NASA Contractor Report 185670

NASA-CR-185670-VOL-2
19920012057

National Aeronautics and Space Administration (NASA)/American Society for Engineering Education (ASEE) Summer Faculty Fellowship Program—1991

Volume 2

William A. Hyman and Stanley H. Goldstein, Editors

Grant NGT 44-001-800

December 1991

NASA Contractor Report 185670

National Aeronautics and Space Administration (NASA)/American Society for Engineering Education (ASEE) Summer Faculty Fellowship Program—1991

Volume 2

William A. Hyman, Editor
Texas A&M University
College Station, Texas

Stanley H. Goldstein, Editor
University Programs Office
Lyndon B. Johnson Space Center
Houston, Texas

Grant NGT 44-001-800

National Aeronautics and Space Administration
Lyndon B. Johnson Space Center
Houston, Texas

December 1991

This Page Intentionally Left Blank

PREFACE

The 1991 Johnson Space Center (JSC) National Aeronautics and Space Administration (NASA)/American Society for Engineering Education (ASEE) Summer Faculty Fellowship Program was conducted by Texas A&M University and JSC. The program at JSC, as well as the programs at other NASA Centers, was funded by the Office of University Affairs, NASA Headquarters, Washington, D.C. The objectives of the program, which began nationally in 1964 and at JSC in 1965, are

1. To further the professional knowledge of qualified engineering and science faculty members

2. To stimulate an exchange of ideas between participants and NASA

3. To enrich and refresh the research and teaching activities of participant's institutions

4. To contribute to the research objectives of the NASA Centers

Each faculty fellow spent at least 10 weeks at JSC engaged in a research project in collaboration with a NASA/JSC colleague. This document is a compilation of the final reports on the research projects done by the faculty fellows during the summer of 1991. Volume 1 contains reports 1 through 14, and Volume 2 contains reports 15 through 27.

This Page Intentionally Left Blank

CONTENTS

Volume 1

Volume 2

FUZZY LOGIC PATH PLANNING SYSTEM FOR COLLISION AVOIDANCE BY AN AUTONOMOUS ROVER VEHICLE

Final Report

NASA/ASEE Summer Faculty Fellowship Program--1991

Johnson Space Center

Prepared By:	Michael G. Murphy, Ph.D.
Academic Rank:	Professor
University & Department:	University of Houston-Downtown Department of Applied Mathematical Sciences Houston, TX 77002
NASA/JSC	
Directorate:	Information Systems
Division:	Information Technology
Branch:	Software Technology
JSC Colleague:	Robert N. Lea, Ph.D.
Date Submitted:	August 23, 1991
Contract Number:	NGT-44-001-800

ABSTRACT

The Space Exploration Initiative (SEI) of the United States will make great demands upon NASA and its limited resources. One aspect of great importance will be providing for autonomous (unmanned) operation of vehicles and/or subsystems in space flight and in exploration of environments such as the surface of Mars. An additional, and complicating, factor of SEI is that much of the need for autonomy of operation will take place under conditions of great uncertainty or ambiguity. Thus, traditional approaches are less likely to provide satisfactory results for the ambitious goals of SEI. In particular, it is appropriate to consider how control situations (one of the major problem areas) can be handled through emerging technologies such as fuzzy logic, neural networks, and genetic algorithms. The absence of precise mathematical modelling for uncertain environments provides an opening for alternative approaches that are better suited for such problem domains and which in fact may lead to a lower level of computational complexity or even the possibility of customized computer chips that will handle specific control problems.

Systems already developed at NASA/JSC have shown the benefits of applying fuzzy logic control theory to space-related operations. This report is concerned with four major issues associated with developing an autonomous collision avoidance subsystem within a path planning system designed for application in a remote, hostile environment that does not lend itself well to remote manipulation of the vehicle involved through Earth-based telecommunications. A good focus for this is unmanned exploration of the surface of Mars. The uncertainties involved indicate that robust approaches such as fuzzy logic control are particularly appropriate.

Four major issues addressed in this report are:

1. avoidance of a single fuzzy moving obstacle;
2. backoff from a deadend in a static obstacle environment;
3. fusion of sensor data to detect obstacles;
4. options for adaptive learning in a path planning system.

It is likely that the approaches described and references given will be useful for other problems with differing situations but characteristics common to those described here (e.g., autonomy of operation under conditions of uncertainty).

INTRODUCTION

This report addresses four important aspects of autonomous collision avoidance in a path planning system: avoidance of a single fuzzy moving obstacle; backoff from a deadend in a static obstacle environment; the fusion of sensor data from multiple sensor sources for obstacle detection; and, options for adaptive learning in a path planning system. Previous work dealt with various types of stationary obstacle scenarios.

NASA is currently involved with planning a variety of unmanned missions. As a particular focus, this investigation will consider some of the issues associated with unmanned surface exploration of Mars.

Examples of the need for collision avoidance by an autonomous rover vehicle with a moving obstacle would be: wind-blown debris, surface flow or anomalies due to subsurface disturbances, another vehicle, etc. The other issues of backoff, sensor fusion, and adaptive learning are important in the overall path planning system concept. Fuzzy logic control systems have been shown by Robert N. Lea of NASA/Johnson Space Center and others to be an effective tool in building reliable systems that function well in the presence of uncertainty or ambiguity (1,2,3).

The research into the use of fuzzy logic in the decision and control process for autonomous path planning including collision avoidance is a new aspect of a continuing problem domain (4,5,6,7,8,9). The theory of fuzzy sets and fuzzy logic was introduced in 1965 by L. A. Zadeh of the University of California, Berkeley (10). The book by Klir and Folger (11) gives a good treatment of the fundamentals of this field, while the book by Kosko (12) addresses more advanced aspects as well as the interface between the application of fuzzy and neural approaches to problem-solving. Until the last few years, there has been a dearth of commercial applications of fuzzy logic control (13). At the present, there is a tidal wave of applications coming from Japan, addressing problems in subway systems, process control in industry, automatic transmissions, camera display integrity, washing machines, vacuum cleaners, etc. Togai InfraLogic, Inc., of California has marketed a fuzzy logic expert system shell for ease of fuzzy logic applications development (14).

For true autonomy of operation, higher-level path planning is necessary to ensure integrity of the physical system, allow for conservative modification of guidance rules based on experience, and facilitate efficient backoff from deadend approaches that interfere with accomplishing the original goal of the mission. A consideration in this investigation is to seek generalized features that encourage extension and adaptation of this path planning system to other environments (e.g., autonomous collision avoidance for space vehicles with respect to other space vehicles, natural and man-made space debris, etc.) Other types of uncertainty modelling, such as Dempster-Shafer theory, may well be useful tools to complement the strengths of fuzzy logic.

AVOIDANCE OF MOVING OBSTACLES

For purposes of this report, we will address a single, moving fuzzy obstacle; that is, an obstacle with a fuzzy radius w and either a fuzzy speed [m - Δm , m + Δm] or a fuzzy direction [ø - Δø , ø + Δø]. See Figure 1 for a graphic representation of these situations.

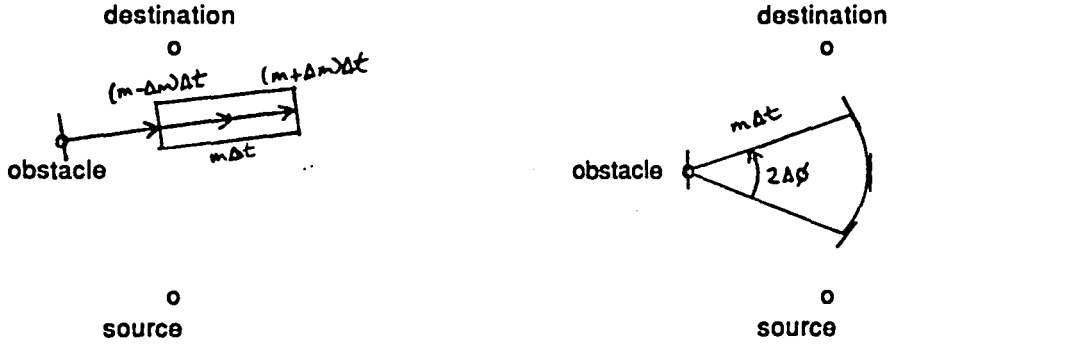

a. fixed direction, fuzzy speed

b. fixed speed, fuzzy direction

Figure 1. - Moving Obstacle Scenario

Using the simplest possible approach to a potentially complicated problem, it is best to not try to project the exact path of the moving obstacle. Instead, the best approach is to use fuzzy rules and a fuzzy inferencing mechanism to take an imprecise environment and assess the likelihood of collision based on the current situation. If necessary, collision avoidance techniques are then applied to avoid the danger. Figure 2 contains two key rules for

the system and membership functions for key fuzzy linguistic variables. To activate the avoidance system means to make changes as needed in speed and direction to avoid collision.

Sample Fuzzy Rules: (fuzzy linguistic variables are underlined)

If the paths of the vehicle and the obstacle cross
and if the time of crossing is similar,
then the obstacle is a hazard.

If the obstacle is close and if the obstacle is a hazard,
then activate the collision avoidance system.

Sample Membership Functions for Fuzzy Linguistic Variables:

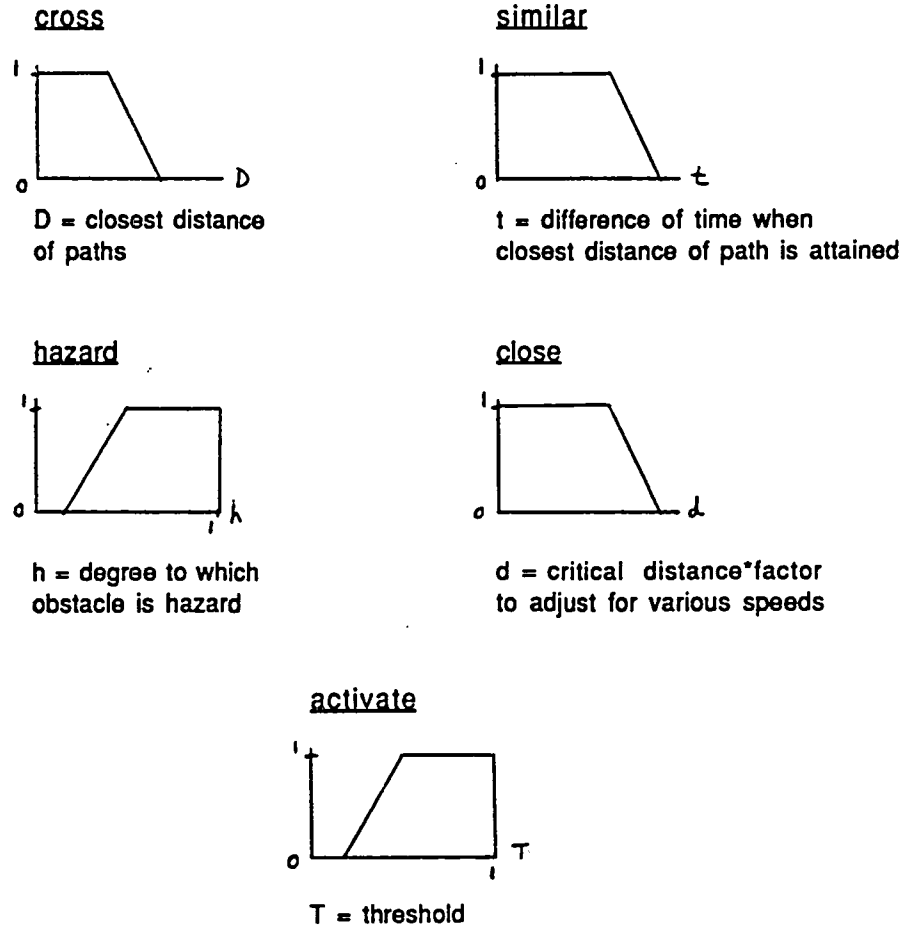

Figure 2. - Sample Rules and Membership Functions

Figure 3 has the architecture for a fuzzy avoidance system for a moving fuzzy obstacle. Implementation may well result in modification of this architecture and/or subsystems to enhance performance. In general, this will be a subsystem of a general path planning system for autonomous exploration with collision avoidance.

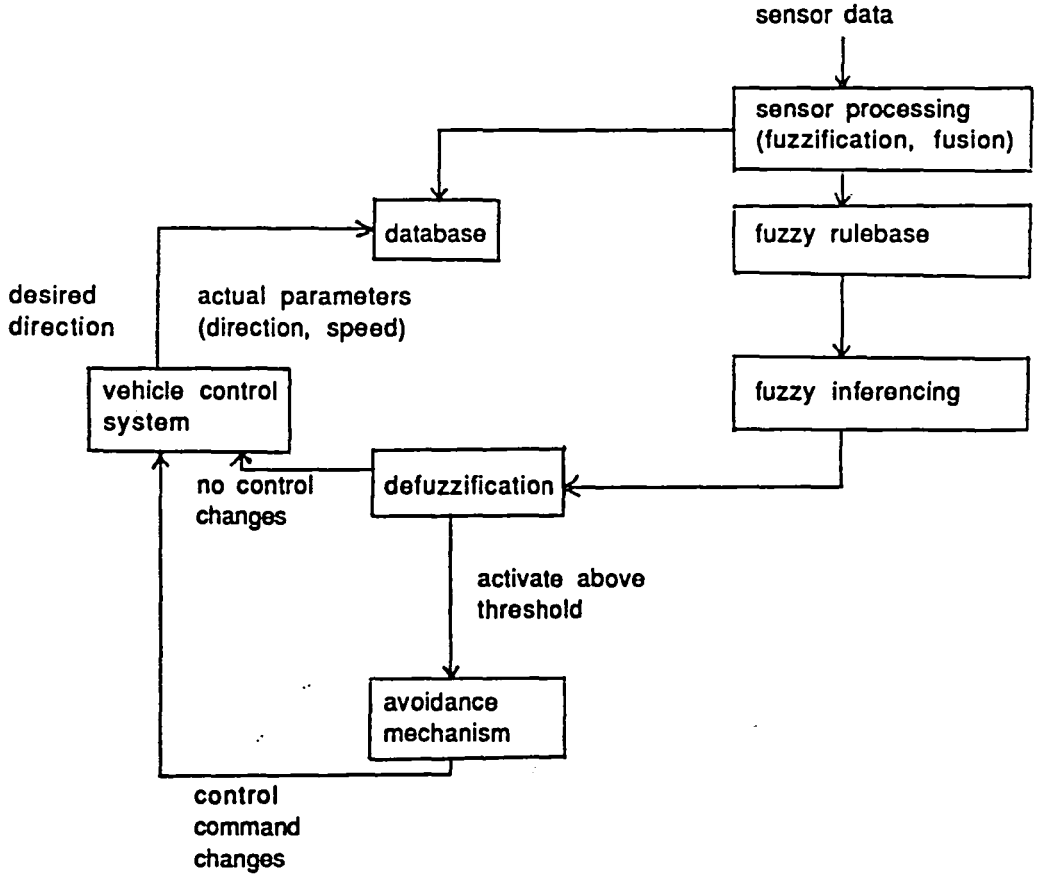

Figure 3. - Architecture for Fuzzy Collision Avoidance Sysem

SENSOR FUSION

Sensor fusion, in the sense of combining information based on more than one sensor operating simultaneously, promises to give a significant improvement in object detection over the use of a single sensor source (4,8). The problem, of course, is to have a computationally reasonable means of combining and interpreting sensor data from dissimilar sources. Dempster-Shafer Theory is a

good candidate for giving useful combinations and interpretations of such data, but it is computationally intense (15,16). A formation of information in a hierarchical structure can be used to give a significant improvement in computational complexity. Our search here has been exploratory in nature, and we see directions for further work, but it is clear that nothing definitive has been established to date.

BACKOFF TECHNIQUES

Basically there are two viable techniques for backoff from deadends in a static environment that is not fully mapped and where uncertainty of information is a regular element of the environment. The first technique is based on reversing direction coupled with extending the critical distance for sensor processing and synthesis so that oscillatory travel patterns are avoided. A possible concern with this approach is that the algorithm is essentially a greedy heuristic that works under the premise that most of the time making a local optimal choice will yield a successful path. The second approach is to store a modified world model that would map known (or approximate) information regarding the explored environment so that a repeat of that exploration would be prevented. The problem with this second approach is the need for significant memory to store the model and increased processing capability for subsequent path development in backoff situations. With neither choice being a clear winner, it is likely that the first approach may have an advantage in the sense of a lesser degree of complexity. Other possibilities are: storing a limited map of the explored region or blocking one or more sectors from being chosen for the direction of the vehicle until an obstacle threshold has been passed and new data is available to evaluate path options. These are desired directions and alternatives for expanding and improving the algorithms previously reported (5,6,7).

OPTIONS FOR ADAPTIVE LEARNING IN A PATH PLANNING SYSTEM

One of the most promising options for adaptive learning in control environments has been the use of neural networks (5,12,17,18,19,20,21,22,23). A difficulty with applying neural networks to adaptive learning in fuzzy environments is the transfer

of techniques from one application to another. Many of the neural approaches to control are very domain specific and require extensive modification (when possible) to use in conjunction with fuzzy systems. One particular approach which is promising is to use neural nets (or even neurons) to tune (adjust) the membership functions of fuzzy variables. Attempts to find general approaches or modify existing designs to accomplish this have been less than successful to date, but it is too early to write off this approach. A bigger problem will be to develop an adaptive system that will operate on data being generated as the system performs and continually (or periodically) update parameters of the system to improve or maintain optimal (or near optimal) performance. Even though this appears to be feasible, it is still unsolved and appears to be more difficult than originally viewed and will still face the test of convincing skeptical engineers that a new technology that adapts to changing circumstances in uncertain environments is a viable choice for mission critical problem-solving. A different adaptive technology that seems possibly suited for training a fuzzy logic control system is genetic algorithms (24).

CONCLUSION AND FUTURE DIRECTIONS

Fuzzy logic control provides significant opportunity for application to uncertain and/or ambiguous control environments such as autonomous collision avoidance. Many areas have been identified in this report that warrant further investigation. In brief, areas of promise are simulation of avoidance of a moving obstacle, use of various approaches to sensor fusion, validation of backoff techniques for static collision avoidance environments, and further development of adaptation techniques to improve/maintain system performance under conditions of uncertainty. Integrating these concepts into a viable path planning system is a worthy, if difficult, goal. Finally, identification of general concepts that transfer to other problem domains is a side goal that may be even richer than the application to collision avoidance and path planning.

REFERENCES

1. Lea, Robert N.: Automated Space Vehicle Control for Rendezvous Proximity Operations. *Telematics and Informatics*, vol. 5, no. 3, 1988, pp. 179-185.

2. Lea, Robert N.: Applications of Fuzzy Sets to Data Monitoring and Process Control. *Proceedings of the ISA'88 International Conference and Exhibit*, October, 1988, pp. 1495-1502.

3. Lea, Robert N.; Togai, Masaki; Teichrow, Jon; and Jani, Yashvant: Fuzzy Logic Approach to Combined Translational and Rotational Control of a Spacecraft in Proximity of the Space Station. *Proceedings of the Third International Fuzzy Systems Association Congress*, August, 1989.

4. Dougherty, E.; Giardina, C.: Mathematical Methods for Artificial Intelligence and Autonomous Systems. Prentice Hall, 1988.

5. Murphy, Michael: Fuzzy Logic Control System to Provide Autonomous Collision Avoidance for Mars Rover Vehicle. Final Report of Summer Faculty Fellowship at NASA/JSC, 1990.

6. Lea, R.; Murphy, M.; and Walters, L.: Fuzzy Logic Control for Autonomous Collision Avoidance. *North American Fuzzy Information Processing Society 1991 Workshop Proceedings*, May, 1991, pp. 154-158.

7. Lea, R.; Jani, Y.; Murphy, M.; and Togai, M.: Design and Performance of a Fuzzy Logic Based Vehicle Controller for Autonomous Collision Avoidance. *Fuzzy and Neural Systems, and Vehicle Applications '91*, (to appear; Tokyo, Japan; November, 1991).

8. Yen, John; and Pfluger, Nathan: Designing an Adaptive Path Execution System. *Proceedings of the 1991 IEEE International Conference on Systems, Man and Cybernetics*, (to appear).

9. IEEE Expert, vol. 6, no. 4, August, 1991 (4 papers on vision and navigation).

10. Zadeh, L. A.: Fuzzy sets. *Information and Control*, vol. 8, pp. 338-353.

11. Klir, George J.; and Folger, Tina A.: Fuzzy Sets, Uncertainty, and Information. Prentice-Hall, 1988.

12. Kosko, Bart: Neural Networks and Fuzzy Systems: A Dynamical Systems Approach to Machine Intelligence. Prentice Hall, 1992 [sic].

13. Lee, Chuen-Chien: Fuzzy Logic in Control Systems: Fuzzy Logic Controller-Parts I and II. *IEEE Transactions on Systems, Man, and Cybernetics*, vol. 20, no. 2, 1990, pp. 404-435.

14. TILShell User's Manual, Release 1.1. Togai InfraLogic Inc., Jan., 1990.

15. DeKorvin, A.; Kleyle, R.; and Murphy, M.: Properties of States of Recognition Arising from a Set of Knowledge Systems with Imperfect Reporting. *Stochastic Analysis and Applications*, vol. 9, no. 2, 1991, pp. 133-146.

16. DeKorvin, A.; Kleyle, R.; and Murphy, M.: Methods for Efficient Object Detection under Conditions of Uncertainty and with Implications for Path Planning. *North American Fuzzy Information Processing Society 1991 Workshop Proceedings*, May, 1991, pp. 42-46.

17. Widrow, Bernard; and Stearns, Samuel D.: Adaptive Signal Processing. Prentice Hall, 1985.

AN INVESTIGATIVE REDESIGN OF THE ECG AND EMG SIGNAL CONDITIONING CIRCUITS FOR TWO-FAULT TOLERANCE AND CIRCUIT IMPROVEMENT

Final Report

NASA/ASEE Summer Faculty Fellowship Program--1991

Johnson Space Center

Prepared By:	Edward M. O'Brien, Ph.D.
Academic Rank:	Associate Professor
University & Department	Mercer University Biomedical Engineering & Electrical and Computer Engineering Departments Macon, Georgia 31207
NASA/JSC	
Directorate:	Space and Life Sciences
Division:	Life Sciences Project
Branch:	Project Engineering
JSC Colleague:	Donald J. Stilwell
Date Submitted:	October 14, 1991
Contract Number:	NGT-44-001-800

INTRODUCTION

An investigation was undertaken to make the electrocardiography (ECG) and the electromyography (EMG) signal conditioning circuits two-fault tolerant and to update the circuitry. The present signal conditioning circuits provide at least one level of subject protection against electrical shock hazard but at a level of 100 μA (for voltages of up to 200 V). However, it is necessary to provide catastrophic fault tolerance protection for the astronauts and to provide protection at a current level of less than 100 μA. For this study, protection at the 10 μA level was sought. This is the generally accepted value below which no possibility of microshock exits. Only the possibility of macroshock exists in the case of the signal conditioners. However, this extra amount of protection is desirable. The initial part of this report deals with current limiter circuits followed by an investigation into the signal conditioner specifications and circuit design.

CURRENT LIMITERS

JFET Limiters

There are several ways to limit the amount of current that flows into a subject that is connected to an instrument via electrodes. The choice of method depends on the origin of the current. The current may come from the instrument's own power supplies or from an external source returning to that source's ground via the instrument.

One protection technique is to insure that there is no connection between the instrument and the external source's ground. This can be done using isolation techniques such as infrared or transformer coupling. This technique was rejected in the case of the signal conditioners for two reasons. First, the isolation devices consume large amounts of power (supply currents in the 4 to 10 mA range) and second, they will not protect against the dc current that could flow into the subject from the power supply on the subject side of the isolation system.

Another type of current limiter is the input to the instrumentation amplifier that will be used in the signal conditioners. Under normal circumstances very little current flows into this terminal. The current that does flow is the bias current for the operational amplifiers (op amps) of the instrumentation amplifier. These currents can be as low as 6 nA for some BJT op amps or as low as the 30 pA for FET op amps. However, these are the currents that flow when the op amps are in their nonsaturated mode of operation. Little is known about how much current would flow if the op amp should saturate or if excessive input voltage should cause a break down of the op amp input stages. For these reasons it is not reasonable to count the input stages of the instrumentation amplifier as a current limiter.

Current limiters can be made from semiconductors. Most circuits use JFET circuits since they are depletion devices and lend themselves to passive operation. However, current limiters can be also made from diodes. The various types of circuit designs have their own advantages and disadvantages. Several designs will be

presented and discussed.

Figure 1 shows the current limiter that is used in the present signal conditioning circuits. It is composed of two n-channel JFETs and three resistors. For low current flowing through the device from the left to the right, Q1 and Q2 initially have low resistance which is much lower than R1. As the current increases, the voltage across R1 increases to the pinch off, V_p, value of Q1. Then Q1 limits the current through the device to a value of approximately $V_p/R1$. Q2 remains as a low resistance. The role of Q1 and Q2 reverse as the current through the device reverses. R2 and R3 are necessary if V_p is larger than .7 V (the turn-on voltage of the diode formed by the gate and channel). Regardless of the value of V_p, including these resistors is a good idea and their value should be fairly large. Figure 2 shows the current through the device as predicted by SPICE. For this run the FETs had a pinch-off of .5 V and an I_{DSS} of 4 mA. (As long as I_{DSS} is of a normal value, i.e., the mA level, this parameter has no effect on the maximum current limit value for this and the other circuits to be discussed.) The resistor R1 was 50 kΩ and R2 and R3 were 1 MΩ. The advantages of this circuit are that there are few parts and only n-channel FETs are required. The dynamic "on" resistance of this circuit is approximately R1 which is 50 kΩ in the above example. The disadvantage of this circuit and all JFET circuits is that the pinch-off voltage must be small to keep the size of the resistor R1 small for a given maximum current flow. Also the breakdown voltage for each device must be larger than the maximum voltage that the subject could ever encounter. JFETs that have low pinch-off voltage and high breakdown voltage are difficult to obtain.

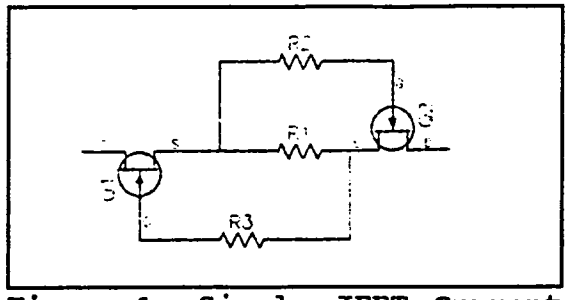

Figure 1. Simple JFET Current Limiter.

Another type of current limiter circuit is shown in Figure 3. This device has four JFETs, two n-channel and two p-channel. The bidirectional current through this

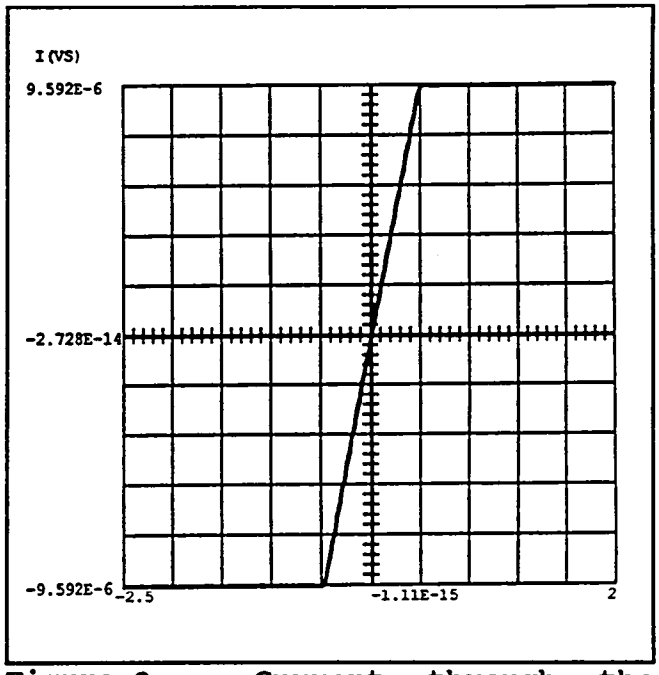

Figure 2. Current through the Limiter of Figure 1.

device is shown in Figure 4 which was generated with SPICE. The pinch-off voltages for these FETs were .5 V. To obtain a maximum current flow of approximately 10 μA, R1 and R4 were 50 kΩ. The other resistors were large at 1 MΩ. The "on" resistance of this device is R1 plus R4. The maximum current flow is $V_p/(R1+R2)$. An advantage of this circuit is that after the voltage across the device gets to $2V_p$ the current flow is reduced to approximately zero. An other advantage is that for given device breakdown voltage the voltage is divided between one of the n-channel and p-channel FETs. Thus, if the overall device breakdown voltage needs to be 200 V, each FET only needs to withstand 100 V. One of the disadvantages of this circuit is the large "on" resistance. It is twice that of the circuit of Figure 1 for the same pinch-off voltages and maximum current.

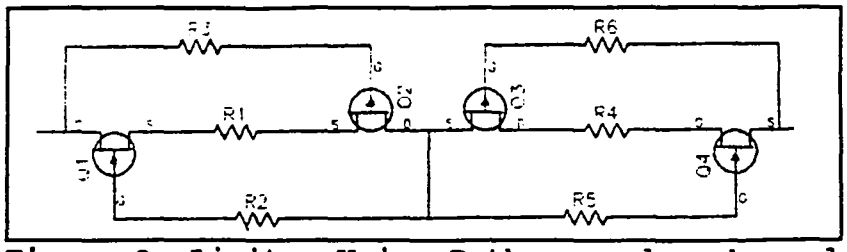

Figure 3. Limiter Using Both n- and p-channel FETs

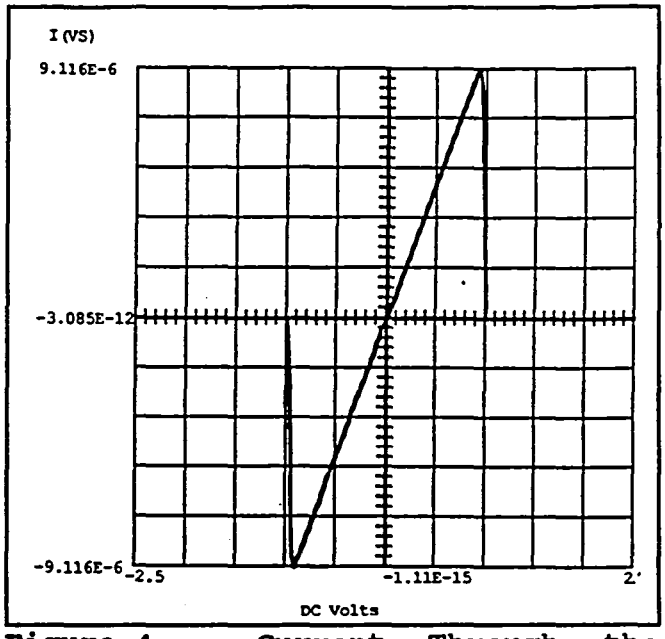

Figure 4. Current Through the Limiter of Figure 3.

The final JFET circuit to be presented is a slightly modified version of the patented circuit used in the Cherne Medical current limiter (Kroll, 1988). The circuit is shown in Figure 5. It is composed of 6 JFETs (4 n-channel and 2 p-channel) and several resistors. This circuit is similar in response to the circuit of Figure 3. That is the current reaches a peak value of approximately $V_p/R2$ as the voltage across the device increase to V_p and declines to a minimum when the voltage reaches $2V_p$. The value of this minimum (left-to-right) current is $(V_p-.5\ V)/R3) + (V_p-.5\ V)/R5$. The .5 V is that voltage at which the diodes formed by Q3 and Q6 just start to turn on. The "on" resistance of the device is approximately R2. Figure 6 shows the SPICE predicted current for the device with all FETs having $V_p = .5$ V, R2 = 50 KΩ, and the other resistors equal to . 1 MΩ. If all resistors but R2 are increased to 1 MΩ the current when the device is hard limiting is approximately .2 μA. The only advantage of this circuit over the circuit of Figure 4 is that, for the same current limit and V_p of the FETs, the "on" resistance is half as much. As with

the circuit of Figure 4, considering only left to right current flow, the breakdown voltages of Q1 and Q4 need only be one half that required for the complete limiter. The disadvantage of this circuit is its large parts count and the fact that it requires both n-channel and p-channel FETs.

The above circuits where fabricated, except with devices with V_p's greater than .5 V, and their general characteristics verified. In all cases, when the devices were on and not limiting, they behaved like pure resistors.

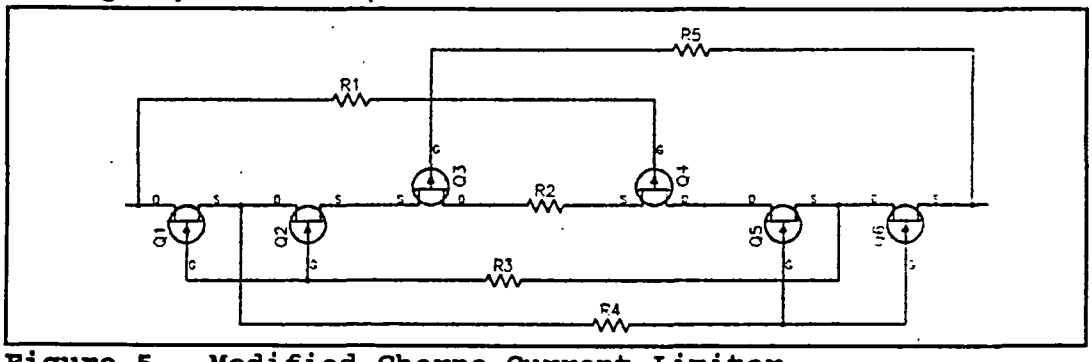

Figure 5. Modified Cherne Current Limiter.

It should be pointed out that actual testing of the Cherne Medical current limiter shows it to follow the SPICE predicted current vs voltage curve except in the hard limit region. In this region the predicted current is .56 μA while the actual testing plus the published advertized value is about 5 μA. The reason for this discrepancy is not clear.

Diode Limiters

As mentioned earlier, current limiters can be made from diodes. The ideal diode equation is given as follows

$$i_d = I_s(e^{v_d/nV_T} - 1) . \qquad (1)$$

Where I_s is the reverse saturation current, n is a constant that is approximately 1 for germanium diodes and 2 for silicon diodes, and V_T is a constant equal to about 25 mV at room temperature. When the diode is reverse biased, the current is constant at a value of I_s. If the reverse saturation current had a value of 10μA and two of these diodes were placed back-to-back as shown in Figure 7, then an ideal current limiting device would be obtained. The "on" conductance of the one diode can be found by differentiating equation (1) above with respect to v_d. The result when inverted gives the "on" resistance of one diode as

$$R_{on} = nV_T / I_s . \qquad (2)$$

For n = 2 and I_s = to 10μA the "on" resistance for a single diode would be 5 kΩ and 10 kΩ for the pair. The breakdown voltage of each would have to be in excess of that

required for the current limiter (200 V for this design).

Unfortunately, the diode current in the reverse direction is not constant. It continues to increase slowly until the breakdown region, with its characteristic knee region, is reached. Designing a current limiter using diodes made from silicon is not practical since the devices have I_s values in the nA range. This makes the "on" resistance unacceptably large from the stand point of thermal noise voltage plus if BJT op amps are used it is difficult to get the required bias currents through the limiter. Germanium diodes have reverse saturation currents about a thousand or more times larger than silicon diodes and they typically have low breakdown voltages.

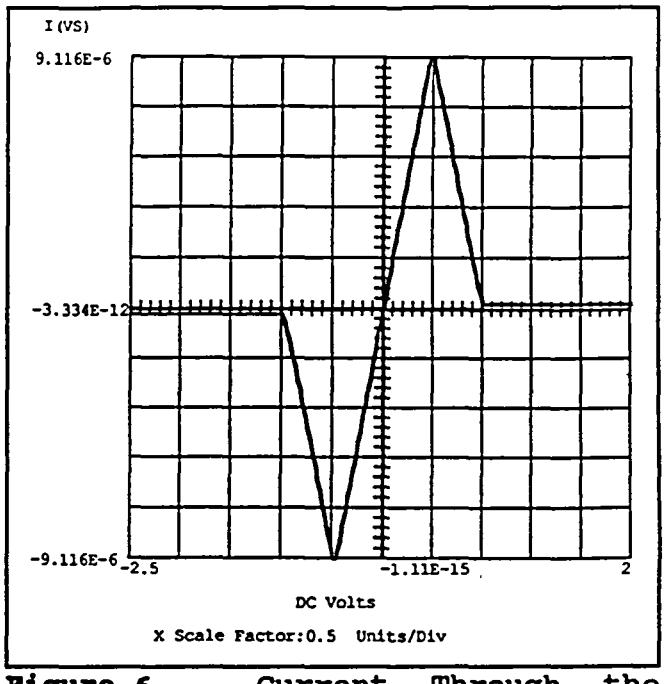

Figure 6. Current Through the Limiter of Figure 5.

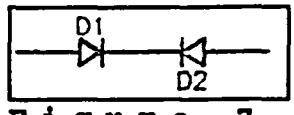

Figure 7. Diode Current Limiter.

A diode that can be used as a current limiter is the 1N277J. This device is supplied by BKC International[1]. This is a germanium diode that has a breakdown voltage of about 125 V. Because of this relatively low breakdown voltage two of the diodes were placed in series and the voltage vs current curve in the reverse biased region generated. This graph is shown in Figure 8. As can be seen from this figure the current through the series pair is less than 10 μA for voltages below -255 V. This is the corner of the knee region because at a voltage of -280 V the current increases to almost 100μA. Curves for several pairs of diodes where generated with approximately the same results. As can be seen from the steepness of the curve near the origin, the "on" resistance of the series pair is very high. The measured value is about 105 kΩ. For two pair of diodes placed back-to-back to obtain current limiting in both directions, the "on" resistance is about 210 kΩ. To reduce this resistance three of these limiters could be placed in parallel. The "on" resistance will drop to about 70 kΩ and the total current through the device at 200 V would only be about 20 μA. Twelve diodes would thus be needed for the construction of one limiter device. These diodes are not available in die form. Therefore, with the standard DO7 package, a large amount of

[1]BKC International Electronics, Inc., 6 Lake Street, Lawrence, MA 01841, (508) 681-0392

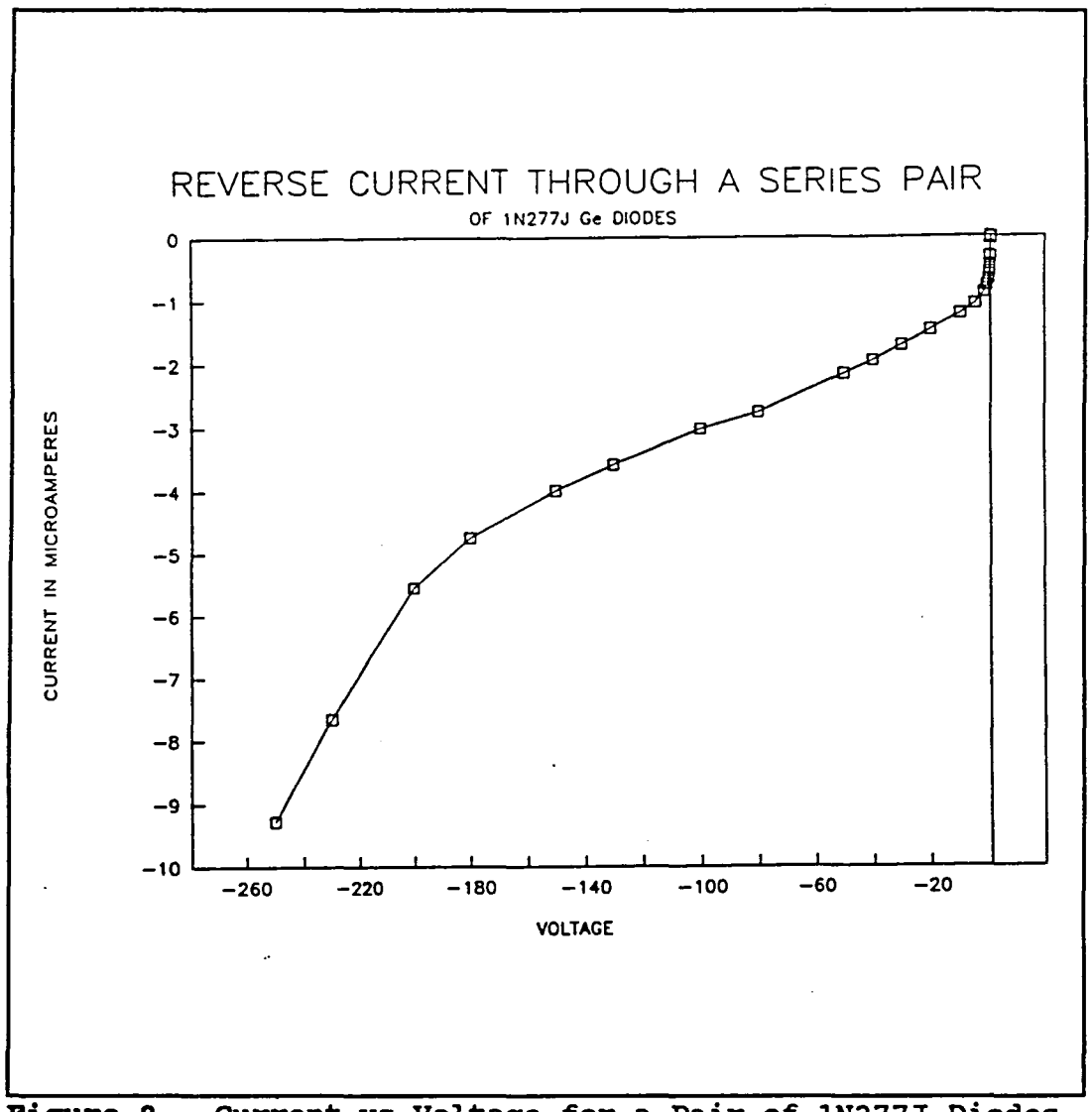

Figure 8. Current vs Voltage for a Pair of 1N277J Diodes

volume will be occupied by one limiter.

The recommendation for the choice of current limiter is the circuit shown in Figure 1. Only n-channel JFETs are needed and these are easier to obtain that p-channel JFETs with low pinch-off voltage and high breakdown voltage.

ACHIEVING TWO-FAULT TOLERANCE

Again, because little is known about how op amp input circuits fail it is not recommended that they be considered as one level of fault tolerance. What is recommended is to series three current limiters in each of the patient leads. Thus it

would take three times the breakdown voltage of an individual limiter to cause the three to breakdown. Since these are in series the current protection would be that of the individual limiters. A disadvantage of placing three limiters in series is that the total resistance is three times that of an individual limiter. Thus thermal noise voltage will have to increase to obtain two-fault tolerance.

SIGNAL CONDITIONER SPECIFICATIONS

The amplitude and frequency content of the ECG and EMG will determine some of the signal conditioner specifications. The amplitude of the ECG is .1-4 mV (Olson, 1978) and the recommended 3 dB bandwidth is .05 to 100 Hz (Kossman, 1967). Pipberger et al. (1975) also recommend that the response of any EMG amplifier be flat within +/- .5 dB in the range of 0.14 to 25 Hz. The amplitude of the EMG is .1-1 mV for surface electrodes. If needle electrodes are used for the EMG much larger voltages, up to 90 mV, can be recorded. The bandwidth required for the EMG is 25 to several kHz (Neuman, 1978). A maximum bandwidth of 1000 Hz is recommended since most clinical studies rarely use bandwidths in excess of 500 Hz. The amplitude out of the signal conditioners should be 5 V or less and should be designed with flexible gain. The gain is recommended to be from 400 to 8000. This would amplify a .1 mV signal to a level of .8 V and a signal of 12.5 mV will not exceed 5 V.

The input impedance of any ECG or EMG amplifier should be as large as possible. This will reduce any voltage divider effect caused by the sum of the total source impedance (skin impedance, electrode impedance, and current limiter impedance) and the input impedance of the amplifier. High input impedance will also reduce any effective input voltage caused by a common mode voltage and source impedance imbalance. The recommended input impedance is at least 5 MΩ by Pipberger et al. (1975). Hauta and Webster (1973) also recommend a 5 MΩ input impedance to keep a source impedance imbalance of 5 kΩ and a common mode voltage of 10 mV from causing more than 10 μV if equivalent input voltage. A value of 10 μV corresponds to 1% of a typical 1 mV input ECG signal.

The common mode rejection ratio, CMRR, of the amplifier should also be as large as possible to reduce the output voltage caused by any signal common to the inputs. Hauta and Webster (1973) recommend a modest 60 dB CMRR at 60 Hz with a 5000 Ω source impedance imbalance.

Random noise is always present in resistors and amplifier electronics. This random noise can be expressed in rms or peak-to-peak voltages. The peak-to-peak voltage is typically a factor of 6 to 8 times the rms voltage (Horowitz and Hill, 1989, p. 454). The peak noise when referred to the input should be no more that about 1% of the input signal level. This would correspond to about 2 μV of peak-to-peak node voltage (.25-.33 μVrms) for the lowest expected 0.1 mV input signals.

Other specifications of the signal conditioning circuits are as follows. They should be battery powered for portability. Since they are battery powered, they should consume as little power as possible. The output resistance should be as small as possible. Since there exists the possibility of more than one signal conditioner connected to an astronaut, it is recommended that the reference electrode be connected to power supply ground

(through the current limiters) as opposed to using some type of "driven right leg" system. With multiple driven systems connected at a time the possibility exists for them to "buck" one another and have an oscillatory reference voltage on the body. The output voltage level should be +/- 5 V and there should also be an output that has a 2.5 V output level for zero input signal.

SIGNAL CONDITIONER DESIGN

The choice of an op amp to be used for the input stages of the instrumentation portion of the signal conditioners was based on the power consumption of the op amp and its noise parameters. Noise is generated at the input of the amplifier due to noise from the input resistors and from the input amplifier. The noise associated with the input resistors is due to thermal noise, shot noise and flicker (1/f) noise. According to Horowitz and Hill (1989, pp. 430-432) for metal film or wire-wound resistors the main component is due mostly to the thermal noise, which is a "white" noise. The total noise voltage in rms is

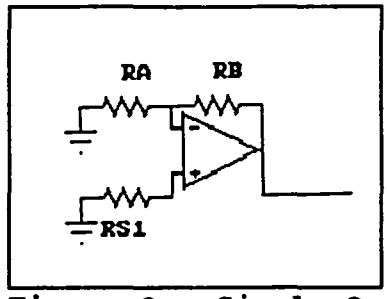

Figure 9. Single Op Amp.

$$E_{thermal}=4kTR(f_H-f_L)^{\frac{1}{2}}. \qquad (3)$$

The constant 4kT has a value of 1.6E-20 at room temperature.
R is the resistance value, and the frequency bandwidth of interest is given by f_H-f_L, the upper and lower frequencies of the band.

The noise associated with the input stages of the op amp can be represented by noise current sources and a noise voltage source. The noise and current sources have noise density power spectra that are composed of flicker noise at low frequencies up to some corner frequency (which is generally different for the noise current and noise voltage sources) and a constant ("white") noise power spectrum from this corner frequency out to infinity. In Figure 9 is shown an op amp with both inputs grounded. R_{S1} is the source resistance seen by the positive terminal of the op amp and R_{S2} is the parallel combination of resistors R_A and R_B. The total noise in a given bandwidth associated with this stage is given by

$$\begin{aligned} E^2(f_H-f_L) &= e_n^2\times[f_{nv_c}\cdot\ln(\frac{f_{nv_c}}{f_L})+(f_H-f_{nv_c})] \\ &+i_n^2\times[f_{ni_c}\cdot\ln(\frac{f_{ni_c}}{f_L})+(f_H-f_{ni_c})]\times(R_{s_1}^2+R_{s_2}^2) \\ &+4KT(f_H-f_L)(R_{s_1}+R_{s_2}). \end{aligned} \qquad (4)$$

The white noise voltage, in V/√Hz, is given by e_n and the white noise current, in A/√Hz,

is given by i_n. The corner frequencies of the current and voltage are f_{nic} and f_{nvc} respectively. Equation 4 is for the case when f_{nic} and f_{nvc} are between f_L and f_H. If the corner frequencies are less than f_L then their respective bracketed term will change to

$$[f_H - f_L] . \qquad (5)$$

If the corner frequencies are greater than f_H, then their respective bracketed terms will be given by

$$[f_{n_c} \ln(f_H/f_L)] . \qquad (6)$$

The first term in the Equation 4 is due to the amplifier equivalent noise voltage source. The second term is the voltage due to the amplifier equivalent noise current sources flowing through R_{S1} and R_{S2}. The log term in each of these expressions is due to flicker noise. The last term in the expression is the thermal noise of R_{S1} and R_{S2}. Because of the random nature of these noises, the noise powers (and not noise voltages) add. The development of
Equation 4 can be found in Meiksin and Thackray (1984, p. 131). The errors in the formula as presented by Meiksin and Thackray have been corrected here.

The input stage of the signal conditioners will be the standard three op amp differential amplifier. The first two op amps of such a design are shown in Figure 10. The total noise referred to the input will then be due to each of these. Since the noise powers add, the total noise will be given by

$$E_{total} = \sqrt{E_+^2 + E_-^2} \qquad (7)$$

E_+ and E_- will be the noise voltage associated with the op amp of the .+ and - terminals of the overall instrumentation amplifier. Each of their voltages is given by Equation 4. R_{S2} for each op amp is simply the feedback resistor since all the bias currents for their negative inputs passes through those resistors.

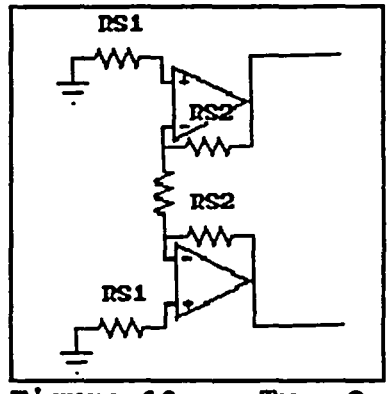

Figure 10. Two Op Amp Input Stage.

Micropower Operational Amplifiers

In this investigation several micropower op amps were examined for their noise characteristics. A list of those op amps considered is given in Table 1 along with the noise parameters of these op amps. Table 2 shows the total noise voltage associated with the two front end op amps for the two different bandwidths of interest, i.e., .05-100 Hz for the ECG signal conditioner and 25-1000 Hz for the EMG signal conditioner. Also shown in this table are several parameters of interest for the op amps: the quiescent power supply current, the bias current, the gain bandwidth product (GBP), and the slew rate. The noise numbers were generated with R_{S1} and R_{S2} equal to

100 and 200 kΩ respectively. R_{S1} was chosen to represent a combination of skin resistance, electrode resistance, and current limiter resistance.

TABLE 1. MICROPOWER OP AMPS AND THEIR NOISE PARAMETERS

op amp	type	En	Fnvc	In	Fnic
		V/√Hz	Hz	A/√Hz	Hz
LT1078	BJT	2.8e-08	7.0e-01	1.7e-14	1.5e+02
LT1178	BJT	4.9e-08	*5.0e-01	1.0e-14	*4.0e+01
LM146	BJT	8.5e-08	1.0e+00	1.8e-13	1.0e+01
LF441	JFET	3.3e-08	2.0e+01	1.0e-14	1.0e+02
OP20-B	BJT	8.0e-08	2.0e+00	9.0e-14	2.0e+01
OP22(1UA)	BJT	9.0e-08	4.0e+00	1.8e-13	2.0e+00
OP22(10UA)	BJT	3.7e-08	6.0e+00	3.7e-13	6.0e+00
OP220	BJT	4.0e-08	3.5e+00	9.0e-14	1.5e+01
OP90	BJT	6.0e-08	8.0e+00	7.0e-13	9.0e+01
TLC27L2	CMOS	7.0e-08	1.0e+01	0.0	1.0e+00
TLC1078	CMOS	7.0e-08	9.0e+00	0.0	1.0e+00

* Personnal communication with an application engineer.

TABLE 2. NOISE VOLTAGE AND OTHER PARAMETERS FOR SELECTED MICROPOWER OP AMPS.

op amp	type	R1 ohm	R2 ohm	Etotal .05-100 Hz 2 OP AMPs uVrms	Etotal 25-1000 Hz 2 OP AMPs uVrms	Quiescent supply current uA	Bias Current nA	GBP kHz	Slew Rate V/usec
LT1078	BJT	1E+05	2E+05	1.07	3.30	39.0	7.0	200.0	0.070
LT1178	BJT	1E+05	2E+05	1.20	3.75	14.0	6.0	60.0	0.025
LM146	BJT	1E+05	2E+05	1.70	5.16	35.0	20.0	100.0	0.040
LF441	JFET	1E+05	2E+05	1.18	3.39	150.0	0.1	1000.0	1.000
OP20-B	BJT	1E+05	2E+05	1.57	4.76	55.0	25.0	100.0	0.050
OP22(1UA)	BJT	1E+05	2E+05	1.77	5.32	160.0	35.0	250.0	0.080
OP22(10UA)	BJT	1E+05	2E+05	1.73	5.04	16.0	7.5	15.0	0.008
OP220	BJT	1E+05	2E+05	1.21	3.64	70.0	20.0	200.0	0.050
OP90	BJT	1E+05	2E+05	5.95	8.16	14.0	20.0	25.0	0.012
TLC27L2	CMOS	1E+05	2E+05	1.54	4.35	14.5	0.6	110.0	0.050
TLC1078	CMOS	1E+05	2E+05	1.52	4.35	14.5	0.6	110.0	0.047

From Table 2 the candidates for the op amps to be used are either the LT1078 or the LT1178 since these have the lowest total noise and the smallest quiescent power supply current. It should be noted that these predicted noise voltages are higher than the recommended values of .25-.33 μV. However, those values were based on an input signal amplitude of only .1 mV. The typical input signal is generally about 1 mV. For this

level of signal, the random noise would be less than 1% of the input signal.

The predicted noise voltages for these two op amps were experimentally verified using fixed resistors. The noise generated using electrodes was actually higher by a factor of four than the predicted values. This is probably due to random fluctuations of the electrode half-cell potential; a factor not accounted for in the noise model.

The choice between the LT1078 and the LT1178 can be made based on the other parameters listed in the table. The slew rate needed for the op amp is determined by the last op amp of the design and is given by

$$slewrate = 2\pi f_{max} V_{out} \qquad (8)$$
$$2\pi(1000Hz)5V = .314V/\mu sec.$$

The maximum frequency required is for the EMG signal conditioner and is 1000 Hz. The maximum output voltage required is 5 V. Given this value of slew rate, only the LT1078 will be satisfactory. This op amp is very attractive for purposes of the signal conditioner because the power supply current is only 39 μA. It is also available in die form.

Figure 11 shows the first stage of the signal conditioner. This stage is the standard three op amp differential amplifier. The overall gain of this stage is 400 (the minimum for the signal conditioners). The gain is split evenly between the first section and second section, i.e., 20 for each. With a GBP of 200 k this will allow each stage to pass frequencies up to 10 kHz. The CMRR of the first stage is 26 dB (common gain of 1 and a difference gain of 20). The worst CMRR of the second section using .1% resistors is 74 dB. The CMRR of the second stage op amp sets the limit for the stage. The CMRR of the LT1078 is 106 dB which is much higher than 74 dB predicted for the second stage. Thus, the limit on CMRR of the second stage will come from the resistors used. The resistors used in the first section should be metal film or wire wound to reduce shot and flicker noise in these resistors.

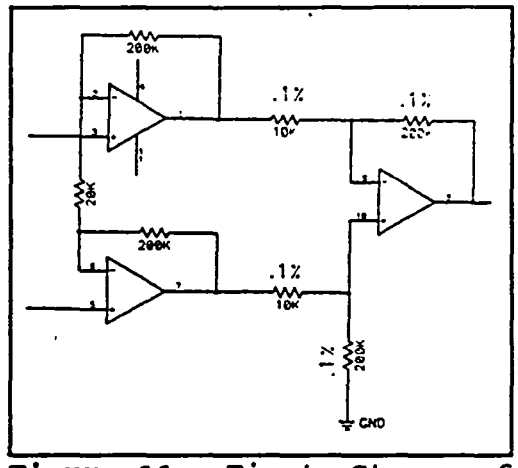

Figure 11. First Stage of the Signal Conditioner.

It is desirable to alter the value of one of the resistor values specified in this design. If the 200 kΩ feedback resistors are changed to 20 kΩ the total random noise, referred to the input, drops from 1.07 μVrms to .74 μVrms.

Figure 12 shows the filtering sections. The output of the first stage will go to a first-order high-pass filter. The 3 dB frequency is given by $1/(2\pi RC)$. For the values shown, the break frequency is approximately .05 Hz. The break frequency can be changed to approximately 25 Hz for the EMG signal conditioner by changing the resistor value to 13.7 kΩ. Also shown in this figure is a fourth-order voltage controlled voltage source, VCVS, Butterworth low-pass filter. This filter provides maximum flatness in the pass-band and very good attenuation in the stop-band. For this filter

$R_{11}=R_{12}=R_{21}=R_{22}=R$ and $C_{11}=C_{12}=C_{21}=C_{22}=C$. The 3 dB frequency is given by $1/(2\pi RC)$. If R = 158 kΩ and C = .01μF, then the 3 dB frequency will be approximately 100 Hz. One percent component values should be used since SPICE analysis showed that for the worst case the magnitude response is only off by 0.5 dB. For two percent values the magnitude response can be off by 1.2 dB in magnitude for the worst case. R14 should be equal to $.152R_{13}$ and R_{24} should be equal to $1.235R_{23}$. For a 3 dB frequency of 1000 Hz. then $R_{11}=R_{12}=R_{21}=R_{22}=$ 15.8 kΩ. The gain of the filter section is 2.575.

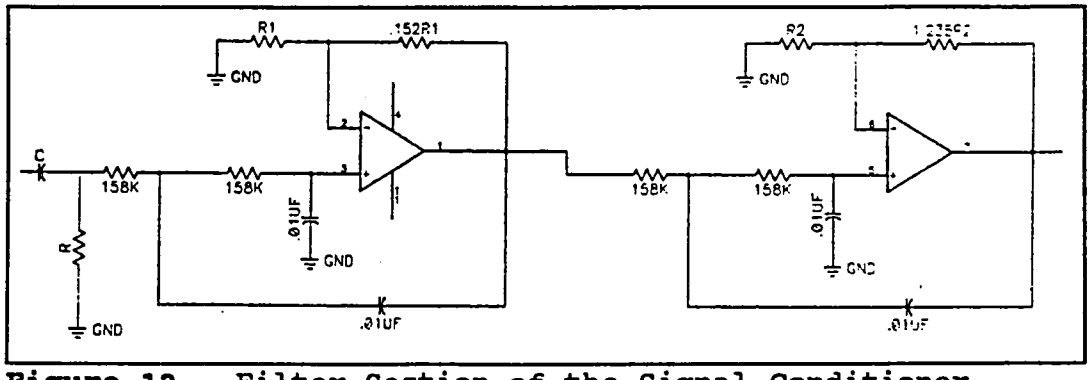

Figure 12. Filter Section of the Signal Conditioner.

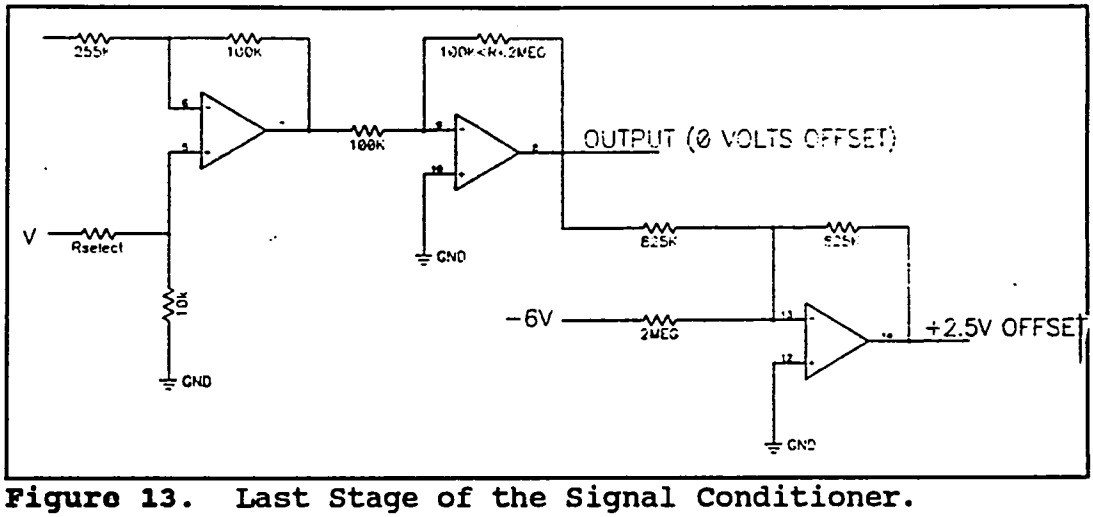

Figure 13. Last Stage of the Signal Conditioner.

The final stage of the signal condition is shown in Figure 13. The signal from the filter section is applied to the 255 kΩ resistor. The gain of this noninverting amplifier is 1/2.55 to negate the gain of the filter section. The V applied to R_{select} is either plus or minus 6 V, the power supplies voltages, and the value of R_{select} is chosen to remove offset voltages of the amplifier. The next stage is a noninverting amplifier that has a gain from 1 to 40, yielding an overall gain of 400 to 8000. The value of the feedback resistor, R, is chosen to yield the desired gain. (Using the LT1078, this op amp could have a gain of 200 and still not limit the bandwidth of the EMG signal.) The output is taken from this

op amp if zero offset voltage is desired. The last op amp simply provides for a +2.5 V offset voltage to the output signal for the ECG signal, if it is desired.

To provide for maximum flexibility only a few resistors need to be changed to make the basic design adaptable to the ECG or EMG signal conditioner. These resistors, R_{11}, R_{12}, R_{21}, R_{22}, R_{select}, and R can be normal resistors that are not in the hybrid circuit by are soldier in a dip header.

The input resistance of the LT1078 is typically 800 MΩ differentially and 6 GΩ common mode. The actual differential input resistance will be higher than 800 MΩ. It will be this value increase by the loop-gain of the first stage. In reality surface effects on the hybrid circuit will cause this resistance to be lower than this very high value. However, it will still be much larger than the recommended value of 5 MΩ.

The output impedance of the LT1078 is 10 Ω for the gain and frequencies of this design. This is well below the recommended value of 200 for the EMG amplifier.

The output voltage of the LT1078 op amps will go down to the minus supply and will go up to 1 V less than the positive supply voltage. Therefore plus and minus 6 V supplies will provide the required 5 V output swing. Batteries made from a series connection of 1.5 V button silver oxide batteries each with 38 mAh life would work well for the supplies. Since there are eight op amps in the design each pulling 39 μA from each supply, the life of the signal conditioners should be 38 mAh/(8*39 μA) = 122 hours.

SUMMARY

Modification of the signal conditioning circuits for the EMG and the ECG was investigated in this study. It is recommended that two-fault tolerance be achieved with the JFET current limiters shown in Figure 1. Three of these devices should be placed in series with each of the electrode leads. It is also recommended that the new signal conditioner amplifiers be based on the LT1078 op amp due to its relatively low noise voltage in comparison to other micropower op amps.

REFERENCES

Hauta, J. C. and J. G. Webster. 1973. 60-Hz Interference in Electrocardiography. IEEE Trans. BioMed. Eng., vol. BME-20(2): 91-101.

Horowitz, P. and W. Hill. 1989. The Art of Electronics. Cambridge University Press, Cambridge. 1125 pp.

Kossmann,N C. E. 1967. Recommendations for the standardization of leads and specification for instruments in electrocardiography and vectorcardiography: Report of committee on electrocardiography, american Heart Association. IEEE Trans. BioMed. Eng., vol. BME-14: 60-68.

Kroll, M. W. 1988. Medical Current Limiting Circuit. U.S. Patent 4,744,369, May 17.

Neuman, M. R. 1978. Biopotential Amplifiers. Page 273-326 in J. G. Webster, ed. Medical Instrumentation, Application and Design. Houghton Mifflin Company, Boston.

Olson, W. H. 1978. Basic Concepts of Instrumentation. Page 1-48 in J. G. Webster, ed. Medical Instrumentation, Application and Design. Houghton Mifflin Company, Boston.

Pipberger, H. V. 1975. Recommendations for standardization of leads and of specifications for instruments in electro-cardiography and vectorcardiography. Circ., 3(2): 11-31.

NEURAL ARCHITECTURES FOR CONTROL

Final Report

NASA/ASEE Summer Faculty Fellowship Program–1991

Johnson Space Center

Prepared by:	James K. Peterson, Ph.D.
Academic Rank:	Assistant Professor
University & Department:	Clemson University Department of Mathematical Sciences Clemson, SC 29631-1907
NASA JSC Directorate:	Information Systems
Division:	Information Technology
Branch:	Software Technology
JSC Colleague:	Robert O. Shelton, Ph.D.
Date Submitted:	July 24, 1991
Contract Number:	NGT -44-001-800

ABSTRACT

In this study, CMAC (Cerebellar Model Articulated Controller) neural architectures are shown to be viable for the purposes of real-time learning and control. Software tools for the exploration of CMAC performance are developed for three hardware platforms, the MacIntosh, the IBM PC and the SUN workstation. All algorithm development was done using the C programming language. These software tools were then used to implement an *adaptive critic* neuro-control design that learns in real-time how to back up a trailer truck. The **truck backer-upper** experiment is a standard performance measure in the neural network literature, but previously the training of the controllers was done off-line. With the CMAC neural architectures, it was possible to train the neuro-controllers on-line in real-time on a MS-DOS PC 386.

CMAC neural architectures are also used in conjunction with a hierarchical planning approach to find collision free paths over two dimensional *analog valued* obstacle fields. The method constructs a *coarse* resolution version of the original problem and then finds the corresponding *coarse* optimal path using multipass dynamic programming. CMAC artificial neural architectures are used to estimate the *analog* transition costs that dynamic programming requires. The CMAC architectures are trained in real-time for each obstacle field presented. The *coarse* optimal path is then used as a baseline for the construction of a *fine* scale optimal path through the original obstacle array.

These results are a very good indication of the potential power of the neural architectures in control design.

In order to reach as wide as audience as possible, we have run a seminar on neuro-control that has met once per week since May 20, 1991. This seminar has thoroughly discussed the CMAC architecture, relevant portions of classical control, back propagation through time and adaptive critic designs. The attendees included staff members from the Information Systems, the Engineering and Life Sciences Directorates and McDonald Douglas Corporation.

1 INTRODUCTION:

In this report, we detail our experiences with the design and application of Cerebellar Model Articulated Controller (CMAC) neural architectures to problems in path planning and control. In order to explore CMAC performance software tools using the C programming language were developed for three hardware platforms, the MacIntosh, the IBM PC and the SUN workstation. These software tools were then used to implement an *adaptive critic* neuro-control design that learns in real-time how to back up a trailer truck. The **truck backer-upper** experiment is a standard performance measure in the neural network literature, but previously the training of the controllers was done off-line. With the CMAC neural architectures, it was possible to train the neuro-controllers on-line in real-time on a MS-DOS PC 386.

CMAC neural architectures are also used in conjunction with a hierarchical planning approach to find collision free paths over two dimensional *analog valued* obstacle fields. The method constructs a *coarse* resolution version of the original problem and then finds the corresponding *coarse* optimal path using multipass dynamic programming. CMAC artificial neural architectures are used to estimate the *analog* transition costs that dynamic programming requires. The CMAC architectures are trained in real-time for each obstacle field presented. The *coarse* path is then used as a baseline in the construction of a *fine* scale path through the original obstacle array.

These results are a very good indication of the potential power of the neural architectures in control design.

In order to reach as wide as audience as possible, we ran a seminar on neuro-control that met once per week from May 20 to July 22, 1991. This seminar thoroughly discussed the CMAC architecture, relevant portions of classical control, back propagation through time and adaptive critic designs. The attendees included staff members from the Information Systems, and Life Sciences Directorates and McDonald Douglas Corporation.

2 CMAC ARCHITECTURES:

The Cerebellar Model Articulated Controller (CMAC) was first developed and described in a series of papers in the 1970's by Albus. [1, 2, 3] Their use in robotic control was further developed by Miller [6, 7, 8] in a series of papers on real time control of robotic arms. Essentially, a CMAC architecture maps the input space of the problem into a much larger **virtual address space** via what can be called **coarse encoding.** The number of entries in the virtual address space is usually quite large, perhaps 10^6 to 10^8 in number; clearly far too large to used for direct storage of tunable parameters. This large virtual address space is drastically reduced in size by *hashing* the virtual address to a smaller working address.

The input-output maps we wish the CMAC architectures to "learn" are of the form $F : [a_1, b_1] \times \ldots \times [a_N, b_N] \rightarrow R^M$. For convenience of expostion, it is easiest to describe

the CMAC architecture for a scalar valued output, ie $M = 1$; a vector-valued CMAC architecture then requires M potentially distinct CMAC structures, one for each ouput component. Let's concentrate then on the map $F : [a_1, b_1] \times \ldots \times [a_N, b_N] \rightarrow R$.

The input space for this CMAC is coarse encoded as follows. The i^{th} component of the input lives in $[a_i, b_i]$. Imagine that we have L levels of overlapping sensors that try to locate a given component in $[a_i, b_i]$. On level j, each sensor for input component i has a *receptive field width* of w_{ij}. If the sensor becomes active at position x, then it remains active until position $\min(x + w_{ij}, b_i)$. When the sensor is active, its output is 1 with value 0 everywhere outside of its region of reception. The starting points of the sensors on a given level and input component can be specified by supplying a fixed *offset*, α_{ij}, which together with the sensor field width completely determines the active region of a particular sensor. We determine the offset schedule by using an *offset base*, β_i.

$$\alpha_{ij} = (j-1)\,\beta_i\,(b_i - a_i), \quad 1 \leq i \leq L, \tag{1}$$

For example, assume there were 10 levels, the number of inputs was 16 with each input component residing in the interval was $[-.1, 1.1]$, the receptive field widths were all .60 and the offsets were all .1. This implies there are 2 sensors on level 0, active on the mutually disjoint subintervals $[0.0, 0.60)$ and $[0.60, 1.1]$; 3 sensors on level 1 active on $[0.0, 0.072)$, $[0.072, 0.672)$ and $[0.672, 1.1]$ and so forth.

Now for a given level j each component p_i of input $\vec{p}$ lies in a unique subinterval component a_j. Hence, the N inputs of $\vec{p}$ can be mapped to a N-tuple of integers $\{a_1, ..., a_N\}$. The **virtual address** of $\vec{p}$ for level j is then

$$\begin{aligned} v_j(\vec{p}) &= \sum_{j=1}^{N} a_j\, T_{j-1}, \\ T_{j-1} &= M_1\, M_2\, \ldots\, M_{j-1}. \end{aligned} \tag{2}$$

where M_j is the number of subintervals the coarse encoding provides on level j and we define $T_0 = 1$.

The virtual address therefore lies between 0 and $M_1 M_2 M_3 \ldots M_N$. This large collection of addresses is called the **virtual memory** of the CMAC architecture and it is reduced to a much smaller sized **working memory** by *hashing* the virtual addresses. We construct the working address associated with input $\vec{p}$ by computing $v_j(\vec{p})$ mod H_j, where H_j is the chosen hash size per level. The input $\vec{p}$ therefore has an associated working address for each level j, $A_j(\vec{p})$, each of which addresses one element of the finite set of weights $\{W^1_{A_1}, W^2_{A_2}, \ldots, W^L_{A_L}\}$. Thus, each input is assigned L weights and the working memory is organized into a two dimensional array of real numbers of L rows, with the j^{th} row of size H_j. The output of the CMAC corresponding to the input $\vec{p}$ is denoted by $g(\vec{p})$ and is defined by

$$g(\vec{p}) = \sum_{j=1}^{L} W^j_{A_j}. \tag{3}$$

The standard CMAC learning rule [3, 6] is then applied to the train the CMAC architectures to learn the I/O mappings. All of the CMAC architectures are initialized with zero values for the weights. Then, if d is the desired output for input $\vec{p}$), as long as the *error*, $d - g(\vec{p})$, is sufficiently large, the weights $W^j_{A_j}$ are updated using as standard delta rule,

$$\left(W^j_{A_j}\right)^{new} = \left(W^j_{A_j}\right)^{old} + \lambda\left(\frac{d - g(\vec{p})}{L}\right). \tag{4}$$

where λ is the *learning rate*, which is generally between 0 and 1. Note that, unlike standard feed forward architectures which use sigmoid transfer functions and therefore have a bounded output typically between 0 and 1, the CMAC output is obtained by *summing* values. Hence, the CMAC output does not necessarily lie between 0 and 1.

3 TRUCK BACKER-UPPER:

In this application, we will study the problem of designing a control architecture that is capable of learning in real-time to back up a standard trailer truck. This problem has become a standard benchmark for the design of self-learning control systems and the success of feed forward architectures in the solution of this problem is well documented in Nguyen and Widrow. [9] We begin with a short discussion of *adaptive control* before concluding with the truck simulation results. Standard references to the *adaptive critic* control which we use in the truck simulation include Barto [4] and Werbos. [14, 15]

3.1 Adaptive Control:

Let's consider a general control problem of the form

$$\min_{\theta \in S} \int_0^\infty f_0(x(s), \theta(s))\, ds \tag{5}$$

Subject to:

$$x'(t) = f(x(t), \theta(t)) \tag{6}$$
$$x(0) = a \tag{7}$$
$$x(t) \in \mathcal{X} \subseteq \mathcal{R}^N \tag{8}$$
$$\theta(t) \in \Theta \subseteq R^M \tag{9}$$

where x and θ are the *state vector* and *control vector* of the system, respectively; $\mathcal{S}$ is the space of functions that the control must be chosen from during the minimization process and (7) - (9) give the initialization and constraint conditions that the state and control must satisfy.

We can discretize the problem represented by equations (5) - (9) by a variety of means. For now, let's use a very simple discretization scheme; replace the differentiations by forward differences and the improper integral in (5) by a simple Riemann sum evaluated at the left-hand endpoints. We will not concern ourselves about the convergence of the resulting infinite series at this time. The discretization process leads to the following problem:

$$\min_{\theta \in \mathcal{P}(\mathcal{S})} \quad \sum_{k=0}^{\infty} f_0\left(x(k\Delta t), \theta(k\Delta t)\right)\, \Delta t \tag{10}$$

Subject to:

$$\begin{aligned} x((k+1)\Delta t) &= x(k\Delta t) + f\left(x(k\Delta t), \theta(k\Delta t)\right)\Delta t && (11)\\ x(0) &= a && (12)\\ x(k\Delta t) &\in \mathcal{X} \subseteq \mathcal{R}^{\mathcal{N}} && (13)\\ \theta(k\Delta t) &\in \Theta \subseteq R^{M} && (14) \end{aligned}$$

where Δt indicate the size of the discrete time step and the controls θ must now lie in a space of piecewise continuous functions which we will denote by $\mathcal{P}(\mathcal{S})$. We can further simplify the notation by denoting $x(k\Delta t) \equiv x_k$, $\theta(k\Delta t) \equiv \theta_k$ and $F(x,\theta) \equiv x + f(x,\theta)\,\Delta t$. If we also assume that between time $k\Delta t$ and $(k+1)\Delta t$, the control θ has only a finite number of possible actions, we can replace the set Θ by the set $\Theta_q = \{A_1, \ldots, A_q\}$. Note that the number of possible control actions q is completely independent of the number of components in the control vector M. Finally, we can think of the function value $f_0\left(x_k, \theta_k\right)\,\Delta t$ as representing some measure of the worth of our control choice at the k^{th} time step, a measure that can be used to *reinforce* our belief in the quality of our choices. Hence, we will choose the relabeling $\mathcal{R}\left(x_k, \theta_k\right) = f_0\left(x_k, \theta_k\right)\,\Delta t$ and refer to $\mathcal{R}$ as the *reinforcement function*. Also, when convenient, we will simply use the notation $\mathcal{R}_k \equiv \mathcal{R}\left(x_k, \theta_k\right)$. This leads to the more compact representation of the control problem:

$$\min_{\theta_k \in A_q} \quad \sum_{k=0}^{\infty} \mathcal{R}\left(x_k, \theta_k\right) \tag{15}$$

Subject to:

$$\begin{aligned} x_{k+1} &= F\left(x_k, \theta_k\right) && (16)\\ x(0) &= a && (17)\\ x_k &\in \mathcal{X} \subseteq \mathcal{R}^{\mathcal{N}} && (18)\\ \theta_k &\in \Theta_q && (19) \end{aligned}$$

Now assume that we have already collected knowledge of the first $L-1$ states, controls and reinforcements; hence, $x_1,\ldots,x_{L-1}$, $\theta_1,\ldots,\theta_{L-1}$ and $\mathcal{R}_1(x_1,\theta_1),\ldots,\mathcal{R}_1(x_{L-1},\theta_{L-1})$ are known. The *measure* of our performance over all *future times* due to the *control actions taken at time step k* is

$$\mathcal{U}(x_k,\theta_k) \;=\; \sum_{j=k+1}^{\infty} \mathcal{R}(x_j,\theta_j) \tag{20}$$

and we will identify $\mathcal{U}_k \equiv \mathcal{U}(x_k,\theta_k)$.

In **Adaptive-Critic** neural architectures, two separate neural networks are used together to solve the problem represented by (15) - (19). We don't know the actual value of future performance that is captured in $\mathcal{U}(x_k,\theta_k)$, so we will try to *estimate* its value using what is called a **critic** network. The correct value of the control which should be chosen to minimize performance over all future times will be estimated by another network called the **action** network.

The output of the action network will be denoted by $\mathcal{J}(W,x,\theta,\mathcal{R})$, where W indicates the parameters that need to be updated via training. We will train the critic network to approximate $\mathcal{U}_k$. A schematic of the learning algorithm for the critic network is given in table 1; i is the index for the training set, j is the index for the weight update loop and W_j are the values of the weights in the critic network after j update steps. The parameters ξ and ζ are the relative *nonnegative* weightings attached to the future prediction and the current reinforcement.

Table 1.- CRITIC LEARNING ALGORITHM

1	$W_0 = 0, j = 0$
2	$i = 1$
3	Increment j
4	Set $W_j = W_{j-1}$
5	Input $x_i, \theta_i, \mathcal{R}_i$
6	Using the previous weights, W_{j-1} Calculate the desired target $D_i = \xi\mathcal{J}(W_{j-1}, x_{i+1}, \theta_{i+1}, \mathcal{R}_{i+1}) + \zeta\mathcal{R}_i$
7	Use the delta rule of section (2) to update the CMAC weights $\mathcal{J}(W_j, x_i, \theta_i, \mathcal{R}_i) = D_i$
8	Increment i
9	If $i < L-1$ Go To (5); Else Continue
10	If $W_j \neq W_{j-1}$ Go To (2); Else Continue

It is possible to implement the learning strategy presented in table 1 into an open-ended two-cycle algorithm as follows:

Note that the algorithm in table 2 adapts the critic network indefinitely, essentialy allowing

Table 2.- REAL-TIME LEARNING ALGORITHM

1	Choose x_0, θ_0
2	Compute $x_1 = F(x_0, \theta_0)$
3	Compute $\mathcal{R}_0$
4	Train $\mathcal{J}$ so that
	$\xi \mathcal{J}(W, X_1, \theta_1, \mathcal{R}_1) + \zeta \mathcal{R}_0 = \mathcal{J}(W, x_0, \theta_0, \mathcal{R}_0)$
5	Set $x_0 = x_1, \theta_0 = \theta_1$
6	Go To 2

for as large an L as desired. After $L-1$ states, controls and reinforcements have been processed and when the critic weights have converged to W, if all target values are satisfied, we have using $\mathcal{J}_i \equiv \mathcal{J}(W, x_i, \theta_i, \mathcal{R}_i)$:

$$\mathcal{J}_i = \xi \mathcal{J}_{i+1} + \zeta \mathcal{R}_i, \ 1 \leq i \leq L-2. \tag{21}$$

Applying (21) recursively, we obtain

$$\mathcal{J}_i = \xi^{L-i-1} \mathcal{J}_{L-1} + \zeta \left(\sum_{j=0}^{L-i-2} \xi^j \mathcal{R}_{i+j} \right), \ 1 \leq i \leq L-2. \tag{22}$$

Note that is $\xi = 1$ and $\zeta = 1$, for sufficiently large L, if the infinite series given by (20) converges, $\sum_{j=0}^{L-i-2} \mathcal{R}_{i+j} \approx \mathcal{U}_{i-1}$ and we have

$$\mathcal{J}_i \approx \mathcal{J}_{L-1} + \mathcal{U}_{i-1}, \ 1 \leq i \leq L-2. \tag{23}$$

The control vectors θ that are used in the critic network are obtained by either adapting another neural architecture called the *action* network or by classical techniques. Let's assume that a neural architecture whose output is labeled $\mathcal{A}_k \equiv \mathcal{A}(V, x_k, \theta_k, \mathcal{R}_k)$ is used to predict the correct control strateg θ_{k+1} for the next time step. Hence, the predicted value of our performance measure, $\mathcal{J}_{k+1}$, suppressing the dependence on W, becomes

$$\mathcal{J}(x_{k+1}, \theta_{k+1}, \mathcal{R}(x_{k+1}, \theta_{k+1})) = \mathcal{J}(x_{k+1}, \mathcal{A}(V, x_k, \theta_k, \mathcal{R}_k), \mathcal{R}(x_{k+1}, \mathcal{A}_k). \tag{24}$$

An efficient way of updating the weights in the *action* network is to compute the rates of change of the critic network's output with respect to the weights in the action network, $\frac{\partial \mathcal{J}_{k+1}}{\partial V_j}$, for each *action* weight V_j. This can be done via back-propagation techniques.

$$\frac{\partial \mathcal{J}_{k+1}}{\partial V_j} = \left[\frac{\partial \mathcal{J}_{k+1}}{\partial \mathcal{A}_{k+1}} + \frac{\partial \mathcal{J}_{k+1}}{\partial \mathcal{R}_{k+1}}\frac{\partial \mathcal{R}_{k+1}}{\partial \mathcal{A}_{k+1}}\right]\frac{\partial \mathcal{A}_{k+1}}{\partial V_j} \tag{25}$$

Once $\frac{\partial \mathcal{J}_{k+1}}{\partial V_j}$ is available for all j, the weights of the action network at each step $k+1$ can be updated in the standard way.

$$(V_j)^{new} = (V_j)^{old} + \lambda\left(\frac{\partial \mathcal{J}_{k+1}}{\partial V_j}\right)|_{V^{old}}, \tag{26}$$

where λ is a learning rate parameter.

If a CMAC architecture is used for the action network, the output $\mathcal{J}_{k+1}$ is not a differentiable function of the inputs $\mathcal{A}_{k+1}$ and $\mathcal{R}_{k+1}$ and equations (25) and (26) can not be used to determine new values of the action network parameters. Since action networks are used in our *truck backer-upper* simulations, we have chosen to implement the control update portion of the adaptive-critic design classically as follows:

$$\theta_{k+1} = \max_{\alpha \in \Theta_q} \mathcal{J}(W, x_{k+1}, \alpha, \mathcal{R}(x_{k+1}, \alpha)) \tag{27}$$

3.2 Truck Results:

We will consider the problem of forcing a cab and two wheeled trailer to backup up along a linear trajectory from a random, sometimes jack-knifed start, while subject to small noise disturbances. We use the usual variable formulation of this truck problem: α_1 is the angle between the center-line of the cab and the x axis; α_2, the angle between the center-line of the trailer and the x axis; β, the *wheel cut angle* or the angle between the front wheel direction and the center-line of the cab; (x_c, y_c), the coordinates of the center of the front edge of the cab and (x_t, y_t), the coordinates of the center of the back edge of the trailer. The angle between the center-lines of the cab and trailer is $\tau = \pi - (\alpha_2 - \alpha_1)$ and the cab-trailer combination is considered jacknifed if $\tau < \frac{\pi}{2}$ or $\alpha_2 - \alpha_1 > \frac{\pi}{2}$.

The state variables for this problem are $\alpha_1, \alpha_2, x_c, y_c, x_t$ and y_t. We choose $\tan(\beta)$ to be the control variable. We wish to pick wheel cut angles at each time step so that the cab-trailer combination successfully tracks the given linear trajectory.

The usual truck backer-upper problem discussed in the literature, e.g., Nguyen [9], considers the problem of finding a control strategy which can successfully back up the cab-trailer from randomly positioned starts to a given position on a horizontally oriented loading dock. Feed forward architectures are trained on progressively more complicated cab-trailer movements using *back propagation through time*. The simulations are very successful, but the training phase required many thousands of runs with correspondingly heavy use of computing resources.

We have used the techniques in section 3.1 to successfully solve our cab-trailer trajectory following problem using a critic network to predict the change in the distance from (x_t, y_t) to the given trajectory with the controls chosen via (27). Our simulations learn to follow the desired trajectory in minutes using a standard MS-DOS 386 PC as the hardware platform.

4 PATH PLANNING:

In this application, we study the problem of finding the optimal path or trajectory of a autonomous device through an obstacle field for a given start and goal position. The obstacle field is modeled by a finite array of time independent analog valued pixels. It is still very difficult to solve this problem efficiently in real world applications. Various algorithms have been proposed for calculating collision free paths through obstacle fields of either fixed or moving objects. Some *fast* algorithms rely on an algorithm design that is highly parallel in nature so that fine grained multi-processor systems can be used to compute the paths quickly, e.g. Hassoun [5]. Others such as Zhu [16] solve the planning problem at multiple scales of resolution in order to quickly find a reasonable approximate path.

Here, we discuss approximate optimal paths constructed using hierarchical methods which entail constructing a *coarse* resolution version of the original obstacle array and then use multipass dynamic programming to find an optimal *coarse* path. The dynamic programming computational engine requires knowledge of the transition costs associated with moving from one node to another. The transition costs associated with the original obstacle array are easy to calculate; however, the *coarse* transition costs associated with the *coarse* obstacle array are difficult to define. They must be calculated in such a manner that the correct qualitative information about the *fine* scale path movements is not lost in the coarsening process.

We have used clustering and filtering algorithms to predict these *coarse* transition costs, Peterson, [10] and feed forward neural architectures; **binary** obstacle fields are discussed in Peterson. [11] and these results are extended in Peterson [12, 13] to calculate an estimated analog cost for a given **analog** valued directional field either via finite sums of weighted binary feedforward networks or through feed forward networks trained to assign an analog directional cost to a given analog valued directional field. However, these methods are calculationally expensive; the training in particular was fairly difficult for these data sets.

In contrast to the above work, here we model the directional costs using CMAC architectures obtaining good qualitative transition cost information with neural architectures that are trainable in a matter of minutes to 10^{-2} *or better* RMS error.

4.1 Dynamic Programming:

Assume we have an obstacle array $\mathcal{P}$ of size $n \times n$ whose value at row i and column j, p_{ij}, can take on any value between 0 and 1. We need to know the cost of moving from a given pixel to its surrounding neighbors. The *transition* cost of moving in any of the directions east (E), northeast (NE), north (N), northwest (NW), west (W), southwest (SW), south

(S) or southeast (SE) is easy to compute. If we are at interior location (i,j) in $\mathcal{P}$, we can denote the surrounding locations by $(i+a, j+b)$, for $-1 \leq a,b \leq 1$, and compute the *transition* cost of moving from position (i,j) to position $(i+a, j+b) = (i',j')$ by $T_{ij;i',j'} = \frac{1}{2}(p_{ij} + p_{i',j'})\sqrt{(a^2+b^2)}$. All transition costs that correspond to moves out of the $\mathcal{P}$ are set to infinity.

Then, given a **start node**, $S \equiv (i_s, j_s)$ and a **goal node**, $G \equiv (i_g, j_g)$, we want to find the minimum cost path through $\mathcal{P}$ from S to G, $C_{S,G,\mathcal{P}}$. *Dynamic Programming* is a technique which will calculate $C_{S,G,\mathcal{P}}$ efficiently. For our problem here, we allow movement in eight (8) directions which are divided into two distinct classes: $\Omega_1 = \{E, NE, N, SE\}$ and $\Omega_2 = \{W, NW, S, SW\}$. From our earlier notation conventions, there are associated sets of indices a and b which give rise to these direction sets, I_1 for Ω_1, and I_2 for Ω_2. Let C_{ij} denote the minimum cost of moving through $\mathcal{P}$ from node (i,j) to G with initial values of infinity with the exception of the goal cost, C_{i_g,j_g}, which is set to zero. For the set Ω_1 directions, start the calculations in the first row and last column of $\mathcal{P}$. We compute the cost values C_{ij} in the last column by moving down through the column and applying **Bellman's Principle of Optimality**, equation (28), at each node.

$$C_{ij} = \min\{C_{ij}, \min\{T_{ij;i+a,j+b} + C_{i+a,j+b} : (a,b) \in I_1\}\} \tag{28}$$

Once the last column is finished, we switch to the top of the next to the last column and move down it until finished. In this way, the cost of moving through the $\mathcal{P}$ from any position (i,j) to G is calculated and stored in a cost matrix C. At this point, no directions in Ω_2 have been used. The next set of directions is implemented similarly. This time, because the directions are essentially left and down movements, the process starts in the first column and last row position and move upwards through the first column. Upon completion of the first column, we switch to the bottom row and second column position and move up the second column. The principle of optimality is the same as given in (28) except that the index set I_1 is replaced by I_2. The **Multipass Dynamic Programming** algorithm combines the operations using the two sets of directions into an iterative procedure in the following way: *first*, compute a pass using direction set Ω_1 and *second*, compute another pass using direction set Ω_2. As long as the costs C are still changing, repeat these two passes; otherwise, stop.

4.2 Coarse Optimal Paths:

Once a random obstacle field is constructed, [12] we construct the coarse obstacle array by overlaying the fine scale array with two additional grids of size $\frac{n}{2} \times \frac{n}{2}$ and $\frac{n}{4} \times \frac{n}{4}$, respectively. The **coarse** obstacle array corresponds to the coarser of these two grids and reduces the number of active nodes in the path planning problem from n^2 to $\frac{n^2}{16}$. The intermediate mesh consists of boxes each of which contains four (4) fine scale squares. which are subdivided it into eight fine scale triangles or **sectors** labeled as shown in Figure 4.2.

Thus, each box in the intermediate grid contains eight fine scale sectors; each block in the coarse grid contains four intermediate boxes of eight fine scale sectors each for a

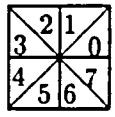

Figure 1.- Sector Subdivisions

total of thirty-two individual sectors. The **coarse** blocks can themselves be subdivided into eight sectors; each **coarse** sector contains four **fine scale** sectors. Each intermediate box can be thought of as a node in an intermediate scale path planning problem by assigning to the eight fine scale sectors within the box the pixel values of the fine scale square that they lie within. Each sector then corresponds to a triangular pixel whose value is an analog height. Further, each **coarse** sector contains four such intermediate sector values. Now each interior coarse block is surrounded by eight other coarse blocks. If we identify each block as a *coarse* node, we can use multipass dynamic programming on the smaller $\frac{n}{4} \times \frac{n}{4}$ array to find a *coarse* optimal path as long as we can find a way of assigning a transition cost for all eight of the possible directions in the sets Ω_1 and Ω_2.

For each desired direction in this "coarse" setting, we define *direction fields* as indicated in Figure 4.3 for the specific cases of the east and northeast directions. The E, N, W and S direction fields consist of 16 fine scale triangles, while the NE, NW, SW and SE direction fields consist of 24 such triangles.

In Peterson [11], these triangles are binary valued and represent an obstacle of height 1 or an empty region in the obstacle array. Hence, each fine scale triangle is modeled as an on-off event, taking the values 1 or 0. The first type of field is called a *straight* field and the second, an *angled* field. For each *straight* direction, each fine scale triangle in that direction's field is an *input*. Thus, in the **binary** case, for each *straight* direction, we need to assign to each $\vec{u} \in 2^{16}$, one of two possible outcomes; a 1 if there is a path through the particular direction field that the $\vec{u}$ represents, and a 0, otherwise. There are therefore 2^{16} possible *straight* fields for a given *straight* direction and 2^{24} possible *angled* fields for a given *angled* direction. On the other hand, in the analog case, we want to assign to each $\vec{u} \in [0,1]^{16}$ an outcome also in $[0,1]$ which represents the directional cost.

4.3 Neural Architectures:

Following Peterson [11, 12, 13], feed forward architectures were designed to "learn" both the patterns that correspond to free paths and also, the patterns that correspond to no free paths in a given direction. For the *straight* direction fields, we chose to use a feed forward network architecture with 16 input neurons, 9 hidden neurons and 1 output neuron. This architecture will be denoted a $16-9-1$ FFN for notational convenience. The *angled* direction fields were modeled using a $24-11-1$ FFN. In the **binary** case, the 0 or 1 path outcomes were determined by visual inspection for 502 examples of each type of direction field. This data was then split into 350 *training* and 152 *testing* examples or exemplars, which consist of pairs of binary direction fields and their associated binary costs.

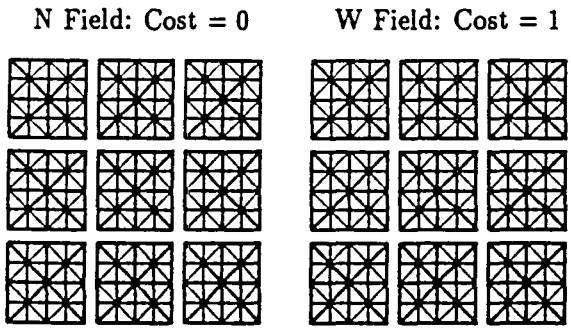

Figure 2.- Coarse Transition Cost Fields

The training results for the eight coarse transition cost feed forward networks for binary valued direction fields are discussed in Peterson. [11] These binary networks averaged 96.2% recognition on the 350 elements in the training sets and 80.0% recognition on the 152 samples in the training sets.

The cost calculations were extended to the analog case in Peterson. [12] Let $\mathcal{D}$ be a *binary* valued direction field of N pixels and let $f : \mathcal{D} \rightarrow [0,1]$ be a feed forward network of the type discussed above. Then the number of pixels, N, in each direction field is either 16 or 24 depending on whether $\mathcal{D}$ represents an *angled* or *straight* field and the network f tries to assign to each $\mathcal{D}$ a binary coarse direction cost of 0 or 1. We will use the network f to define a coarse transition cost for a direction field $\mathcal{E}$ which consists of N analog valued pixels, $p_1, \ldots, p_N$, whose values lie between 0 and 1.

From the original field $\mathcal{E}$, we can construct approximations, $\mathcal{E}^M$, as follows. For a given positive integer M, each pixel value p_i will then be in one of the mutually exclusive sets $[\frac{j-1}{M}, \frac{j}{M})$, $1 \leq j \leq M-1$ or $[\frac{M-1}{M}, 1]$. Hence, for each M, we can determine *approximate* direction fields, $\mathcal{E}^M$, where each pixel value is discretized to lie in one of M+1 values. We will label the pixel values lying in each $\mathcal{E}^M$ by p_i^M, where $p_i^M \in \left\{0, \frac{1}{M}, \ldots, \frac{M-1}{M}, 1\right\}$. We then construct *clipped* copies of the direction field $\mathcal{E}^M = \left\{p_1^{jM}, \ldots, p_N^{jM}\right\}$, where $p_i^{jM} = 0$ if $p_i^M < \frac{j}{M}$ and 1 otherwise. The *clipped* direction fields $\mathcal{E}_j^M$ are binary valued direction fields and we can compute $f(\mathcal{E}_j^M)$ for all j, $1 \leq j \leq M$. Following Peterson [12], the cost assessed for an analog valued direction field $\mathcal{E}^M$ consisting of M discrete levels of pixel values is then defined to be

$$C^M = \frac{\sum_{j=1}^{M} f(\mathcal{E}_j^M)}{M}. \tag{29}$$

For a given obstacle array, the associated coarse array contains many nodes which have well defined coarse transitions for all or some of the movement directions. The procedure outlined above permits us to use equation (29) to compute the estimated analog cost for each direction field for a given choice of gray scale M. Thus, each random obstacle array provides a wealth of training and testing data. There are then three generated paths of

interest, each of which is a matrix of 0's and 1's, with a 1 indicating that the path goes through that node and a 0, that the node is not in the path. First, $\mathcal{P}_{\mathcal{F}}$, the fine scale path; second, $\mathcal{P}_{\mathcal{FA}}$, the coarse path implied by $\mathcal{P}_{\mathcal{F}}$, where a coarse node is part of this path if at least one node in the fine scale path contained in the coarse node and third, $\mathcal{P}_{\mathcal{A}}$, the coarse scale path. The distance between $\mathcal{P}_{\mathcal{FA}}$ and $\mathcal{P}_{\mathcal{A}}$ indicates how reasonably our approximation methods work. We use the following distance measure, where (i,j) and (k,m) are the (row,column) indices of the path matrices.

$$\rho(\mathcal{P}_{\mathcal{FA}}, \mathcal{P}_{\mathcal{A}}) = \max_{\mathcal{P}_{FA}^{ij} > 0} \min_{\mathcal{P}_{A}^{km} > 0} \sqrt{((i-k)^2 + (j-m)^2)} \tag{30}$$

The directional cost information calculated using the method above generates very reasonable paths. For a 100 randomly generated 80×80 obstacle fields using gray scale $M = 20$, the associated coarse fields were 20×20 and the average $\rho(\mathcal{P}_{\mathcal{FA}}, \mathcal{P}_{\mathcal{A}})$ distance was 1.69. This indicates that a reasonable corridor can be chosen by using the coarse path as a centerline and then padding out a distance of 1 to 2 coarse blocks on either side. This removes substantial amounts of the original search space thereby lessening the computational burden of the obtaining the fine scale multipass dynamic programming solution in the corridor; at the same time, we have high confidence that we have successfully identified the correct region in the original obstacle array where the fine scale path resides.

The method outlined above provides a reasonable way to compute an estimate to the approximate analog transition costs for the obstacle avoidance problem. However, it is fairly expensive to perform the calculations suggested by equation (29). In Peterson [13], training and testing sets of analog direction fields and their associated analog costs were generated using 16 gray scales using the same feed forward architectures as in the binary case discussed above. The training results for the eight coarse transition cost feed forward networks for analog valued direction fields are summarized in Table 3. Each direction was trained using $395 - 445$ exemplars and tested on a different set of $50 - 100$ exemplars. The training and testing sets here consist of pairs of analog direction fields and their associated analog costs; the term RMS refers to the *Root Mean Square* error.

Table 3.- ANALOG TRANSITION COST FFN's

	E	W	N	S	NE	NW	SW	SE
RMS Train	.04	.07	.05	.06	.05	.05	.05	.06
RMS Test	.14	.18	.10	.17	.09	.11	.23	.10

The approximate paths generated via this method were also quite good, in spite of the relatively poor RMS errors on the testing sets. However, it was very difficult to train this data. In the rest of this work, we explore an alternative neural architecture for learning the approximate directional cost mappings which has very fast learning and sufficient generalization to also provide good performance on path generation.

4.4 CMAC Architectures:

We now use the CMAC architecture as described in 2 to estimate the directional costs required for the generation of the coarse obstacle path. The input-output maps we wish the CMAC architectures to "learn" are those discussed in section 4.3. For convenience of expostion, we will concentrate on the east direction input-output map; the input set here is a subset of R^{16} and the output set is $[0,1]$. For these experiments, the underlying direction field $\mathcal{D}$ is represented by a M gray scale approximation, which in the notation of section 4.3 is labeled $\mathcal{E}^M$. Thus, the allowable values of each component of the direction field are $\frac{j}{M}$, for $0 \leq j \leq M$. The output that is assigned to each such approximate direction field is the output calculated by the techniques given in section 4.3. This is precisely the I/O map whose training results for a $16-9-1$ *east* FFN are presented in table 3 for the case $M = 16$. The CMAC architecture for the E direction is identical to that used for the N, S and W directions; the NE, NW, SW and SE I/O maps are structured very similarly.

The input space for the east CMAC was **coarse encoded** as follows. Each component of the input lives in $[-.1, 1.1]$. The offset base β was constant for all input components and all receptive field widths were fixed at w. The offset base and sensor width used for all of the straight, E, N, W, and S, CMAC architectures and those for the angled direction fields, NW, NE, SW and SE, are given in table 4. Now pick a given direction field sample. For a given level j each component p_i of input $\vec{p}$ lies in a **unique** subinterval component a_j. Hence, the 16 inputs of $\mathcal{E}^M$ can be mapped to a 16-tuple of integers $\{a_1, ..., a_{16}\}$.

Table 4.- CMAC ARCHITECTURE

	L	β	w
Straight	10	0.1	0.60
Angled	20	0.05	0.60

We chose a uniform hash size of 1024 for all levels. Thus, each input direction field is assigned L weights and the working memory is organized into a two dimensional array of real numbers of size $L \times 1024$. The output of each CMAC and its training rule were implemented as noted in section 2. In the results below, all RMS errors on training are based on the raw CMAC outputs, but the CMAC output is clipped to lie in $[0,1]$ before being used in path planning calculations.

4.5 Training Results:

The following simulation results are from the CMAC simulation code developed at the NASA Johnson Space Center. The training samples were obtained from randomly generated 40×40 fine scale arrays with associated 10×10 coarse arrays. We obtained 90 samples per obstacle array for the straight directions and 81 samples for angled directions. We used a gray scale of $M = 20$. The CMAC architectures were trained on each of these sample sets, then a new random obstacle field was generated. This process was run 100 times, giving

a total of 9000 and 8100 potentially different training samples, however, on these runs, we typically see about 25% repeats.

The 89th training run is indicated below in table 5; all runs were limited to 10 training updates; R_0 and R_1 are the initial and final RMS errors and M_0 and M_1 are the initial and final maximum absolute errors.

Table 5.- CMAC TRAINING

	E	N	W	S	NE	NW	SW	SE
R_0	.131	.127	.115	.156	.137	.214	.197	.143
R_1	.0004	.0029	.0008	.002	.0004	.0021	.00084	.0034
M_0	.618	.51	.42	.787	.458	.753	.58	.452
M_1	.0037	.019	.0078	.014	.002	.011	.0049	.03

The procedure used above to generate training samples was then used to generate another 40 sets of directional data; for this set, all the data was saved into one file per direction. The straight directional data thus consisted of 3600 samples, 40 runs at 90 samples per run; the angled data consisted of 3240 samples, 40 runs at 81 samples per run. The performance of the trained CMAC's was then checked on these testing sets. These results are listed in table 6.

Table 6.- CMAC TESTING

	E	N	W	S	NE	NW	SW	SE
R_0	.305	.259	.387	.312	.199	.387	.261	.185
R_1	.150	.133	.154	.158	.158	.220	.20	.70
M_0	.95	.385	.95	.864	.85	.897	.950	.155
M_1	.84	.806	.91	.981	.863	1.205	.948	.909

The directional cost information calculated using the CMAC architectures also generates very reasonable paths. For a 100 randomly generated 80 × 80 obstacle fields, the associated coarse fields were 20 × 20 and the average $\rho(\mathcal{P}_{\mathcal{FA}}, \mathcal{P}_{\mathcal{A}})$ distance was 1.62. The approximate paths generated via this method were very good, in spite of the relatively poor RMS errors on the testing sets listed in table 6.

5 REFERENCES:

1. Albus, J. 1975. "A New Approach to Manipulator Control: The Cerebellar Model Articulation Controller (CMAC)." *J. Dynamic Systems, Measurement and Control*, 220- 227.

2. Albus, J. 1975. "Data Storage in the Cerebellar Model Articulation Controller (CMAC)." *J. Dynamic Systems, Measurement and Control*, 228 - 233.

3. Albus, J. 1979. "Mechanisms of Planning and Problem Solving in the Brain." *Math. Biosciences*, Vol. 45, 247 - 293.

4. Barto, A., R. Sutton and C. Anderson. 1983. "Neuronlike Adaptive Elements That Can Solve Difficult Learning Control Problems." *IEEE Trans. Systems, Man and Cybernetics*, Vol. SMC-13, No. 5, 834 - 846.

5. Hassoun, M. H. and A. Sanghvi. 1990. "Fast Computation of Optimal Paths in Two- and Higher Dimensional Maps", *Neural Networks*, Vol. 3: 355 - 363.

6. Miller, W. 1987. "Sensor-Based Control of Robotic Manipulators Using as General Learning Algorithm." *IEEE J. Robot. Automat.*, Vol RA-3, No. 2, 157 - 165

7. Miller, W. 1989. "Real Time Application of Neural Networks for Sensor Based Control of Robots with Vision." *IEEE Systems, Man and Cybernetics*, Vol. 19, 825 - 831.

8. Miller, W., F. Glanz and L. Kraft, III. 1990. "CMAC: An Associative Neural Network Alternative to Backpropagation." *Proceedings of the IEEE*, Vol. 78, No. 10, 1561 - 1567.

9. Nguyen, D. and B. Widrow. 1990. "Neural Networks for Self-Learning Control Systems", *IEEE Control Systems Magazine*, Vol. 10, No. 3, 18 - 23.

10. Peterson, J. 1991. "Obstacle Avoidance Using Hierarchical Dynamic Programming.", *The Proceedings of the 23rd Southeastern Symposium on System Theory*, March 1991.

11. Peterson, J. 1991. "Obstacle Avoidance Using Neural Networks and Hierarchical Dynamic Programming.",*Proceedings of the 2nd Workshop on Neural Networks: Academic/Industrial/NASA/Defense*, Society for Computer Simulation.

12. Peterson, J. 1991. "Path Planning in Analog Valued Obstacle Arrays Using Hierarchical Dynamic Programming and Neural Networks", submitted to *Artificial Neural Networks in Engineering and Science*, to be held St. Louis, Missouri, November 1991.

13. Peterson, J. 1991. "Estimating Directional Cost Information in Analog Obstacle Fields Using a Single Neural Network", submitted to *Neural Information Processing Systems*, to be held Denver, CO, December 1991.

14. Werbos, P. 1990. "Consistency of HDP Applied to a Simple Reinforcement Learning Problem", *Neural Networks*, Vol. 3, 179 - 189.

15. Werbos, P. 1990. "A Menu of Designs for Reinforcement Learning Over Time", in **Neural Networks for Control**, ed. Miller, Sutton and Werbos, 67 - 96.

16. Zhu, D. and J. Latombe. 1991. "New Heuristic Algorithms for Efficient Hierarchical Path Planning." *IEEE Trans. Robotics and Automation*, Vol. 7, No. 1, 9 - 20.

TOTAL QUALITY MANAGEMENT: ANALYSIS, EVALUATION & IMPLEMENTATION WITHIN ACRV PROJECT TEAMS

Final Report

NASA/ASEE Summer Faculty Fellowship Program--1991

Johnson Space Center

Prepared by:	Laura B. Raiman, Ph.D.
Academic Rank:	Assistant Professor
University & Department:	Pennsylvania State University Department of Industrial & Systems Engineering University Park, PA 16802
NASA/JSC	
Directorate:	New Initiatives Office
Division:	ACRV Project Office
Branch:	n/a
JSC Colleague:	Brian K. Kelly
Date Submitted:	August 9, 1991
Contract Number:	NGT-44-001-800

ABSTRACT

Total Quality Management (TQM) is a cooperative form of doing business that relies on the talents of everyone in an organization to continually improve quality and productivity, using teams and an assortment of statistical and measurement tools. The Assured Crew Return Vehicle (ACRV) Project Office was identified as an excellent project in which to demonstrate the applications and benefits of TQM processes. As the ACRV program moves through its various stages of development, it is vital that effectiveness and efficiency be maintained in order to provide the Space Station Freedom crew an affordable, on-time assured return to Earth. A critical factor for the success of the ACRV is attaining the maximum benefit from the resources applied to the Program.

Through a series of four tutorials on various quality improvement techniques, and numerous one-on-one sessions during the SSF's 10-week term in the Project office, results were obtained which are aiding the ACRV office in implementing a disciplined, ongoing process for generating fundamental decisions and actions that shape and guide the organization. Significant advances were made in improving the processes for two particular groups - the correspondence distribution team and the W.A.T.E.R. Test team. Numerous people from across JSC were a part of the various team activities including Engineering, Man Systems, and Safety. The work also included significant interaction with the support contractor to the ACRV Project. The results of the improvement activities can be used as models for other organizations desiring to operate under a system of continuous improvement. In particular, they have advanced the ACRV Project Teams further down the path of continuous improvement, in support of a working philosophy of Total Quality Management.

INTRODUCTION

Total Quality Management (TQM) is a cooperative form of doing business that relies on the talents of everyone in an organization to continually improve quality and productivity, using teams and an assortment of statistical and measurement tools. JSC management has made a commitment to understanding TQM techniques, and to implementation within JSC organizations. The ACRV (Assured Crew Return Vehicle) Project Office was identified as an excellent project in which to demonstrate the applications and benefits of TQM processes. As the ACRV program moves through its various stages of development, it is vital that effectiveness and efficiency be maintained in order to provide the Space Station Freedom (SSF) crew an affordable, on-time assured return to Earth. The challenge is magnified by an increasing pressure to adhere to schedule, cost and technical objectives. A critical factor for the success of the ACRV is attaining the maximum benefit from the resources applied to the Program.

This paper documents the work performed over a 10 week period which involved examining and assessing the processes being utilized by the ACRV Project teams from a total quality perspective. A major portion of this work involved determining specifically where certain statistical tools would be appropriate, and demonstrating their application. Major areas of interest included ACRV testing techniques, probability of mission success (POMS), operational availability (A_o), and strategic planning. The results from this study are aiding the ACRV office in implementing a disciplined, ongoing process for producing fundamental decisions and actions that shape and guide the organization. The resulting activities of the ACRV Project teams will serve as models for other organizations which are attempting to use TQM effectively to anticipate and respond to changing environments.

METHODS IMPLEMENTED FOR IMPROVEMENT ACTIVITIES

The activities conducted over the summer were supported by a series of four tutorials presented by the Summer Faculty Fellow (SSF). After discussions with ACRV Project Office managers and team members concerning Project Office activities and methods, the SSF decided that it was necessary to provide training in some of the quality analysis techniques. Once training was completed in each area, the existing knowledge of the team members could be integrated with the new analysis techniques in order to achieve a direct application of the numerous quality improvement techniques. This immediate application not only

helps implant a solid understanding of each technique, but also generates enthusiasm since people have the opportunity to immediately apply new techniques. The four tutorials presented were as follows: TQM: Philosophy & Tools; Design of Experiments; Quality Function Deployment; and Benchmarking. (Copies of the materials presented in these tutorials may be obtained by contacting the SSF or the ACRV Project Office). The contents of each of the four topics are described below.

TQM: Philosophy & Tools

Process improvement is aided by viewing an organization as a network of linkages of processes run by internal producers and customers of output. The ultimate output of this network is the product or service provided to an external customer. Quality and productivity are improved as producers work in teams with their suppliers (internal and external) to improve internal customer satisfaction and hence external customer satisfaction. The focus of quality improvement therefore, must be on identifying and improving the key processes in each function of each department in an organization. Incremental process improvements must be made on an ongoing basis. The strategy for achieving these process improvements involves three major activities: 1) selecting the process, 2) documenting the current knowledge of the process, and 3) using an improvement cycle to increase the knowledge of the process. A basic model (developed by Associates in Process Improvement) for process improvement is shown in Figure 1.

The last activity in the strategy is the iterative use of the improvement cycle. The use of this cycle is meant to increase users' knowledge of a process. This cycle is also referred to as the Shewhart Cycle, Deming Cycle, and plan-do-check-act (PDCA) Cycle. In order to step through this cycle for any particular process, there are a number of quality improvement tools that may be used. The tutorial covered the use of seven of these tools: flowcharts, cause and effect diagrams, pareto charts, check sheets, histograms, control charts and scatter diagrams. These tools may be used for collection of data and/or analysis of data and information.

The final portion of this tutorial covered the concept of variation. It is vital that all team members understand some of the basic statistical concepts needed to interpret variation. They must be able to determine whether the patterns of variation that are observed are indicative of a trend or of random variation that is similar to what has been observed in the past. This distinction between

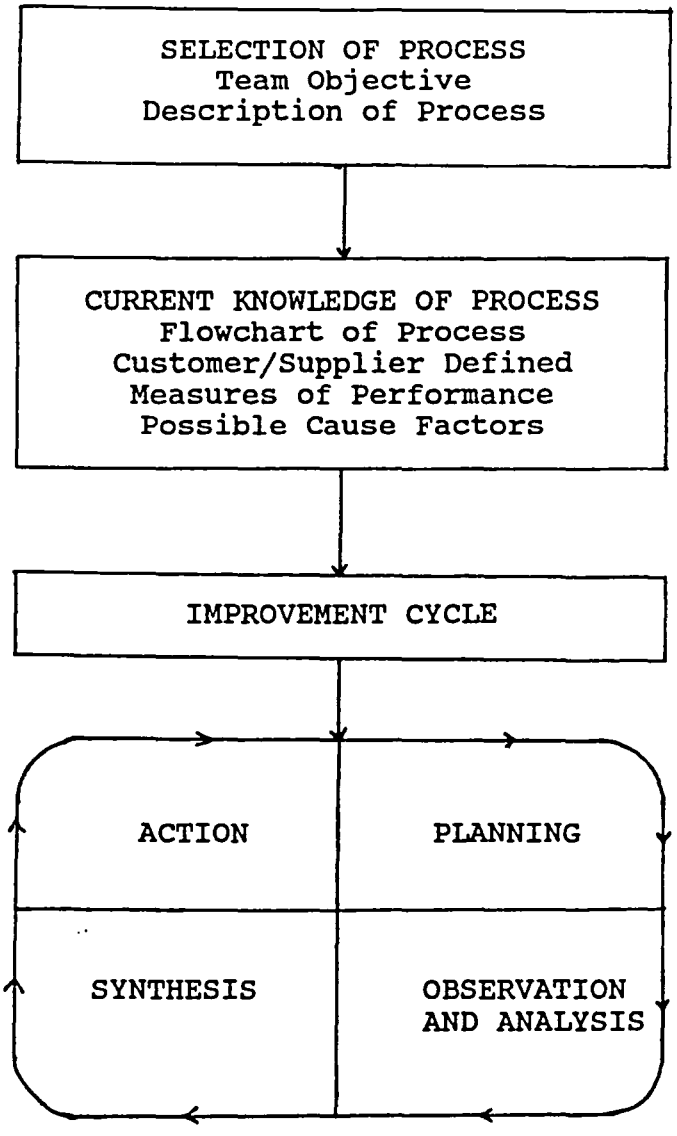

Figure 1.- Strategy for Process Improvement

patterns of variation is necessary to minimize the losses resulting from the misinterpretation of the patterns. These losses ca be minimized by understanding that variation can be caused by either common or special causes, by knowing how to determine whether a system is stable or not, and by basing action on this analysis.

Design of Experiments

This tutorial covered the basics of effective experimentation. Without knowledge of statistical experimental procedure, experiments are often performed in such a way that some (or perhaps all) important questions cannot be answered. Because of the possibility of performing an ill-advised set of experiments, questions of design must be considered at the start of an experimental program. Classical approaches to experimental design, including full factorial designs and fractional factorial designs, allow for consideration of both statistical accuracy and cost. Statistical accuracy involves the proper selection of the response to be measured, determination of the number of factors that influence the response, the selection of the subset of these factors to be studied in the experiment being planned, the number of times the basic experiment should be repeated (replicated), and the form of the analysis to be conducted. To minimize the cost of an experimental investigation, usually it is preferable to choose the simplest experimental design possible and to utilize the smallest sample size consistent with satisfactory results. Fortunately, most simple experimental designs are both statistically efficient and economical.

Using the classical designs as a foundation, the basics of Taguchi Methods for Experimentation were also covered. The ideas of system design, parameter design and tolerance design were all included in this discussion. The idea of the Taguchi Loss Function was also presented, allowing for a discussion of impact of quality improvements on cost.

Quality Function Deployment

This tutorial covered the basics of QFD. This included a general exposure to the basic QFD methodology, including the "House of Quality". The House of Quality provides for complete analysis of the basic relationship matrix which relates customer needs to specific design concepts. This analysis includes a competitive evaluation, and interaction matrix relating the design concepts to one another, and the development of measures for each of the design concepts. QFD helps to integrate all of the corporate functions in being responsive to customer requirements so that product planning, product design, process planning and production planning provide a coherent response to the customer needs that achieves value and satisfaction for the customer. QFD plays a major role in achieving products that have reduced cost, better quality, features that satisfy customer's needs, and are developed in a significantly shorter

development time. As a result, the products are intrinsically much more appealing to potential customers.

Discussion of QFD concepts during the tutorial were extensive under the area of requirements. Possible applications were identified which included: relating the SPRD requirements to the three mission segments; relating the SPRD requirements to the detailed contractor requirements; defining customer requirements for computer needs in the next phases of the Project, and subsequently defining requirements for the systems which will be used to fulfill these requirements.

Benchmarking

This tutorial covered the general concepts included in Benchmarking. In simple terms, benchmarking is the continuous process of measuring products, services and practices against the toughest competitors, or those companies recognized as industry leaders. Benchmarking techniques allows the user to analyze what, why, and how leading companies have done, to earn their leadership position. Benchmarking activities must look into the future, not just the present. In order to achieve world class performance tomorrow, a company must not only eliminate the current Benchmark gap, but also must improve performance such that they surpass the current bast practices in the future by setting a new standard.

The 10-step process Xerox developed to accomplish Benchmarking was presented, and an example of the techniques used by Motorola to achieve and maintain their standing as a world class company. While discussing these issues, a good period of time was spent brainstorming on who the customers are for ACRV, what companies should be considered when benchmarking processes in JSC, and how to ensure that a benchmark gap is not just filled in the present, but that world class levels are surpassed in the future.

IMPLEMENTATION OF QUALITY IMPROVEMENT TECHNIQUES

Two major team improvement activities, and implementations of quality improvement techniques occurred over the 10-week period. The first involved one team's trip through the process improvement cycle, and the second involved the improvement of test matrix design for a major testing effort. Descriptions of both of these improvement efforts are given below.

Correspondence Distribution Team (CDT)

This effort involved a team of 5 people - two NASA/ ACRV personnel, and three support contractor (Eagle Engineering) personnel. The first effort of the CDT was to describe the process to be examined. The process included all correspondence distribution once it was received at the front door of the ACRV office. This included regular mail, NASA mail, faxes, electronic mail and drop-offs. The problem was that too much unnecessary paper was crossing the desk of the project manager and his secretary. As a result, important information might get lost in the mass of paper, specific correspondence could get misplaced and as a result require hours to track it at a later date.

The first step in the improvement process, after getting the team together, was to hold a brainstorming session to flowchart the existing process. In a two-and-a-half hour session, the team brainstormed all of the steps in the correspondence distribution process, they then reorganized all of the steps into flowchart form. The current flowchart was then typed up and distributed to team members. The team took one week to evaluate the flowchart, make the necessary changes, and think of ways to improve the process. One week later, members of the team got back together to brainstorm improvement ideas. A significant number of ideas were presented to help eliminate the amount of paper going across the manager's desk. After all of the improvement ideas were documented and discussed, a new flowchart was generated which incorporated the process revisions.

The final step in the improvement process for the CDT will be to implement the improvement ideas. The team got together one last time to review the improved distribution process, and make any last changes. The improved process was then presented to the manager. In addition to the numerous improvements made to the correspondence distribution process, there were also a number of other valuable aspects to the team activities. Team members gained ownership of their process, and as a result everyone understood the entire process to a much greater extent than going into the team activities. This also meant that all team members had strong buy-in to all suggested improvements.

A valuable customer/supplier relationship was strengthened since team members were not all direct NASA ACRV Project Office employees. The result of this was elimination of some barriers that previously existed between the contractor and the Project Office. Three team members

represented the support contractor to the Project Office, and therefore filled a "supplier seat" on the CDT. Members also realized the value of working as a team - recognizing that the sum of everyone's ideas is greater than what could be accomplished individually. The final benefit was the excitement generated as a result of this team's activities. Enough interest was generated that the support contractor requested the SSF to make a presentation to their top management on TQM and related tools. This step cannot help but strengthen the working relationship between the support contractor and the Project Office.

Wave Analysis & Test of Extraction Requirements (WATER) Test Plan

The second major team effort accomplished during the 10-week period was the effective design of the WATER test plan, which focuses on the post-landing phase of the ACRV mission. While the decision to bring the ACRV down to land-landing site or a water-landing site has not been made, the WATER evaluation focuses on the specific post-landing dynamics of a water-landing vehicle. The development of a full scale, generic ACRV mockup is the centerpiece of the crew egress evaluation. A substantial amount of research resulted in the capability of the mockup to simulate the water dynamics of both the Apollo and a NASA study vehicle concept, SCRAM. An entire week of unmanned testing is planned, which is devoted to the development of an engineering motion analysis database. An additional set of testing evaluations are planned to focus on the manned aspects of ACRV water recovery.

The purpose of the second tutorial on Experimental Design was to expose the WATER team members to the concepts behind effective and efficient experimentation methods. The engineering (unmanned) portion of the test deals with a large number of input variables including: horizontal C.G., vertical C.G., weight, sea state, and vehicle configuration. The response variables include static draft, flotation attitude, and pitch amplitude after disturbance. Dynamic response measures include pitch amplitude, heave amplitude, surge amplitude, yaw rate, and wave run-up magnitude. The Medical/Man Systems (manned) portion of the test deals with input variables including vehicle configuration, wave state, hatch location, and crew composition (mixture of deconditioned and ill/injured crewmembers). Each of the test levels for all the input variables had to be determined, and an effective testing scheme for combining these levels into an effective test scheme also had to be examined.

During the course of the tutorial, and individual one-on-one sessions, the members of the WATER Team were exposed to different test designs. The differences between one-at-a-time testing and orthogonal, balanced designs were thoroughly examined. Significant time was also spent discussing how to integrate the engineering and medical/man systems test objectives for the week of combined testing, in order to obtain useful data that can be used effectively to make useful characterizations.

The WATER test plan is still in the planning phase. Actual experimentation is expected to take place in late '91 or early '92. Followup work between the SSF and the ACRV Project Office will continue to examine both the design and issues involved in the WATER Test. Some preliminary test design analysis may also be examined using the 1/20th scale wave tank and ACRV models prior to the actual WATER Tests.

Miscellaneous Engineering Probability Analysis Issues

An additional assortment of engineering/reliability issues were examined during the summer. The first involved generating a landing error probability distribution, given engineering simulated footprints. Initial engineering studies were performed to estimate the targeting accuracy to a landing point of a range of ACRV configurations due to navigation, entry guidance, and parachute drift dispersions. The configurations varied in types of navigation aids employed, vehicle lift-to-drag (L/D) ratios, and parachute characteristics. From this study, an overall summary of landing footprints was provided to the SSF. This information was then used to generate a two-dimensional probability distribution which characterized the probability of landing over a given region.

Using information obtained on obstacle coverage at two specified landing sites, a probability distribution for the obstacles was also generated. When these two probability footprints were used in conjunction, it resulted in the capability of estimating the probability of the ACRV hitting an obstacle upon landing. This measure is an important factor in the overall probability of mission success.

The general ideas used for in conjunction with the above problem were also used to analyze some slightly different situations. The first one involved using historical landing data from the Apollo landings to generate confidence intervals on targeting error. The second application involved the development of a technique to evaluate the probability of surviving debris from reentry

hitting a person upon landing. The generation of the probability distributions for this method were similar to those used for landing footprint distributions. The final problem investigated was evaluating the effects of wind profiles specifically on landing error footprints. The purpose of this investigation was to determine if retargeting the ACRV based on wind profile information would cause a significant reduction in the size of the landing error footprint. This final problem is still under investigation.

CONCLUSIONS

There are a number of notable results which occurred as a result of all of the above improvement activities. In general, the members of the ACRV Project Office teams have gained a better understanding of TQM - not just as a philosophy, but also as knowledge of the tools available to support the philosophy. This has more people thinking about the available tools, and possible applications in the work and processes of the Project Office. The tutorials and the supplementary statistical work provided engineers supporting the ACRV, and Project Office members with a strengthened statistical awareness, and understanding of the use of probability distributions.

Many members of the Project Office expressed a strong interest in finding more applications, and continuing the quality improvement activities so that knowledge of the tools is not lost. For two of the Project Office Teams - Correspondence Distribution and WATER Test - there is greater team ownership, and significant improvements have been made in the processes evaluated by each of the teams.

Another added benefit coming from the tutorials and improvement activities is an increased interest on the part of the support contractor to the ACRV Project Office, and various NASA support organizations. The support contractor, Eagle Engineering, received a tutorial on TQM philosophy and tools, and are looking at how to implement TQM in their own processes. This activity will directly benefit the ACRV Project Office, since they are a customer of Eagle. With regard to the NASA support organizations, the summer activities included people from many Directorates including Engineering, S,R & QA, Man Systems, and Medical personnel. The involvement of all of these ACRV support people improves internal customer/supplier relationships, helps provide some focus on internal processes as well as external, and provides many additional people with direct experience working with TQM tools, and operating under the corresponding philosophy.

Improving product or service quality is achieved through improvements in the processes that produce the product or service. Every activity and every job is part of a process - and can be improved. Improvement comes through people and learning. The strategy for process improvement used by teams in the ACRV Project Office, especially over the course of the summer, helps provide a roadmap for further improvement. The roadmap includes the development of team members who possess the ability to determine a common objective, define the relevant process, define the current knowledge, and build on that knowledge to make a change in the process using the improvement cycle. If the enthusiasm, and team activities, initiated in the projects described in this paper are used as a roadmap into the future, the ACRV Office will realize significant improvements in processes, and will leave a well-defined trail for others to follow along the road of continuous improvement.

ANALYSIS OF ISSUES FOR PROJECT SCHEDULING BY MULTIPLE, DISPERSED SCHEDULERS (DISTRIBUTED SCHEDULING) AND REQUIREMENTS FOR MANUAL PROTOCOLS AND COMPUTER-BASED SUPPORT

Final Report

NASA/ASEE Summer Faculty Fellowship Program--1991

Johnson Space Center

Prepared By:	Stephen F. Richards, Ph.D.
Academic Rank:	Associate Professor
University & Department	Ambassador College Computer Information Systems Department Big Sandy, Texas 75755
NASA/JSC	
Directorate:	Information Systems
Division:	Information Technologies
Branch:	Software Technology
JSC Colleague:	Chris Culbert
Date Submitted:	November 18, 1991
Contract Number:	NGT-44-001-800

ABSTRACT

Although computerized operations have significant gains realized in many areas, one area, scheduling, has enjoyed few benefits from automation. The traditional methods of industrial engineering and operations research have not proven robust enough to handle the complexities associated with the scheduling of realistic problems. To address this need, NASA has developed COMPASS (COMPuter Aided Scheduling System), a sophisticated, interactive scheduling tool that is in wide-spread use within NASA and the contractor community. Like most existing tools, however, COMPASS addresses only single- user applications. COMPASS therefore provides no explicit support for the large class of problems in which several people, perhaps at various locations, build separate schedules that share a common pool of resources.

This research examines the issue of distributed scheduling, as applied to application domains characterized by the partial ordering of tasks, limited resources, and time restrictions. The focus of this research is on identifying issues related to distributed scheduling, locating applicable problem domains within NASA, and suggesting areas for on-going research. The issues that this research identifies are goals, rescheduling requirements, database support, the need for communication and coordination among individual schedulers, the potential for expert system support for scheduling, and the possibility of integrating artificially intelligent schedulers into a network of human schedulers.

INTRODUCTION

Scheduling is the process of assigning resources and times to each activity of a plan (or plans) while ensuring that each constraint is obeyed. Optimization criteria can determine the relative desirability of two alternate schedules. Although scheduling problems are often simple to visualize and express, scheduling is an NP-complete problem, so attempts to apply mathematical programming to scheduling have met with very limited success [2, 6]. In fact, programming approaches have been limited to very narrow problem domains, especially that of the job-shop, in which jobs must be assigned to various machines.

This research focuses on the class of scheduling problem in which:

1) activities have precedence relationships (one activity must not begin until another activity has completed);
2) resources are limited;
3) objectives or optimization criteria exist that may be used to rank competing schedules; and
4) the time frame in which to complete all activities (or as many activities as possible) is limited.

This class of problem differs from the job-shop problem domain in that a job-shop problem assumes an infinite time line in which all activities may complete. In a job-shop problem, all activities are scheduled regardless of the total time required. In contrast, in this research resources may be over-subscribed, so that even the optimum schedule might not accommodate all desired activities within the time limitations. Thus, provision must be made for selecting between competing activities (or sets of related activities) where insufficient time exists for the completion of all activities.

To assist users in developing viable schedules NASA has developed COMPASS (COMPuter Aided Scheduling System) [3], a computer-based tool that interactively schedules activities in a user-specified order. COMPASS provides graphical tools for displaying activities, resource availability, and schedules. In COMPASS, activities are partially ordered and require resources. Activity attributes supported by COMPASS include priority, required resources, duration, earliest permissible start time, latest permissible end time, and state conditions. COMPASS has enjoyed wide-spread acceptance within NASA and the contractor community.

NASA has recently proposed enhancing COMPASS to support multi-user or distributed scheduling problems. This research has focused on the issues raised by distributed scheduling and on requirements for computerized support of this problem domain. The next section of this report defines distributed scheduling and addresses these issues.

DISTRIBUTED SCHEDULING

Distributed scheduling consists of those scheduling problems involving several schedulers, each of whom is responsible for scheduling activities that are somehow interrelated. Typically, the activities will share a common resource pool, but the activities also may have precedence requirements, or one activity may establish a state that another activity requires, etc. Distributed scheduling problem domains of particular interest to NASA include the scheduling of astronomical satellite experiments, personnel training, and space mission activities.

In such problems, the size and complexity of the scheduling task and the limited abilities, skills, knowledge, and resources of any individual make the distribution of the

scheduling task a natural and necessary means of developing the required schedule. By distributing the work, each scheduler can concentrate on a manageable volume of work in a narrow domain. However, the lack of a single point of control increases the complexity of the overall scheduling problem (as a result of the necessary communication overhead) and raises several issues regarding the interactions of multiple schedulers and the integration of their individual schedules.

The most basic issue is that of goals. What measure of goodness is most appropriate in a distributed environment? How do the optimization criteria for a distributed scheduling problem differ from those for a non-distributed problem? Variables commonly used for scheduling problems include [4, 5]:

-- Completion time: the time at which processing of the last activity completes.
-- Flow-time: the total time that activities spend in the shop.
-- Lateness: the difference between the completion time of an activity and some pre-specified due date associated with that activity.
-- Tardiness: equal to lateness when lateness is positive, otherwise equal to zero.

Schedule evaluation criteria typically involve minimizing or maximizing the mean, total, minimum, or maximum or one or more of these variables. In a standard job-shop problem, these criteria are assumed to be universally agreed upon. However, even in such a standard, non-distributed scheduling environment, the various tasks to be scheduled may belong to several different customers (perhaps represented by members of the marketing staff), each of whom would prefer that his or her tasks be given high priority. Thus, even in a non-distributed setting conflicting goals may exist. When conflict exists, the scheduler must have some means of determining a set of priorities to be applied to the scheduling task. The scheduler may be flexible in his or her choice of priorities, adjusting them to the needs of the moment. For example, the scheduler might attempt to mollify a major customer who has been slighted by giving preference to that customer's work. Regardless of the conflicting demands, however, the optimization requirements are formulated as a single point of control and this procedure can succeed because the single scheduler (or team of schedulers) who develops the optimization criteria also controls the entire resource pool.

In a distributed schedule, however, individual schedulers must share resources, so one scheduler optimizing his or her schedule may restrict another scheduler's options, resulting in a suboptimal global schedule. The issue of a global measure of goodness becomes more important in distributed scheduling than in individual, interactive scheduling. This is true because an individual scheduler can accept a schedule even without a specific measure of goodness; the schedule may balance several conflicting needs fairly well and "just look good." A distributed schedule, in contrast, must "look good" through several sets of eyes. When a team of schedulers must continue to work together on future projects, perceptions of inequity or misplaced priorities can engender resentments that will poison these on-going relationships. Thus, some mechanism for balancing both local and global optimization must be provided. The protocol used by the schedulers to coordinate their activities must support optimization techniques that are perceived as both equitable and efficient.

Selecting a desirable scheduling protocol requires balancing several possibly conflicting goals, including the following [1]:

1. The protocol should encourage the development of high quality schedules that score well when evaluated by either the global optimization criteria or the optimization criteria of individual schedulers. Schedules should also be resilient to unexpected changes.
2. The protocol should be easy to use. Features enhancing ease of use include ease of

learning; minimum complexity; informative to the user of the state of activities, resources, etc.; and natural representation or concepts. Yet, the process should be sufficiently rich in features and notation to encompass a wide range of scheduling problems.

3. The overhead, such as communications requirements, should be kept to a minimum.
4. The time required to develop schedules should be short, especially in highly dynamic environments.
5. Any computerized support should have a short response time. This requires that optimization techniques be computationally simple.

Several sample scheduling protocols are listed below. For each alternative the issues of division of resources, communication, cooperation, and optimality are discussed.

1. Schedule tasks by priority. This protocol requires that all tasks be known and prioritized in advance and then be scheduled in priority sequence. This is really non-distributed scheduling, except that we have several schedulers responsible for collecting tasks and we may provide improved computer support to enable the individual schedulers to track their own set of tasks by viewing only their portion of the schedule. This protocol also requires some mechanism for assigning priorities to tasks (e.g., a central authority or a voting scheme). The potential for high quality projects is the same as for non-distributed scheduling. Although an advantage of this method is that participants will perceive it as fair, following this method strictly does not allow for compromises, such as scheduling two medium priority, low resource intensive tasks instead of one high priority, high resource intensive task.
2. First come, first served. In this approach all schedulers are equal and none has priority over the others. Resources are not assigned to individual schedulers, but may be reserved by any scheduler. The state of the global schedule must be continuously available to all schedulers. No cooperation among schedulers is required. Optimization is poor, because there is no attempt to balance the needs of multiple schedulers. There is a tendency among schedulers to reserve resources early, even before they know their full requirements. This tendency to hoard can result in the allocation of resources to low priority tasks.
3. Divide resources among schedulers in advance. This protocol permanently allocates resources to specific schedulers who can use them as they choose. No communication or cooperation among schedulers is required. Schedulers need not even know the global schedule. This approach is impractical when there is a potential state conflict between tasks (e.g., when two schedulers independently schedule a treadmill experiment and aa microgravity experiment that requires no vibration). This approach may also yield poor schedules when one scheduler assigns resources to low priority tasks or leaves resources unused that could be used by another scheduler. In this approach the quality of the resulting schedule is limited by the quality of the initial allocation of resources.
4. Divide resources among schedulers in advance but permit borrowing. This approach differs from the previous one by permitting schedulers to negotiate among themselves to improve their schedules. There is still no need for global optimization criteria. The status and bargaining power of individual schedulers is determined by the initial allocation of resources. Communication needs consist of a knowledge of resources available to other users.
5. Sharing of intentions among schedulers. In this protocol schedulers review their intentions with their peers and receive feedback before reserving resources and

committing to a particular schedule. While this approach has the potential for producing high quality schedules through the sharing of knowledge and expertise, it also imposes a heavy communication burden among schedulers that can negate much of the benefit resulting from distributing the scheduling task. This approach is also fragile in that its success depends on the voluntary cooperation of each scheduler. Where this cooperation fails, this protocol can degenerate into a first come, first served system.

6. Simultaneous iterative scheduling. In this protocol each scheduler devises a schedule and shares it with others. Schedulers identify and resolve conflicts by some agreed upon method. If unscheduled tasks and unallocated resources remain, another round of scheduling follows. In this approach all schedulers must be ready to schedule simultaneously. Also, each participant must be provided some incentive to cooperate with the others in resolving conflicts. The global schedule must be available to all schedulers.
7. Consecutive iterative scheduling. In this protocol the schedulers are divided into two or more groups that alternately devise schedules. This approach is useful when one group creates resources required by another. For example, a university administration develops a schedule of classes, the students then submit their individual schedule requests, and the administration, after analyzing the requests, adds sections to some classes and deletes sections from others. The students then request changes to their schedules. In principle this cycle can continue for many iterations. This approach requires some incentive to cooperate and requires that each scheduler knows the global schedule and the state of available resources.

Any attempt to develop a universal scheduling methodology is doomed to failure because of the enormous diversity of scheduling domains. The variety of tasks, resources, constraints, and environments is virtually unlimited. The protocols listed above are not applicable to all domains but must be selected based on the characteristics of the specific domain of interest.

A second issue identified by this research is the requirement for revising a schedule, also termed rescheduling [2]. Several factors can trigger a need to reschedule. A resource can become unavailable, making the current schedule unfeasible; a task can take longer than expected; or a user can change his or her requirements so as to impose a conflict, exhaust a resource needed by a later task, or delete an enabling task that creates a resource or state needed subsequently. In addition, rescheduling is desirable, although not required, whenever an opportunity arises to improve the schedule by adding previously unscheduled tasks or resequencing already scheduled tasks. This can happen, for example, when new resources become available or when a task completes early. Differences between scheduling and rescheduling include: 1) rescheduling takes place in the context of an existing schedule that we may wish to disturb as little as possible; 2) rescheduling must consider work in progress; 3) rescheduling often must occur quickly, in contrast to the initial scheduling which may be performed in a more leisurely manner; and 4) someone other than the original scheduler may perform the rescheduling. An important issue for rescheduling in a distributed scheduling environment is the need to reduce communication requirements among schedulers to facilitate quick rescheduling. Since this may require a return to centralized scheduling, the rescheduler must have the appropriate information to make beneficial changes.

A third issue is that of database support for distributed scheduling. A distributed scheduling system requires many of the features of a distributed database management system. The system must merge separate databases of tasks, resources, constraints, and

assignments into a single image while retaining the ability to display for individual schedulers only those portions of the database under their control. However, since each scheduler has a different view of the world (with different time scales, measures of goodness, types of constraints, etc.), the system must support different user languages and communicate with each scheduler in a natural and helpful way. As our software tools, such as COMPASS, address more diverse and complex problem domains, we will require a more comprehensive database language for describing scheduling problems.

A fourth issue is that of communication and coordination among schedulers. At present, many of the NASA schedulers who impact one another by their work do not even know one another, much less communicate regularly. The people who schedule the Hubble telescope and its ground facilities are assigned specific resources that they schedule independently of each other. One research question concerns how much of this lack of communication is the result of historical developments and how much is intentional on the part of schedulers. Do they fail to communicate because they do not perceive a need to communicate, or because they feel communication is too time consuming, or because they fear loss of control of their environment, or is there some other reason? If independent scheduling is a human preferred approach, then it will be important to determine why this is true, how we can encourage people to cooperate, and how we can enhance cooperation while reducing communication. The mechanisms for communication and coordination (the languages, database support, and interaction procedures) appear to be a critical aspect of distributed scheduling by human agents.

A fifth issue involves the introduction of expert system support for scheduling. Optimization heuristics have been envisioned for individual scheduling support; some of this support is already available on COMPASS. Support for distributed scheduling would focus on communication and negotiation. An expert system that monitored the actions of all schedulers could infer when one scheduler needed to know of the actions of another. This would reduce communications requirements. Also, an expert system could search for instances in which it would be mutually advantageous for two schedulers to trade resources or to reschedule certain tasks.

Finally, a sixth issue asks how we can introduce artificially intelligent schedulers into the system. The scheduling of certain domains, such as power generation, may be suitable for AI approaches. It would be natural to introduce such agents into human scheduling systems. How can artificial and human agents best interact? This issue awaits the development of suitable AI schedulers for individual scheduling domains.

CONCLUSIONS

This research has begun an investigation of the issues of distributed scheduling. This report has identified and discussed several issues. These issues will impact both the computerized support for distributed scheduling that is envisioned to appear in future versions of COMPASS as well as the manual procedures that schedulers will use for cooperating with one another.

During this academic year this researcher will remain in contact with NASA to identify members of the NASA community who might benefit from distributed scheduling and who are willing to participate in experiments during the coming summer. During the summer we will investigate the effects of different optimization criteria and procedures for communication and coordination.

REFERENCES

1. Fox, Mark S., "Constraint-Directed Search: A Case Study of Job Shop Scheduling," Ph.D. dissertation, Carnegie-Mellon University, 1983.

2. Fox, Mark S. and Zweben, Monte, "Knowledge Based Scheduling," Tutorial MA2, presented at the Ninth National Conference on Artificial Intelligence, July 15, 1991.

3. McDonnell Douglas Space Systems Co., "COMPASS 2.0 User's Manual", for NASA/Johnson Space Center Software Technology Branch, 1991.

4.. Ow, Peng Si, "Heuristic Knowledge and Search for Scheduling," Ph.D. dissertation, Carnegie-Mellon University, 1984.

5. Salvador, Michael S., "Scheduling and Sequencing," in HANDBOOK OF OPERATIONS RESEARCH, Joseph J. Moder and Salah E. Elmaghraby (Editors), Van Nostrand Reinhold, New York, 1978, pp. 268-300.

6. Ullman, J. D. "NP-Complete Scheduling Problems," Journal of Computer and System Sciences, Vol. 10, 1975, pp. 384-393.

NONDESTRUCTIVE STRUCTURAL DAMAGE DETECTION IN FLEXIBLE SPACE STRUCTURES USING VIBRATION CHARACTERIZATION

Final Report

NASA/ASEE Summer Faculty Fellowship Program - 1991

Johnson Space Center

Prepared By:	James M. Ricles, Ph.D.
Academic Rank:	Assistant Professor
University & Department:	University of California, San Diego Department of AMES, 0411 La Jolla, California 92093
NASA/JSC	
Directorate:	Engineering
Division:	Structures and Mechanics
Branch:	Loads and Structural Dynamics
JSC Colleague:	David A. Hamilton
Date Submitted:	August 16, 1991
Contract Number:	NGT-44-001-800

ABSTRACT

Spacecraft are susceptible to structural damage over their operating life from impact, environmental loads, and fatigue. Structural damage that is not detected and not corrected may potentially cause more damage and eventually catastrophic structural failure. NASA's current fleet of reusable spacecraft, namely the Space Shuttle, has been flown on several missions. In addition, configurations of future NASA space structures, e.g. Space Station Freedom, are larger and more complex than current structures, making them more susceptible to damage as well as being more difficult to inspect. Consequently, a reliable structural damage detection capability is essential to maintain the flight safety of these structures. Visual inspections alone can not locate impending material failure (fatigue cracks, yielding), it can only observe post-failure situations. An alternative approach is to develop an inspection and monitoring system based on vibration characterization that assesses the integrity of structural and mechanical components.

A methodology for detecting structural damage is presented. This methodology is based on utilizing modal test data in conjunction with a correlated analytical model of the structure to: (1) identify the structural dynamic characteristics (resonant frequencies and mode shapes) from measurements of ambient motions and/or force excitation, (2) calculate modal residual force vectors to identify the location of structural damage, and (3) conduct a weighted sensitivity analysis in order to assess the extent of mass and stiffness variations, where structural damage is characterized by stiffness reductions. The approach is unique from other existing approaches in that varying system mass and stiffness, mass center locations, the perturbation of both the natural frequencies and mode shapes, and statistical confidence factors for structural parameters and experimental instrumentation are all directly accounted for.

An analytical assessment was conducted on the methodology. The results of this assessment show the method to provide a precise indication of both the location and the extent of structural damage.

INTRODUCTION

Flexible space structures, launch vehicles, and satellites are susceptible to structural damage over their operating lifes from impact, operating loads, and fatigue. Undetected and uncorrected damage can lead to structural deterioration of their members and consequently jeopardize the flight safety of the structure. Thus, numerous damage inspection methods and monitoring procedures have been developed and used by NASA and the aerospace industry. These include: X-ray; ultrasonic testing; magnetic resonance; coin tap; dye penetrate; and visual inspection. These methods can be time consuming and are local assessments, often requiring the exposure of structural elements to the inspector and equipment for detecting damage. As a monitoring system for detecting spacecraft in orbit (i.e. Space Station Freedom) none of these are appropriate. An alternative approach, which formed the basis for the study reported herein, is to recognize the fact that modal vibration test data (structural natural frequencies and mode shapes) characterizes the state of the structure [Ewins, 1984]. Therefore, postflight and inflight (e.g. monitoring) data can be utilized to distinguish whether changes (damage) have occurred to the structure by comparing this data to a set of baseline data. Modal testing as a means of inspection has several advantages. Direct exposure of structural elements is not required, while at the same time more of the complete structure can be inspected in one modal test by having appropriately placed sensors. The consequences of this is a reduction in schedule and cost.

In the past, the purpose of performing modal testing on a structure has been to correlate and calibrate the structure's analytical model in order that the mode shapes and frequencies of the model and test results agree over selected frequency ranges. Correcting analytical models in this manner is often referred to as system identification (SID). A vast amount of work has been done in the area of SID and procedures have evolved for application in the industry. In order to use SID in damage detection, the formulation must be based on maintaining element connectivity. Some of the SID methods which qualify and have been extended to damage detection are those of Kabe [1985] and Chen and Garba [1988]. Both of these however are based on the severe limitation that the mass is constant and changes in vibration characteristics are associated with only stiffness loss or gain. Some of the more recent development in damage detection by vibration characterization is that of Stubbs [1990], which accounts for the possibility of change of mass and/or stiffness. The development however ignores the sensitivity to mode shape perturbation. All of the above noted methods do not consider uncertainty in instrumentation.

This study was concerned with developing a new methodology for nondestructive damage detection in flexible space structures, in which the phenomena ignored in current methods are accounted for. The methodology was formulated on the basis of using modal test data to characterize the state of the structure, considering: varying system mass and stiffness; mass center locations; perturbation in vibration frequencies and mode shapes; statistical weighting factors for analytical model structural parameters (e.g. element mass and stiffness); and confidence factors for errors in experimental instrumentation. The scope of this study included implementing the damage detection methodology onto a computer in order to validate and assess the approach. This validation and assessment effort is based on analytically derived modal test data for a number of different cases, representing damage scenarios involving two structures. The theoretical basis of the methodology and summary of its assessment is included in this report. Conclusions based on the assessment and topics for future research are noted.

THEORETICAL BASIS

General

The algorithm for damage detection is given in Fig. 1, and consisting of three main parts: 1) Modal Test Survey; 2) Locating Damage; and 3) Assessing the Severity of Damage. In the modal test survey a baseline experimental modal test is performed to measure the vibration properties Λ_0, which includes natural frequencies ω_0 and mode shapes Φ_0. This data is used to

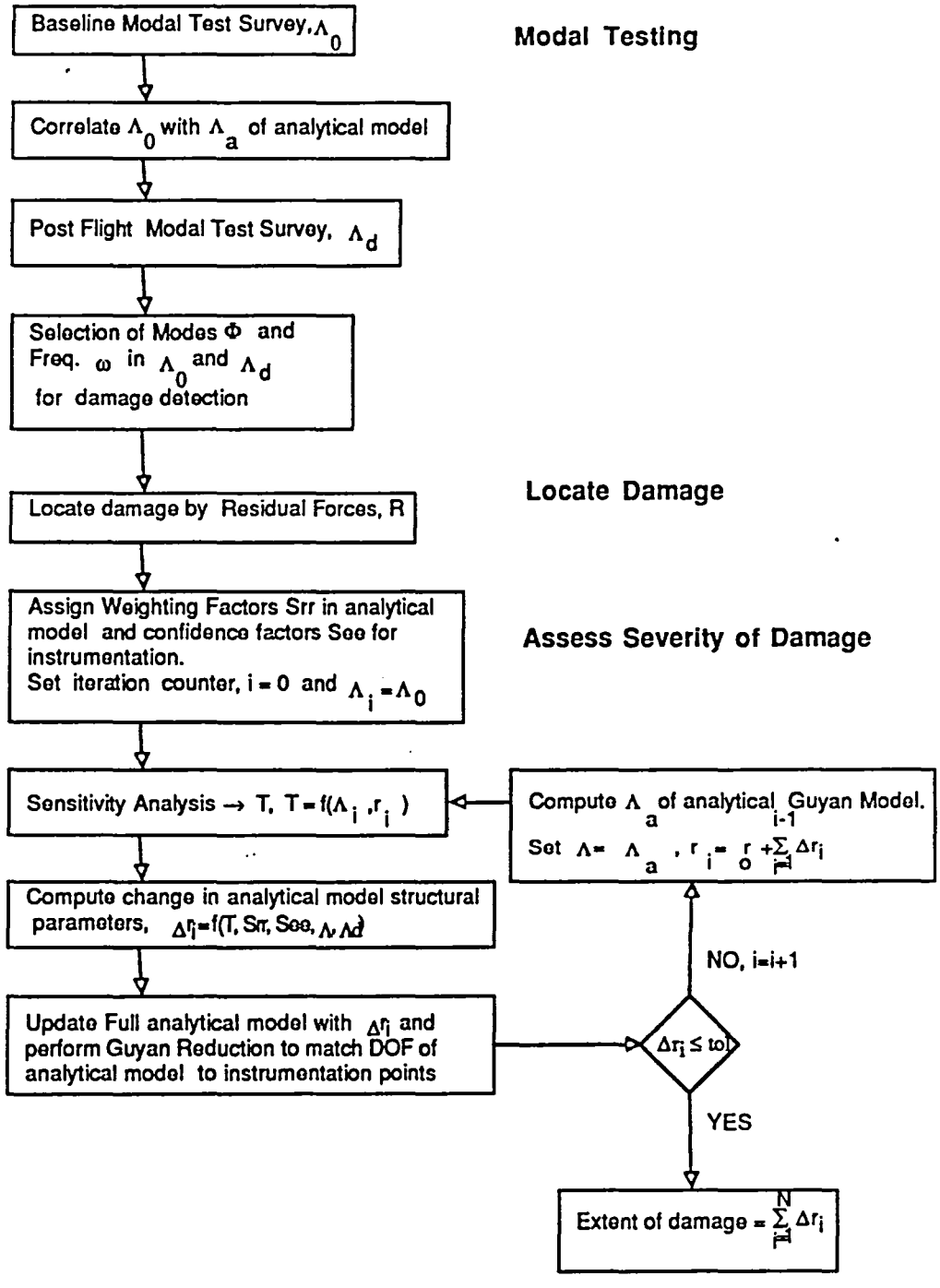

Figure 1. - Damage Detection Algorithm

correlate with an analytical model and set the baseline for subsequent comparison in the remaining parts of the algorithm. The modal test survey is completed by conducting postflight, or inflight for monitoring, experimental modal testing to measure the vibration properties Λ_d , which includes natural frequencies ω_d and mode shapes Φ_d.

It is necessary to select appropriate frequencies and mode shapes in Λ_o and Λ_d to start the damage detection. This is accomplished by considering the correlation of Λ_o with the vibration properties Λ_a of the analytical model. The selection of modes must be done such that discrepancies between Λo and Λa are smaller than those of Λ_o and Λ_d, otherwise one will be incorrectly estimating the damage due to the fact that the analytical model is corrected to match Λ_o and further undergoes changes towards Λ_d . The selection of modes should be based on the following criteria: a smaller frequency shift $\Delta\omega$ as well as a superior set of values for modal assurance criterion (MAC) between Λ_o and Λ_a compared to Λ_o and Λ_d , and an adequate cross orthogonality check (COR) between Λ_o and Λ_a ; where for mode i (considering Λ_o and Λ_a)

$$\Delta\omega_i = (\omega_i)_0 - (\omega_i)_a \qquad [1]$$

$$MAC_i = \frac{\left[\sum_{j=1}^{N} (\phi_{ji})_0 (\phi_{ji})_a\right]^2}{\sum_{j=1}^{N} (\phi_{ji})_0^2 \sum_{j=1}^{N} (\phi_{ji})_a^2} \qquad [2]$$

and for all modes , $$COR = \Phi_0^T M_a \Phi_a \qquad [3]$$

in which M_a = analytical mass matrix, and j = instrumentation point location. In Eqns [1], [2], and [3] the assessment for Λ_o - Λ_d is performed by replacing Λ_a with Λ_d.

Locating Damage

Identifying the location of damage in the structure is based on differences in Λ_d and Λ_0 through an extended application of the Residual Force Method [Chen and Wang, 1988]. In concept, the experimental frequencies and mode shapes must satisfy an eigenvalue equation, where considering the damaged structure and mode i

$$(K_d - \lambda_{di} M_d)\phi_{di} = 0 \qquad [4]$$

in which K_d and M_d are the experimental (unknown) stiffness and mass matrices associated with the damaged structure, respectively, and λ_{di} (ω_{di}^2) the experimental measured eigenvalue (natural frequency squared) corresponding to the experimental measured mode shape ϕ_{di} of mode i of the damaged structure. Assuming that the damaged stiffness and mass matrices are defined as

$$K_d = K_b + \Delta K \qquad [5]$$

$$M_d = M_b + \Delta M \qquad [6]$$

in which K_b , M_b = known baseline stiffness and mass matrices of the analytical model, and ΔK, ΔM = unknown changes in stiffness and mass matrices due to damage. Substituting Eqns. [5] and [6] into Eqn. [4] and rearranging, one arrives at the definition of the residual force vector R_i for mode i

$$R_i = -\left(\Delta K - \lambda_{d_i}\Delta M\right)\phi_{d_i} \qquad [7a]$$

$$= \left(K_b - \lambda_{d_i}M_b\right)\phi_{d_i} \qquad [7b]$$

where the right hand side of Eqn. [7b] is known and will be equal to zero for an undamaged structure. By examining R_i, where each term corresponds to a measurement point on the structure, one can locate regions in the structure that are damaged. These locations correspond to the degrees-of-freedom (DOF) that have large magnitudes in R_i. It should be emphasized that one should calculate R_i for several modes, for if a damaged member is near a node line where the modal displacement is near zero, the residual forces will have a tendency to be near zero.

Assessment of Damage Severity

The assessment of damage severity is based on establishing a relationship between the measured vibration characteristics and structural parameters (members mass, stiffness, section geometry) in the damaged region using a first order Taylor series expansion:

$$\Lambda_d = \Lambda_0 + T(r_d - r_0) + \varepsilon \qquad [8]$$

where Λ_d , Λ_0 = arrays containing corresponding selected measured natural frequencies and modes shapes in which $\Lambda^T=\{\omega^2,\Phi\}^T$; r_d, r_0 = unknown array of structural parameters in damaged region and known baseline array of structural parameters in same location of structure, ε = array of testing errors associated with each measured parameter (e.g. mode shape amplitudes and natural frequencies). Matrix T is a sensitivity matrix that relates the change in vibration parameters, accounting for the perturbation in natural frequencies and mode shapes:

$$T = \begin{bmatrix} \frac{\partial\omega^2}{\partial K} & \frac{\partial\omega^2}{\partial M} \\ \frac{\partial\Phi}{\partial K} & \frac{\partial\Phi}{\partial M} \end{bmatrix}_0 \begin{bmatrix} \frac{\partial K}{\partial r} \\ \frac{\partial M}{\partial r} \end{bmatrix}_0 \qquad [9]$$

The subscript "o" is associated with the baseline configuration. The four individual submatrices in the first matrix of T represents partial derivatives of the eigenvalues and mode shapes with respect to the coefficients of the stiffness and mass matrices, whereas the second matrix of T represents the partial derivatives of the stiffness and mass matrices with respect to the structural parameters r. The derivatives of the eigenvalues and mode shapes are determined from the measured baseline data Λ_0 and analytical mass matrix, where for mode k and considering instrumentation points i and j it can be shown:

$$\frac{\partial\omega_k^2}{\partial K_{ij}} = \frac{\phi_{ik}\phi_{jk}}{\phi_k^T M\phi_k}; \qquad \frac{\partial\phi_{rk}}{\partial K_{ij}} = \sum_{n=1}^{q}\left[\frac{\phi_{in}\phi_{jk}\phi_{rn}}{(\omega_k^2 - \omega_n^2)\phi_n^T M\phi_n}\right](1 - \delta_{nk}) \qquad [10]$$

$$\frac{\partial \omega_k^2}{\partial M_{ij}} = \frac{-\omega_k^2 \phi_{ik}\phi_{jk}}{\phi_k^T M \phi_k} \quad ; \quad \frac{\partial \phi_{rk}}{\partial M_{ij}} = \sum_{n=1}^{q} \left[\frac{-\omega_k^2 \phi_{in}\phi_{jk}\phi_{rn}(1 - \delta_{nk})}{(\omega_k^2 - \omega_n^2)\phi_n^T M \phi_n} - \frac{\phi_{in}\phi_{jk}\phi_{rn}\,\delta_{nk}}{2\,\phi_n^T M \phi_n} \right] \qquad [11]$$

in which q = number of retained modes in Λ_0 for the assessment, n = index to identify mode number.

The goal in the assessment is to determine r_d. This is accomplished by first treating the difference $R = r_d - r_0$ for all structural parameters as normally distributed random variables with a zero mean and a specified covariance S_{RR} in order to deal with the uncertainty in the damage assessment. Treating the test measurement error also as a random variable with a zero mean and specified covariance $S_{\varepsilon\varepsilon}$ leads to the solution, where it can be shown that

$$r_d = r_o + S_{RR}^* T^T [T S_{RR}^* T^T + S_{\varepsilon\varepsilon}]^{-1} (\Lambda_d - \Lambda_0) \qquad [12]$$

where

$$S_{RR}^* = S_{RR} - S_{RR} T^T [T S_{RR} T^T + S_{\varepsilon\varepsilon}]^{-1} T S_{RR} \qquad [13]$$

Values for the diagonal terms (e.g. variances) in S_{RR} are assigned in conjunction with the results of the residual force analysis, all off diagonal terms being set equal to zero. Only those members suspected of damage are given nonzero variances, and therefore are the only members that are emphasized in the damage severity assessment. In this study all suspected members with damage were given equal variances. It should be noted that uncertainties in the analytical model can also be considered by assigning nonzero variances related to the structural parameters associated with these uncertainties.

If the relationship between the stiffness and mass components and the structural system is linear the method will converge in one step. However, the partial derivatives of the eigenvalues with respect to the stiffness and mass coefficients is nonlinear if enough damage has occurred to cause a frequency shift, as illustrated in Fig 2(a). To obtain a more accurate assessment of the severity of damage it is necessary to either continuously monitor the system (inflight damage monitoring) or use the correlated analytical model to update the damage assessment in order to converge to Λ_d, as illustrated in Fig. 2(b). Each update involves completing the tasks associated with the part of the algorithm labelled Damage Severity Assessment in Fig. 1. The change in the structural parameters at the i^{th} updating point is $\Delta r_i = r_d - r_i$, where r_d comes from Eqn. [12] considering $r_0 = r_i$ with $T = T_i$ and $\Lambda_0 = \Lambda_i$. Here r_i = the current value for the structural parameters, which reflects the accumulated changes from previous updates and T_i = the sensitivity matrix based on the vibration characteristics of the updated baseline analytical model (or in the case of an online monitoring system, the measured characteristics at the point). Convergence is achieved when Δr_i during an update becomes less than the tolerance for convergence, with the predicted extent of damage equal to the sum of Δr_i for all of the update cycles, as indicated in Fig 2(b).

As noted in the damage detection algorithm (Fig. 1) the full analytical model is updated, which may likely have more degrees-of-freedom (DOFs) than instrumented DOFs of the modal test structure. Guyan reduction is therefore required to reduce the model's DOFs to the instrumentation points. The other alternative is to maintain the full model in the assessment and not evaluate the columns in T pertaining to non-instrumented DOFs. The first procedure was pursued. In evaluating the sensitivity matrix, the derivatives of the stiffness and mass coefficients involves the Guyan transformation matrix Ψ:

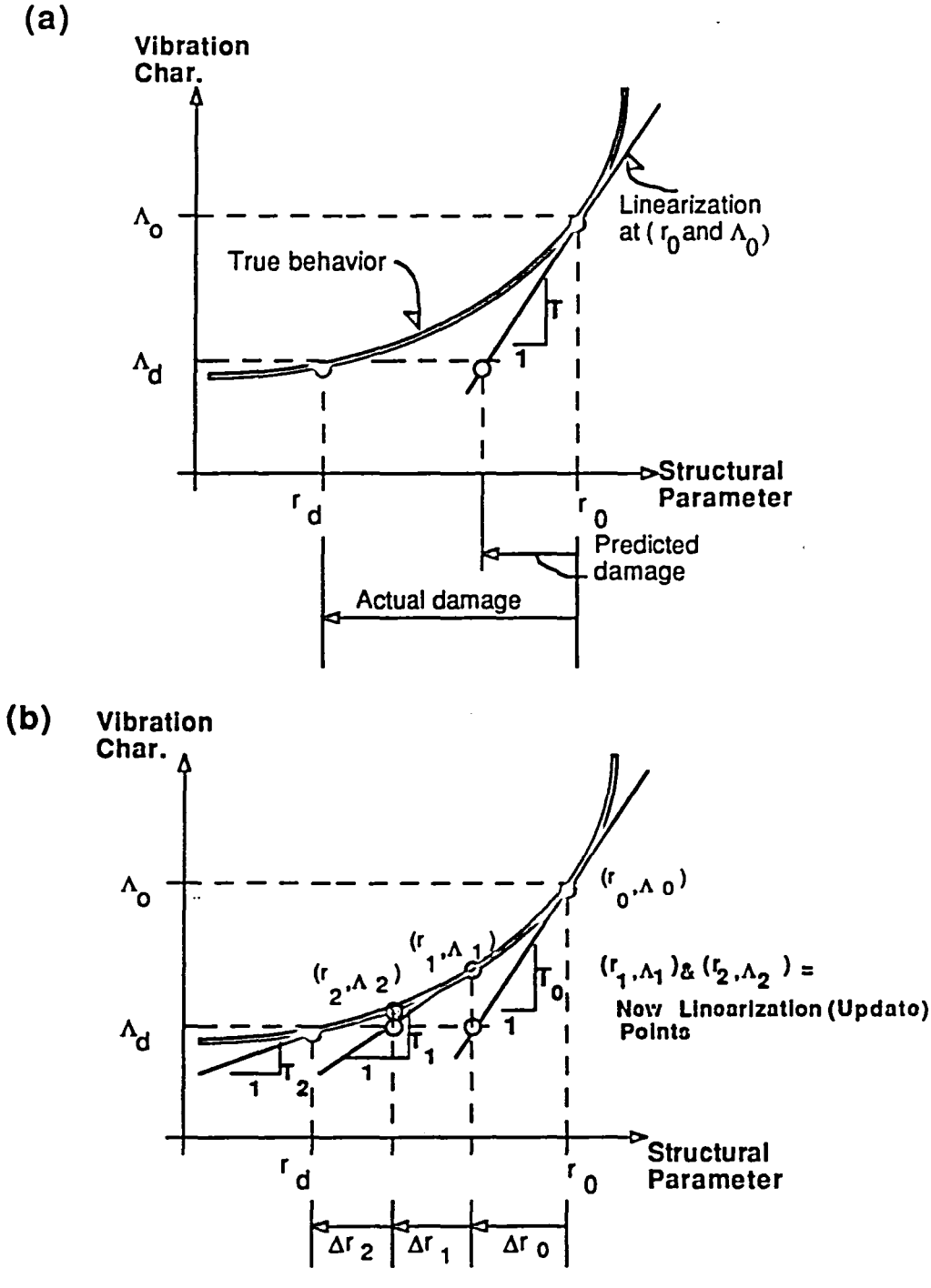

Figure 2. - (a) Linearization of the Nonlinear Relationship and, (b) Updating to Obtain Convergence.

$$\frac{\partial K_{ij}}{\partial r} = \frac{\partial}{\partial r}\left(\Psi^T K^* \Psi\right) = \frac{\partial \Psi^T}{\partial r} K^* \Psi + \Psi^T \frac{\partial K^*_{ij}}{\partial r} \Psi + \Psi^T K^* \frac{\partial \Psi}{\partial r} \qquad [14]$$

$$\frac{\partial M_{ij}}{\partial r} = \frac{\partial}{\partial r}\left(\Psi^T M^* \Psi\right) = \frac{\partial \Psi^T}{\partial r} M^* \Psi + \Psi^T \frac{\partial M^*_{ij}}{\partial r} \Psi + \Psi^T M^* \frac{\partial \Psi}{\partial r} \qquad [15]$$

where K^* and M^* = stiffness and mass matrices related to the full analytical model.

VALIDATION AND ASSESSMENT

Program of Investigation

The verification and assessment of the damage detection methodology involved an 'analytical modal test structure', and therefore is analytical in nature. An experimental assessment is planned as a future study. The analytical assessment involved imposing damage to the modal test structure and 'forgetting' where these locations existed and the extent of imposed damage. An attempt was then made to detect the damage, using Λ_0 based on the undamaged 'analytical modal test modal' and Λ_d based on the damaged 'analytical modal test model'.

Two structures were considered in this study: Structure A and Structure B. Both of these structures are shown in Fig. 3. Structure A consists of a 40 member truss structure with 32 in plane translational DOF. All DOF are located at the nodes shown in Fig. 3, having lumped mass of m. At two nodes a greater mass of M was assigned. Each of these additional mass represented 36% of the total structural mass and were placed to represent similar situations that exists in space truss type structures. All 32 DOF were assumed to be instrumented, hence the ensuing analytical model (which was a finite element model- FEM) used in the algorithm shown in Fig. 1 represented a perfectly correlated model where $\Lambda_0 = \Lambda_a$. Structure B had similar geometry as Structure A, except that the mass was more distributed and in plane rotational and translational DOF existed, which resulted in a 168 DOF structure with 80 elements. The nodes, each having a lumped mass, and elements is shown in Fig. 3(b). Only 32 translational DOF of Structure B were instrumented, and identified in Fig. 3(c). The FEM used to assess the damage was a Guyan reduced FEM, where the full FEM had the 168 DOF of the modal test model. Thus, Λ_a was based on a 32 DOF Guyan reduced FEM, with Λ_0 and Λ_d obtained from the 168 DOF modal test model (modal displacements being only 'known' at the 32 instrumented translational DOF).

A total of five cases were studied, each representing a different damage scenario. These cases are described in Table 1, and refer to damaged members shown in Fig. 3. In all cases $S_{\varepsilon\varepsilon}$ was based on standard deviations equal to 2% of the modal frequencies and maximum modal displacements of each mode retained in the assessment. Members suspected of damage were weighted equally, S_{RR} based on standard deviations of 15% of the baseline material's Young modulus.

Structure A

The natural frequency of vibration for the first six modes of Structure A are given in Table 2. The baseline frequencies, f_0, are identical to the FEM frequencies f_a since both were produced from the same analytical model. Thus no MAC or orthogonality checks were required. The damaged frequencies f_d pertaining to the postflight modal test for all cases and the shift from the baseline frequency f_0 are also given in Table 2. The amount of frequency shift is considered small. For mode 2 of Case 1 and mode 1 of Case 2 there is no frequency shift due to damage. In Case 2 the damaged structural frequencies become larger due to the combined effect of decrease in stiffness and decrease in mass (5% of M). As more members are damaged without loss of mass (Cases 3 and 4) there is a greater frequency shift, for the f_d for these cases becomes smaller.

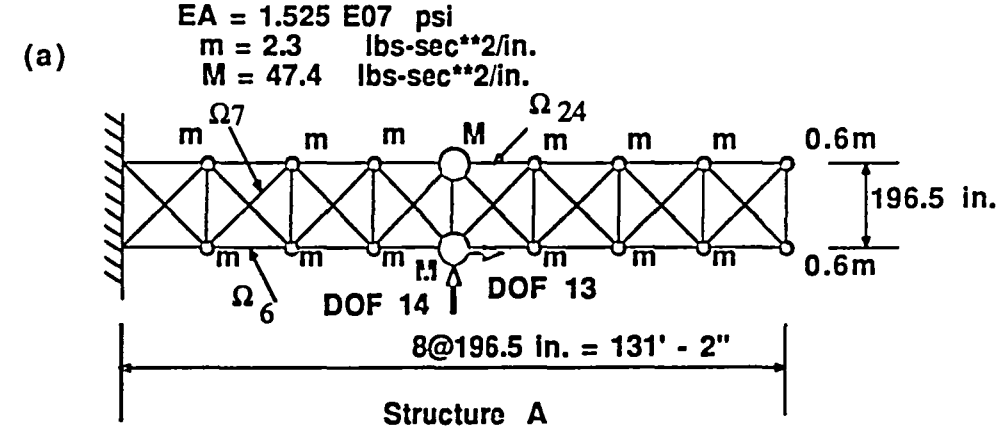

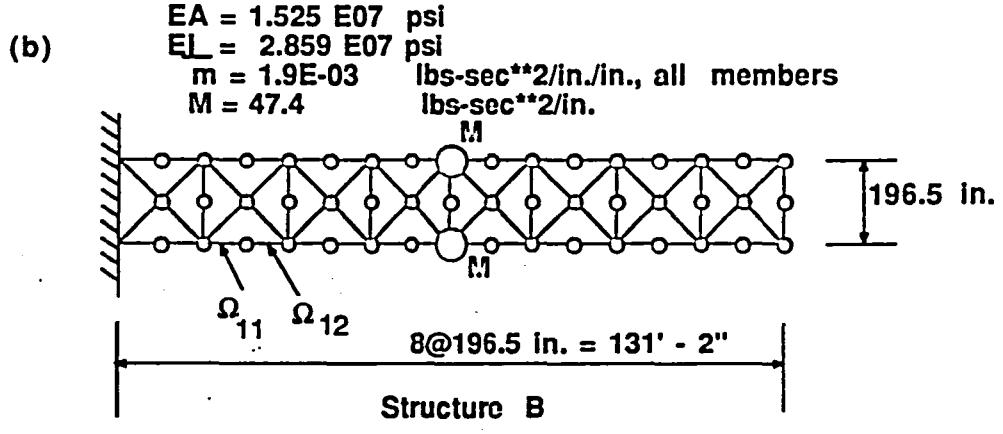

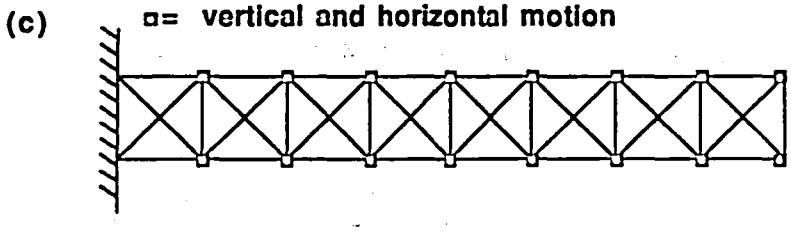

Figure 3. - (a) Modal Test Structure A, (b) Structure B, and (c) Instrumentation Points.

TABLE 1. - Case Studies for Assessment

Case	Structure	Comments
1	A	10% stiffness loss in member (Ω_6)
2	A	10% stiffness loss in member, (Ω_6), 5% loss of mass at DOF 13 &14
3	A	two members with stiffness loss, $(\Omega_6 = 10\%; \Omega_7 = 5\%)$
4	A	3 members with stiffness loss, $(\Omega_6 = 10\%; \Omega_7 = 5\%; \Omega_{24} = 5\%)$
5	B	10% stiffness loss in one member, (Ω_{11})

TABLE 2. - Case Studies for Assessment, Structure A

Mode	Natural Frequency - Hz.									
	f_0	f_a	Case 1		Case 2		Case 3		Case 4	
			f_d	$f_0 - f_d$	f_d	$f_0 - f_d$	f_d	$f_0 - f_d$	f_d	$f_0 - f_d$
1	0.499	0.499	0.496	0.003	0.499	0.0	0.496	0.003	0.496	0.003
2	2.212	2.212	2.212	0.000	2.222	-0.010	2.211	0.001	2.204	0.008
3	3.144	3.144	3.126	0.018	3.157	-0.013	3.125	0.019	3.125	0.019
4	7.109	7.109	7.105	0.004	7.157	-0.048	7.101	0.008	7.078	0.031
5	9.815	9.815	9.814	0.001	9.932	-0.117	9.814	0.001	9.808	0.007
6	11.646	11.646	11.638	0.008	11.649	-0.003	11.635	0.011	11.630	0.016

TABLE 3. - Natural Frequencies and Modal Assurance Criteria, Structure B

Mode	Natural Frequency - Hz.					MAC	
	f_0	f_a	f_d	$f_0 - f_a$	$f_0 - f_d$	$\phi_0; \phi_a$	$\phi_0; \phi_d$
1	0.554	0.555	0.552	-0.001	0.002	0.999	0.999
2	2.704	2.706	2.704	-0.002	0.000	0.999	0.999
3	3.313	3.315	3.304	-0.002	0.009	0.999	0.998
4	7.827	7.921	7.826	-0.094	0.001	0.997	0.996

The residual forces for mode 1 are shown in Fig. 4 for all cases. The forces were calculated using Eqn. [7b], where K_b and M_b are that of the FEM. The residual forces acting at the nodes for which no value is given in Fig. 4 were 3 to 4 orders of magnitude smaller than those shown. The residual forces for Case 1 give a clear indication than member 6 is damaged, for the forces are equal and opposite and act at the ends of member 6. For Case 2 the residual forces again give an indication that member 6 is damaged, and that there exists some change at DOF 13 and 14 which is associated with the location of the loss of mass. The residual forces for Case 3 indicate damage in members 6 and 7, by recognizing the way in which the forces balance. Likewise, the residual forces for Case 4 give an indication that members 6, 7,and 24 are damaged. The forces for mode 1 appear to also correctly indicate the relative extent of damage among the members. This is generally not true, for damaged members near a node line will have a small residual force due to the small modal displacements at these locations.

The results of the assessment of damage severity are shown in Fig. 5, where the predicted damage in terms of percent of baseline value is plotted as a function of number of updates. All results show convergence to the exact result and give a precise indication of the severity of member damage. The affect of retaining a larger number of modes in the assessment is to increase the rate of convergence, as evident in Case 1 which compare the results using the first 2 modes with that using the first 4 modes. Cases 2 and 3 both used the first 4 modes and Case 4 the first 6 modes. In Case 4, using only the first 4 modes resulted in a slow rate of convergence. For all cases S_{RR} was used in lieu of S_{RR}^* in Eqn [12], and therefore remained a constant. It was found that using S_{RR}^* in Eqn [12] as defined by Eqn. [13] resulted in a slower rate of convergence with no improvement in the final result.

Structure B

The natural frequencies for the first 4 modes of Structure B are given in Table 3. The major shift in frequency due to damage is shown to occur in mode 3, where the difference in the baseline f_0 and postflight (damaged) frequencies f_d is 0.009 Hz. The accuracy of the Guyan reduced FEM used as the analytical model in the assessment is shown to be very good in the first three modes. However, the FEM's frequency of f_a = 7.921 Hz. for the 4^{th} mode shows a significant discrepancy ($f_0 - f_a$) compared to the frequency shift due to damage ($f_0 - f_d$) . Modes higher than the 4^{th} mode were found to have an even greater discrepancy between f_0 and f_a . It is therefore advisable to include only the first 3 modes in the assessment of damage. The values for the MACs are also given in Table 3. Good correlation exist between the mode shapes of the first 4 modes of the baseline and analytical FEM, as well as the baseline and postflight modal test data. The cross orthogonality check between the FEM and measured baseline data is summarized in Table 4. It is apparent that the 4^{th} mode of the baseline data does not have good orthogonality with respect to the FEM modes, as reflected in the value of 0.795 on the diagonal and 0.028 on the off diagonal.

The residual forces of mode 1 are shown in Fig. 6. Forces at nodes not shown are 3 to 4 orders of magnitude smaller than those shown. The residual forces indicate that damage has occurred in either both or one of the elements between the residual forces (element 11 and 12). It was determined that damage had occurred only in element 11 by noting that the residual forces of Fig. 6 diminish when assigning a nonzero variance only to this member and proceeding with one update in the damage severity assessment. When assigning nonzero variances to both elements 11 and 12 the residual forces increased after performing one update. The assessment for damage severity thus preceded with a nonzero variance assigned only to element 11.

The results of the severity of damage assessment are shown in Fig. 7. The curve labeled Guyan III corresponds to using the first 4 modes, Guyan II the first 3 modes, and Guyan I the hypothetical situation of a perfectly correlated FEM with respect to the first 4 modes (e.g. Λ_a

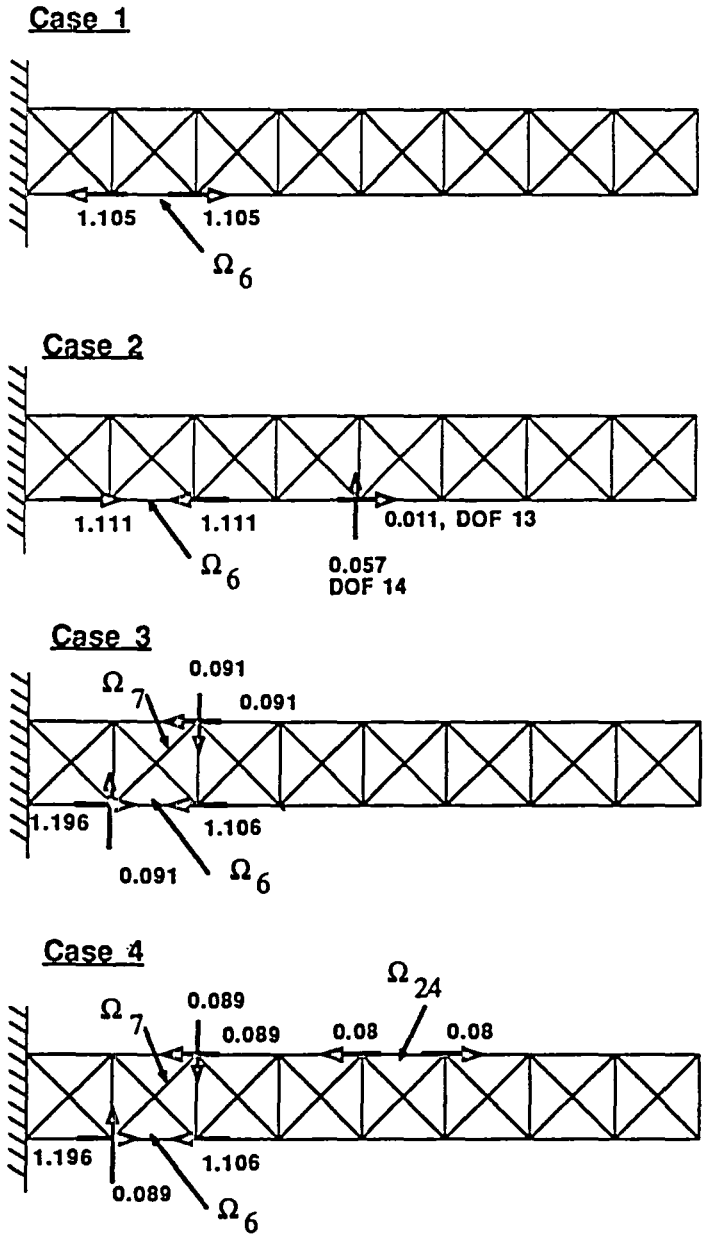

Figure 4. - Mode 1 Residual Forces for Structure A.

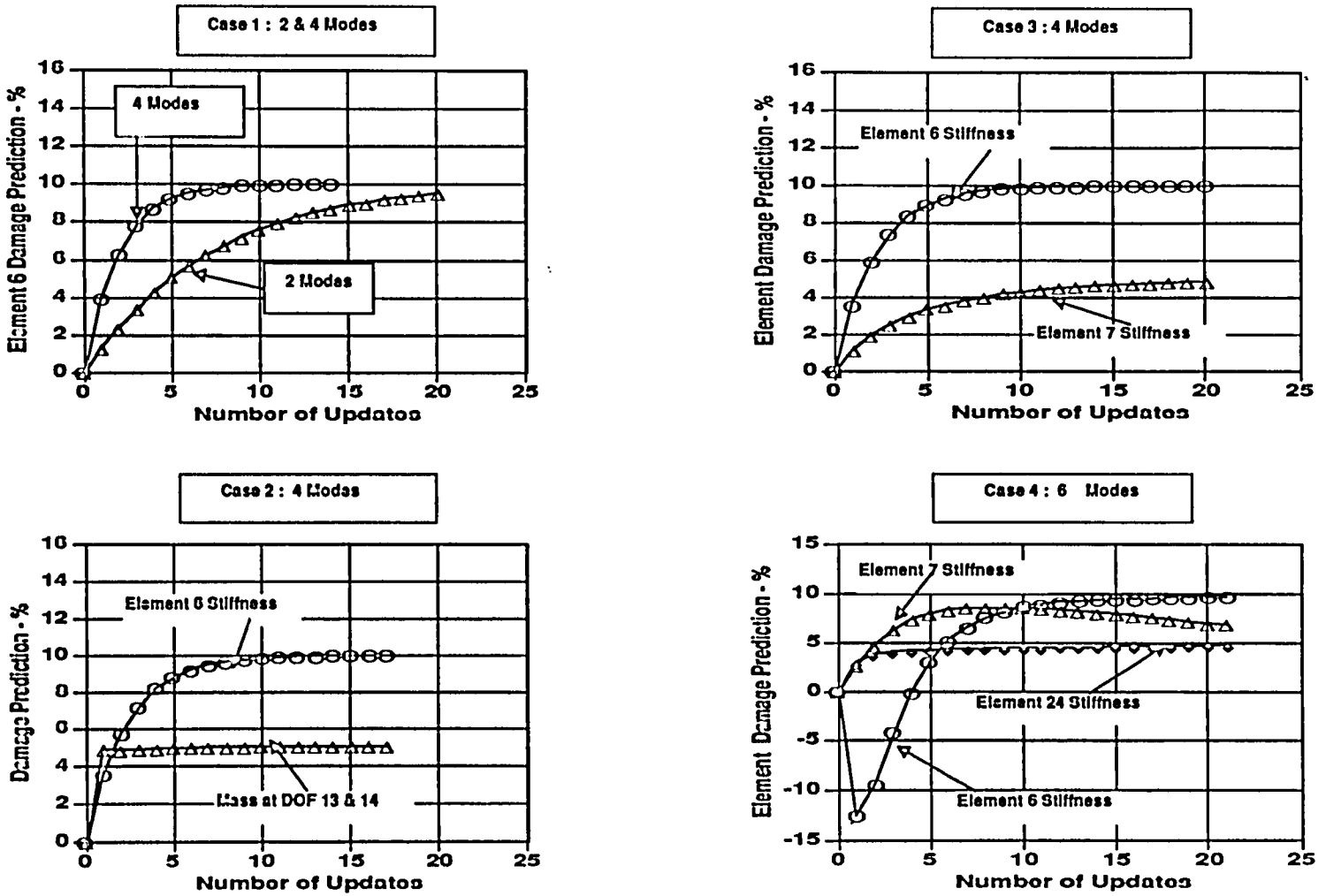

Figure 5. - Structure A Damage Assessment Results

TABLE 4. - Cross Orthogonality Check, Structure B

Test $\phi 0$ \ FEM ϕa	Mode	1	2	3	4
	1	0.999	0.001	0.001	0.011
	2	-0.004	0.999	0.003	0.008
	3	0.003	0.006	0.990	0.009
	4	0.013	0.028	0.015	0.795

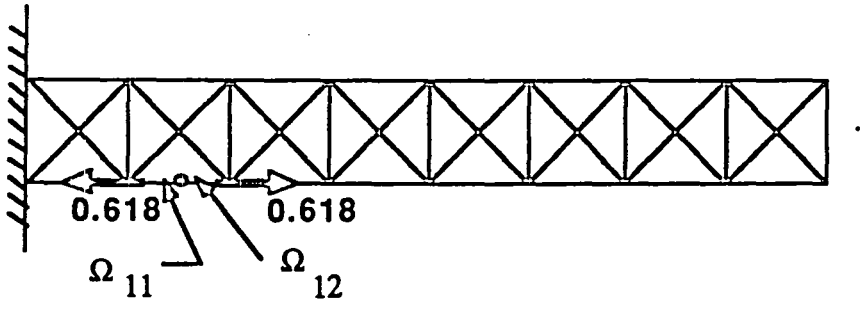

Figure 6. - Mode 1 Residual Forces for Structure B, Case 5.

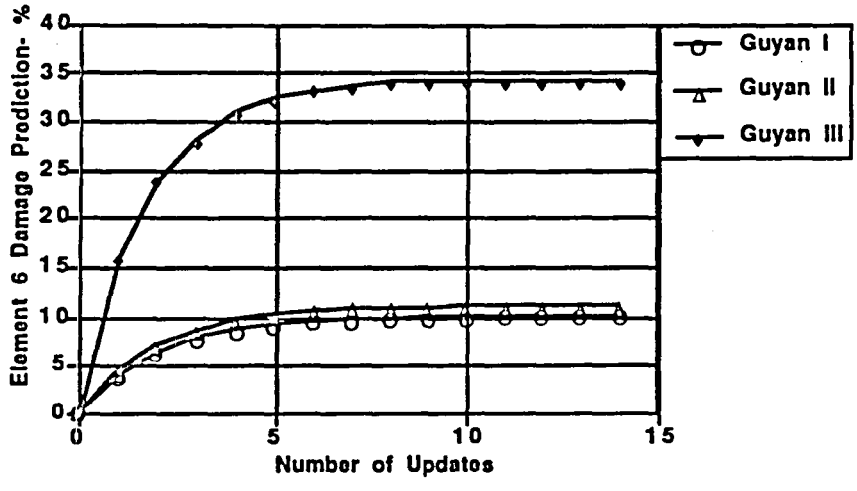

Figure 7. - Structure B Damage Assessment Results

= Λ_0). The results for Guyan I converge to the exact result of 10%, while Guyan converges to 11% and Guyan to 34%. It is apparent that the 4^{th} mode is causing the method to over predict the severity of damage in member 11 by correcting for discrepancies between Λ_a and Λ_0 in addition to assessing the extent of damage. As noted above, mode 4 was determined not to be fit for inclusion in the assessment; indicating the importance of performing and examining the results of the correlation analysis before performing the damage assessment for severity. In the event that not enough modes are correlated, one could use the damage assessment algorithm to first correct the analytical model, using λ_0 and ϕ_0 in Eqn. [7b] to locate areas in the FEM needing adjustment and using the vibration characteristics for Λ_0 and Λ_a instead of Λ_0 and Λ_d in Eqn [12] to determine the necessary correction for the FEM.

As a final comment, the differences in f_0 and f_d are small as well as those of f_0 and f_a, and in the practical sense less than the resolution of most modal testing equipment. It would be expected in a real application involving modal testing that the differences between f_0 and f_d would be greater as well as those between f_0 and f_a. The results of this study are still considered valid since it is the relative differences between $f_0 - f_d$ and $f_0 - f_a$ that are important.

CONCLUSIONS

Based on the results of this study involving a two step procedure of detecting damage and assessing its severity the following conclusions are noted:

1. The method of detecting locations of structural damage by the Residual Force Method gives good results.

2. Basing the assessment for severity of damage on suspected members, as found by the Residual Force Method, can result in an accurate assessment. The correlation of the analytical model used in the assessment algorithm with the baseline data is important. The use of frequency shift, modal assurance criteria, and cross orthogonality checks appear to give good guidance on retaining correct modes in the damage assessment for severity and minimizing the error.

Areas which are suggested for further study include:

1. An experimental verification of the methodology for detecting damage.

2. A further investigation involving the calibration of the above criteria for selecting which modes should be retained in the assessment for damage.

3. Use of the methodology to simultaneously perform system identification and assessment for damage for analytical models that are not well correlated with the baseline data.

4. Use of the method as an online damage monitoring system for large space structures such as Space Station Freedom.

Work is currently continuing in the these areas which have been suggested as needing further study.

REFERENCES

1. Chen, J.C. and Garba, J.A., "On-Orbit Damage Assessment for Large Space Structures," AIAA Journal, Vol. 26, No. 12, June 1988.

2. Chen, T.Y. and Wang. B.P., "Finite Element Model Refinement Using Modal Analysis Data," *Proceedings of AIAA/ASME 29th Structures, Structural Dynamics, and Materials Conference*, April 1988.

3. Ewins, D. J., " Modal Testing: Theory and Practice," John Wiley and Sons, Inc., 1984.

4. Kabe, A.M. " Stiffness Matrix Adjustment Using Mode Data," *AIAA Journal*, Vol. 23, No. 9, Sept. 1985.

5. Stubbs, N., T. Broone and R. Osegueda, "Nondestructive Construction Error Detection in Large Space Structures," *AIAA Journal*, Vol. 28, No. 1, 1990.

Evaluation of Cutaneous Blood Flow During Lower Body Negative Pressure To Prevent Orthostatic Intolerance of Bedrest

Final Report

NASA/ASEE Summer Faculty Fellowship Program--1991

Johnson Space Center

Prepared by:	Marilyn Rubin, Ph. D.
Academic Rank:	Professor
University and Department:	St. Louis University School of Nursing St. Louis, Mo., 63104
NASA/JSC	
Directorate:	Space and Life Sciences
Division:	Medical Sciences
Branch:	Biomedical Laboratories
JSC Colleague:	Suzanne Fortney, Ph.D.
Date Submitted:	August 9, 1991
Contract Number:	NGT-44-001-800

ABSTRACT

Orthostatic tolerance is markedly impaired in most of the crewmembers during space flight and could seriously compromise crew safety during and immediately after landing. NASA investigators are studying the use of lower body negative pressure (LBNP) as a countermeasure to this intolerance. It is hypothesized that the continuously changing vascular pressure induced by sinusoidal LBNP with an additional countermeasure of salt and water will help crewmembers to be in a more acceptable physiologic condition to enter the earth's atmosphere. This process is used by crewmembers during space flight itself.

In ground based studies, subjects on bedrest provide the model for studying the physiologic effects of weightlessness. When subjects are treated with sinusoidal LBNP, negative pressures ranging from 0 to -60 mm./Hg. are administered during a two hour period. This increases body fluids in the legs and lower body which assists crewmembers and bedrest subjects to more readily adapt to the earth's gravitational field upon assuming the upright posture.

This paper reports the results of two subjects who were placed on bedrest for six days. The subjects were randomly selected for either the control or treatment mode. The subject receiving the treatment mode ingested salt tablets and water on day 4 of the bedrest period. A ramp LBNP of two hours was next administered to this subject. The control subject did not receive anything during the bedrest period.

Laser doppler was used to measure the cutaneous blood flow of the forearm and calf to monitor vasoconstrictor effects of the baroreceptor reflex. Data indicated that skin blood flow in the treatment subject was higher than baseline in the forearm while the skin blood flow was decreased in the control subject.

The comparison of these two subjects indicated that their responses to LBNP differ, however, the positive results with the treatment subject indicates that these two countermeasures to orthostatic intolerance show promise of success.

INTRODUCTION

Orthostatic tolerance is markedly impaired in most of the crewmembers during space flight and could seriously compromise crew safety during and immediately after landing. NASA investigators are studying the use of lower body negative pressure (LBNP) as a countermeasure to this intolerance. It is hypothesized that the continuously changing vascular pressure induced by sinusoidal LBNP with an additional countermeasure of ingestion of salt tablets and water will help the crewmembers to be in a more acceptable physiologic condition to enter earth's atmosphere. This process is used by crewmembers during space flight itself.

In ground based studies, subjects on bedrest provide the model for studying the physiologic effects of weightlessness. Previous studies have shown that weightlessness in space and bedrest on the ground have similar outcomes on the body. The objectives for using LBNP are to increase plasma volume (as a result of stimulating secretions of aldosterone and anti-diuretic hormones and attenuating release of atrial natriuretic hormone) and by maintaining carotid sinus baroreceptor function, overall autonomic nervous system function and leg compliance.

Sinusoidal LBNP, ranging from 0 to -60 mm/Hg. for a two hour period of time, increases body fluids in the legs and assists crewmembers and bedrest subjects to adapt to gravitational effects, either upon re-entry into earth's gravitational field or upon assuming the upright position after bedrest. This adaptation prevents fainting and other cardiovascular problem.

During the administration of LBNP, it is important to assess the subject's physiologic responses and to monitor the effects, particularly, on the cardiovascular system. One of the significant responses to monitor is the baroreceptor vasoconstriction reflex which can be assessed by measuring cutaneous blood flow in the forearm.

Kellogg et al (1990) reported that cutaneous arterioles are controlled by both vasoconconstrictor and vasodilator sympathetic nerves. In their studies, they stated that the baroreflex clearly controls active vasodilation in skin and, therefore, has a major function in regulating cutaneous circulation. In an earlier study, Johnson et al (1973) investigated the competitive responses between cutaneous vasodilator and vasoconstrictor reflexes in man. Their findings document that skin blood flow is under both baroreceptor and thermoregulatory reflex control. Johnson and his associates assert that during heating, the skin retains the ability to vasoconstrict but the vasoconstriction does not completely override the heat induced vasodilation.

Later, Johnson (1986) further elucidated the reflex nature of regulation of circulation. He found that baroreceptor reflexes and reflexes associated with exercise each compete with thermoregulatory reflexes for control of the cutaneous circulation, but neither can overcome thermoregulatory vasodilation. He concluded that regulation of body temperature, maintainence of arterial blood pressure and redistribution of blood flow to working muscles is a result of the competition among the thermoregulatory and nonthermoregulatory reflexes.

Essandoh (1987) examined postural cardiovascular reflexes and their effects upon responses of the forearm and calf resistance vessels. Low pressure mechanoreceptors are deactivated by LBNP below -20 Torr which results in constriction of forearm but not calf resistance vessels. However, unloading both low and high pressure mechanoreceptors by lower body negative pressure of more than -20 Torr causes a large and similar constriction of both the forearm and the calf vessels. During postural changes, from supine to sitting positions, the major reflex adjustments to these changes in posture take place in the forarm.

Skin vasomotion responses may be seen by monitoring circulation with a laser doppler. This method of monitoring red blood cell velocity provides information about blood perfusion in a safe, non-invasive manner at the cutaneous surface. Laser doppler flowmeters work on the principle that a laser light beam is scattered by moving red blood cells. This movement is reflected into the photodector.

METHODOLOGY

This investigator participated in an ongoing study of subjects on bedrest. At this time, two of the subjects have completed the 6 day bedrest period. Criteria for subject selection included the following: normal, healthy males in the age range of 25-50 (the same age range for selection of astronauts), successful physical examination and successful stress testing on the treadmill.

Prior to entry into the study, each subject received a full explanation of the study and signed a consent form for voluntary participation. The study was approved by the NASA Human Investigation Committee.

The subject then presented hinself at the laboratory for a practice protocol of the study. Later, during the data collection phase, the subject during pre-bedrest, during bedrest (for treatment subject) and at post-bedrest, entered the LBNP box or chamber. The subject placed his legs into the chamber with his waist at the iris or the opening of the chamber. A heavy elastic skirt, placed around the subject's waist, was attached to the chamber and provided the seal necessary to prevent leakage of air into the chamber during LBNP.

The subject was connected to a number of monitors of physiologic variables. These were instruments for obtaining the electrocardiogram, echocardiogram, automatic and manual blood pressure indicators, strain gauge on the leg to record volume change, plethysmograph to evaluate blood volume in the arm, and laser doppler instruments to measure blood flow in the forearm and the calf.

This investigator was responsible for monitoring the laser doppler method of measuring blood flow of the skin. The data and results of this part of the study are reported here.

Two laser doppler instruments were used. The Perimed Laser Doppler Flowmeter, Periflux PF2B, was used for recording blood flow in the left forearm through a probe that was placed within a small heater (set at 38 degrees centigrade) and connected to the skin with a two sided adhesive ring. The Perimed instrument has a 2 nW He-Ne laser of 632.8 nm wavelength. At the normal skin, it has a hemisphere of approximatly 1 mm. radius. It measures skin blood flow at a depth of 1 mm.

The second laser doppler instrument was the Vasamedics Laserflo BPM 2. The probe from this instrument was placed on the calf of the subject. There was no heater attached to the probe. The wave length of the laser was 780 nm. It measures skin blood flow at a depth of 1 mm.

Monitoring was continuous for collection of data for baseline, during the LBNP, after release of negative pressure and duing recovery.

RESULTS

The subjects were randomly selected for either the treatment or the control condition. Subject A was designated as the control subject and Subject B as the treatment subject. The results of the data are presented graphically in illustrations.

In Figure 1, the baseline data is presented prior to LBNP. The data is from the left forearm only of the two subjects. The course of cutaneous blood flow for these two subjects is very dissimilar. Subject A has an inconsistent response and tolerates the negative pressure to a level of -100 mm./Hg. On the other hand, Subject B has a consistent response and tolerates the negative pressure to -70 mm./Hg. This difference may be explained by the difference in states of tension during LBNP. Subject B was much more relaxed that Subject A. Both subjects showed blood flow values above baseline when the negative pressure was released and slightly below baseline during the three minute recovery time.

In Figure 2, Subject A's data are presented for both the pre-

bedrest LBNP and from the sixth day of bedrest. Measurements were made of cutaneous blood flow of the left forearm and the calf. When measurements were repeated, care was taken to measure at the same place on the skin. Post bedrest values of blood flow for the forearm are reduced. The calf blood flow is also reduced below the forearm blood flow and at the negative pressure levels of -50, -60, and -70 nn./Hg. approached zero. In order to more readily view the values for the calf blood flow, the date were increased by a factor of 10. The zero readings may be from stasis within the capillaries or possibly from a collapse of the vessel from the negative pressure. In any event, there is no movement of red blood cells.

Subject B was tested on the fourth day of bedrest prior to ingestion of salt pills and water. In Figure 3, the forearm values show a reduction in blood flow on Day 4. Following the ingestion of salt and water, the subject received a ramp LBNP, using sinusoidal negative pressures going from 0 to -60 mm./Hg. within 5 minute intervals for a period of two hours. On the sixth day of bedrest, this subject's cutaneous blood flow was increased over baseline, indicating that the countermeasures were successful.

In Figure 4, the cutaneous blood flow of the forearm and the calf of Subject B are displayed. Values for the calf blood flow are again increased by a factor of 10. When compared, the blood flow of the right calf was decreased on the sixth day of bedrest during LBNP. At the -70 mm./Hg. of pressure, the blood flow was zero in the calf, just prior to release of the negative pressure.

DISCUSSION

These two subjects had dissimilar responses in cutaneous blood flow during LBNP. However, the data for Subject B, who received the treatment mode, showed that the countermeasures had improved the responses of the forearm and an increased level of blood perfusion which is the desired outcome. Subject A, control mode, did not show this adaptation.

References

Nilson, G., T. Tenland, and P. Oberg. Evaluation of a laser doppler flowmeter for measurement of tissue blood flow. IEEE Transactions on Biomedical Engineering, 27: 597-604, 1980.

Essandoh, L., D. Duprez and J. Shepherd. Postural cardiovascular refexes: comparison of responses of forearm and calf resistance vessels. J. Appl. Physiol. 63: 1801-1805, 1987.

Johnson, J., G. Brengelmann, J. Hales, P. Vanhoutte and C.Wenger. Regulation of the cutaneous circulation. Federation Proc.45: 2841-2850, 1986.

Johnson, J., M. Niederberger, L. Rowell, M. Eisman, and G. Brengelmann. Competition between cutaneous vasodilator and vasoconstrictor reflexes in man. J. Appl. Physiol. 35(6): 798-803, 1973.

Kellogg, D., J. Johnson, and W. Kosiba. Baroreflex control of the cutaneous active vasodilator system in humans. Circ. Res. 66: 1420-1426, 1990.

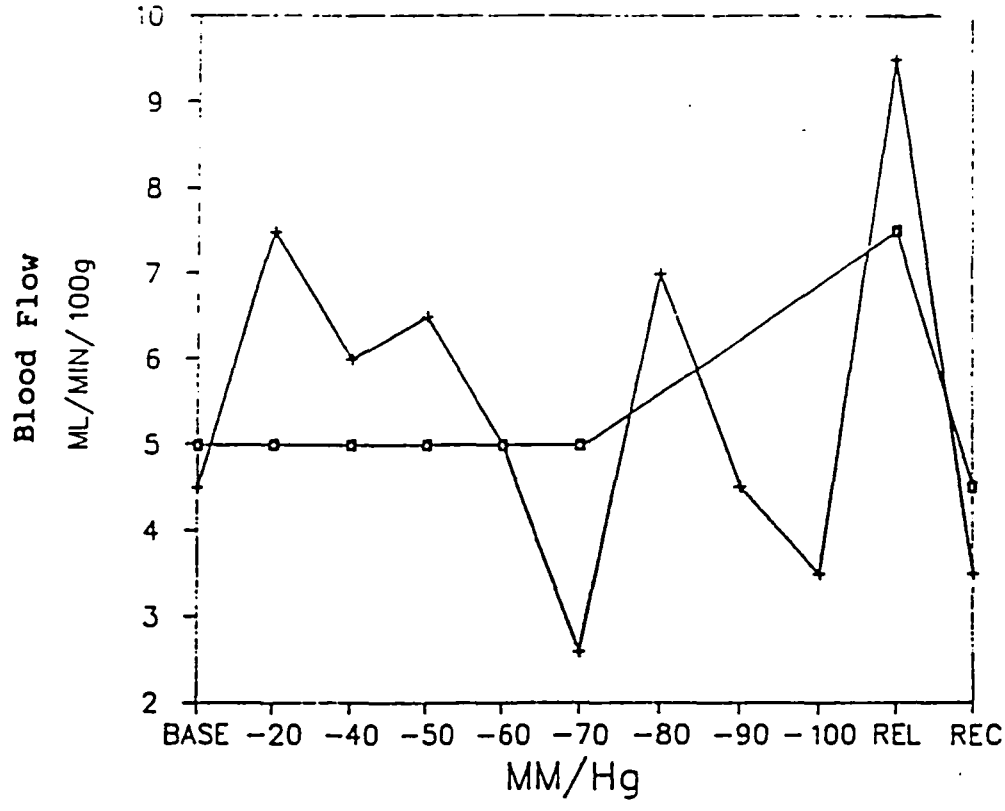

Figure 1. Subjects A and B Pre-bedrest Forearm Blood Flow (□ Treatment, + Control)

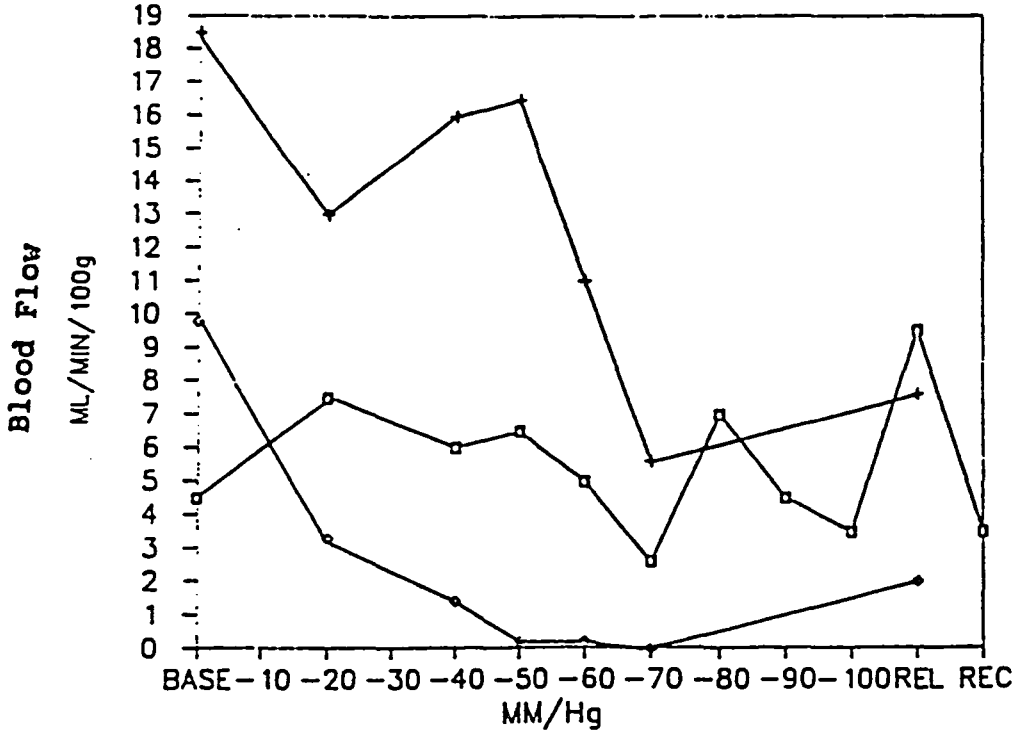

Figure 2. Subject A's Left Forearm and Right Calf Blood Flow (□ left forearm, pre-bedrest, + left forearm, day 6, ◊ right calf, day 6)

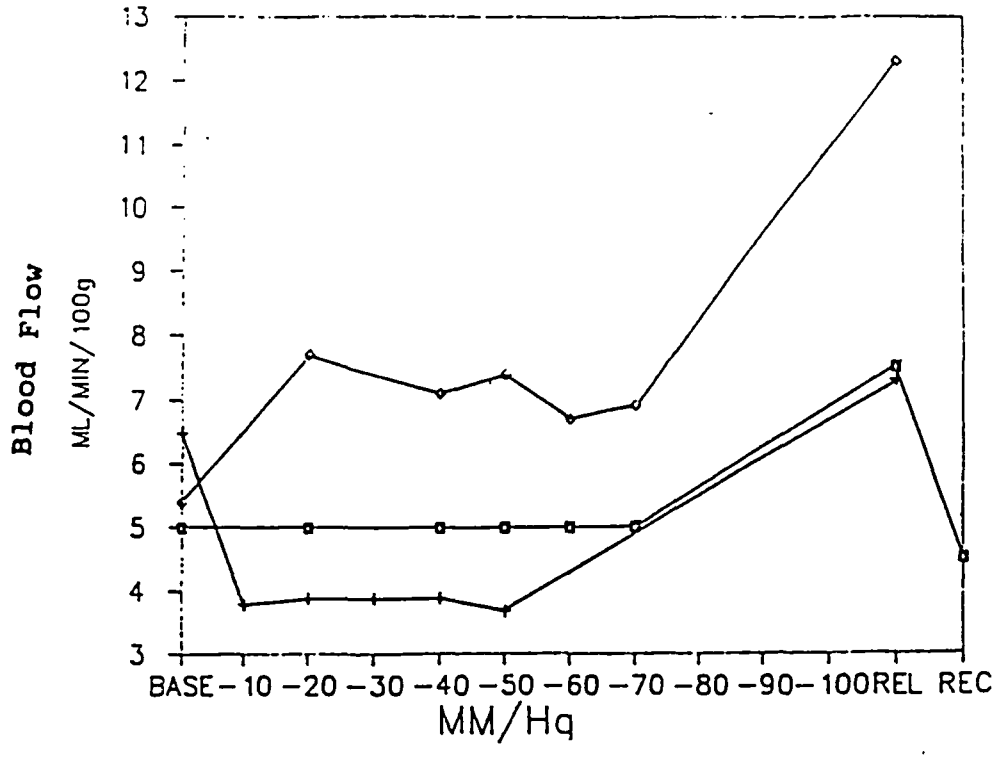

Figure 3. Subject B's Left Forearm Blood Flow (□ pre-bedrest, + day 4, ◊ day 6).

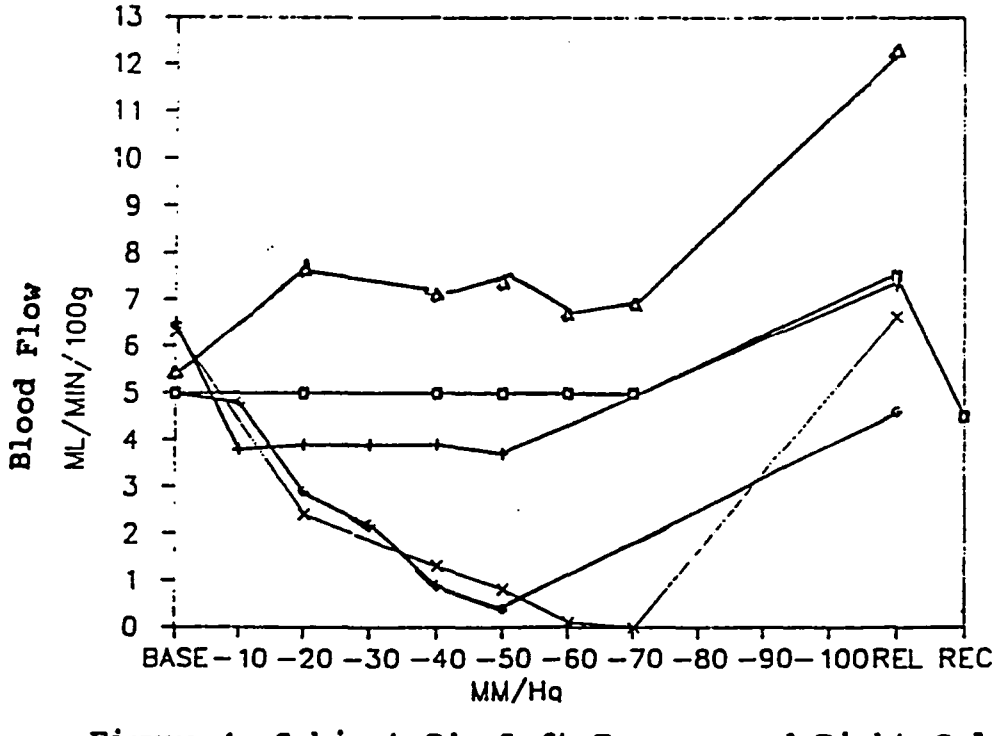

Figure 4. Subject B's Left Forearm and Right Calf Blood Flow (forearm, □ pre-bedrest, + day 4, △ day 6; calf, ◊ day 4, x̄ day 6.

THE DEVELOPMENT OF HIGH ORDER NUMERICAL TECHNIQUES FOR REENTRY SIMULATION OF HYPERSONIC SPACECRAFT

Final Report

NASA/ASEE Summer Faculty Fellowship Program – 1991

Johnson Space Center

Prepared By:	Richard Sanders
Academic Rank:	Associate Professor
University and Dept.:	University of Houston - University Park Department of Mathematics Houston, Texas 77204-3476
NASA/JSC	
Directorate:	Engineering and Development
Division:	Navigation, Control and Aeronautics Division
Branch:	Aeroscience Branch
JSC Colleague:	Chin Li
Date Submitted:	November 15, 1991
Contract Number:	NGT 44-001-800

Abstract. The primary difficulty encountered when simulating hypersonic flow is the flow normally includes strong nonlinear discontinuities. These discontinuities fall into three broad classes: shocks, slip-lines and rarefaction waves. Moreover, in the hypersonic flow regime, the chemistry of hot gases plays a vital role and can not be neglected. These facts combine to make the numerical treatment of spacecraft reentry a most challenging problem. In this work, we develop a class of finite difference schemes that accurately resolve discontinuous solutions to spacecraft reentry flow and are simple to incorporate into existing spacecraft reentry codes.

§1. Introduction. The most simple finite difference schemes for the numerical approximation of partial differential equations are easy to motivate. Basically what one does is replace derivatives by finite difference quotients that approximate them. However, this recipe does not alway guarantee a stable scheme. To see this, consider the pde:

$$\begin{aligned} &\frac{\partial u}{\partial t} + \lambda \frac{\partial u}{\partial x} = 0 \\ &u(x,0) = u_0(x). \end{aligned} \tag{1.1}$$

Let t^n denote $n\Delta t$ with $n = 0,1,2,\ldots$ and x_j denote $j\Delta x$ with $j = \ldots,-1,0,1,\ldots$. Let the grid function u_j^n approximate $u(x_j,t^n)$. One possible finite difference scheme to approximate the solution to the pde above is:

$$\text{Replace } \frac{\partial u}{\partial t} \text{ with } \frac{u_j^{n+1} - u_j^n}{\Delta t}.$$
$$\text{Replace } \frac{\partial u}{\partial x} \text{ with } \frac{u_{j+1}^n - u_{j-1}^n}{2\Delta x}.$$

This gives and explicit time marching scheme

$$u_j^{n+1} = u_j^n - \frac{\Delta t}{2\Delta x}\lambda(u_{j+1}^n - u_{j-1}^n).$$

Applying this scheme to discrete initial data

$$u_j^0 = e^{i\theta x_j},$$

we obtain an exact solution

$$u_j^n = (g(\theta\Delta x))^n e^{i\theta x_j}$$
$$g(\theta) = 1 - \frac{\Delta t}{\Delta x}\lambda i \sin(\theta).$$

$g(\theta)$ is called the amplification factor. For all $\pi > |\theta| > 0$ we have that $|g(\theta)| > 1$. Therefore, the amplitude of every wave component with $\pi > |\theta\Delta x| > 0$ blows up geometrically – this scheme is unstable.

A desirable feature of the scheme above is the centered difference approximation for $\partial/\partial x$. In addition to its second order accuracy, central space differencing schemes require only a three point stencil. There are ways to construct *linearly stable* central space differencing finite difference schemes to solve (1.1). For example,

$$\text{Replace } \frac{\partial u}{\partial t} \text{ with } \frac{u_j^{n+1} - u_j^n}{\Delta t}.$$
$$\text{Replace } \frac{\partial u}{\partial x} \text{ with } \frac{u_{j+1}^{n+1} - u_{j-1}^{n+1}}{2\Delta x},$$

defines what is called backward Euler time discretization. This implicit scheme is unconditionally stable. Another implicit scheme that is unconditionally stable is the trapezoidal rule. It is given by

$$\text{Replace } \frac{\partial u}{\partial t} \text{ with } \frac{u_j^{n+1} - u_j^n}{\Delta t}.$$
$$\text{Replace } \frac{\partial u}{\partial x} \text{ with } \frac{1}{2}\left(\frac{u_{j+1}^n - u_{j-1}^n}{2\Delta x} + \frac{u_{j+1}^{n+1} - u_{j-1}^{n+1}}{2\Delta x}\right).$$

While these two implicit schemes are stable and therefore convergent for smooth data, they both work poorly for problems that have discontinuous solutions. This fact results from their large phase errors in the high frequencies. It is also possible to build an explicit conditionally stable centered scheme by the addition of artificial viscosity. A second order in space and time scheme for (1.1) is the popular Lax-Wendroff scheme

$$u_j^{n+1} = u_j^n - \frac{\Delta t}{2\Delta x}\lambda(u_{j+1}^n - u_{j-1}^n) + \frac{1}{2}(\frac{\Delta t}{\Delta x}\lambda)^2(u_{j+1}^n - 2u_j^n + u_{j-1}^n).$$

This scheme also produces poor results when the solution to (1.1) is not smooth. To see this, consider (1.1) with $\lambda = 1$ and with initial data

$$u(x,0) = u_0(x) = \begin{cases} 1 & \text{if } |x - 1/2| \le 0.10 \\ 0 & \text{otherwise} \end{cases},$$

(see the left pulse around $x = 0.5$ in figure 1.1). The exact solution to this problem at $t = 1.0$ is just the pulse translated to the right by 1 unit, (see the right pulse around $x = 1.5$). The small boxes in figure 1.1 depict the numerical results to this problem coming from the Lax-Wendroff difference scheme.

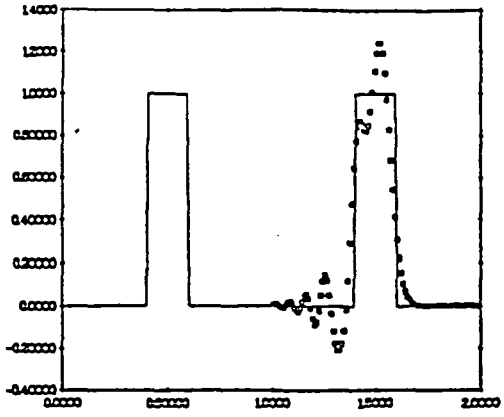

Figure 1.1. The solid line represents the initial data and exact solution at $t = 1.0$. The small boxes indicate the grid values coming from the Lax-Wendroff difference scheme.

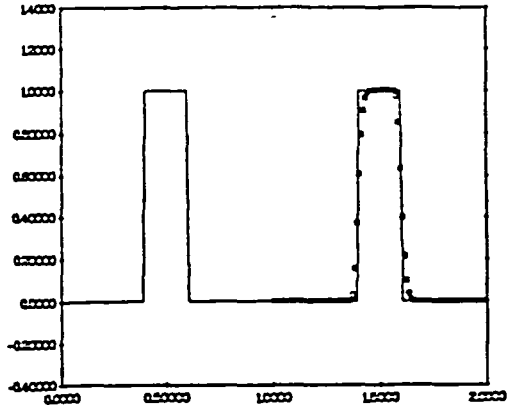

Figure 1.2. The solid line represents the initial data and exact solution at $t = 1.0$. The small boxes indicate the grid values coming from one of our modified fourth order central difference schemes.

The *wiggles* are a result of the high frequency phase error inherent to the Lax-Wendroff scheme.

When simulating the flow of air around hypersonic spacecraft on reentry, large gradient flows are the rule and not the exception. It should be obvious from the simple example above that traditional finite difference schemes can yield less than satisfactory results in these flow regimes. A certain amount of care must therefore be given to the design of numerical approximation techniques to accurately solve hypersonic flow problems. Eliminating nonphysical oscillations that are intrinsic to approximations coming from centered schemes applied to nonlinear systems of conservation laws is the main focus of this work. We modify a class of central space difference schemes to completely eliminate spurious numerical oscillations found in the example above. Compare the results coming from one of our modified central schemes presented in figure 1.2. Our modified schemes are intended to be simple enough so as to easily lend themselves to reliably approximate solutions to the equations governing the reentry of hypersonic spacecraft.

§2. The modified centered scheme for the scalar law. In this section, we develop a simple modification to a central differencing scheme applied to nonlinear, scalar, conservation laws of the form:

$$\frac{\partial}{\partial t}u + \frac{\partial}{\partial x}f(u) = 0. \tag{2.1}$$

An explicit forward Euler in time and central differencing in space finite difference formula applied to this problem is written as

$$u_j^{n+1} = u_j^n - \frac{\Delta t}{\Delta x}\left(f(u_{j+1/2}^n) - f(u_{j-1/2}^n)\right), \tag{2.2}$$

where u_j^n is used to indicate the approximation of $u(x,t)$ at time level t^n and spatial grid block centered at x_j. $u_{j+1/2}^n$ will be used here to denote some approximation to $u(x_{j+1/2}, t^n)$. For example, if we take

$$u_{j+1/2}^n = \frac{1}{2}(u_{j+1}^n + u_j^n),$$

then the resulting scheme is second order accurate in space and first order in time. One could hardly ask for a simpler approximation scheme to solve a partial differential equation. Unfortunately, as demonstrated above, this second order in space central differencing scheme is strictly unstable. To stabilize the central space differencing approach, we add a *parameter free* nonlinear artificial viscosity term to the right hand side of (2.2). This added viscosity term will have the property that in regions where the numerical approximation is not at a local extrema, the numerical viscosity term is identically zero.

Throughout this section, we make the following assumptions concerning the midpoints required by the forward Euler difference scheme (2.2):

(2.3a) For each j, the midpoint $u_{j+1/2}$ is given by a continuous function of grid values u_k, $k = j, j \pm 1, j \pm 2, \ldots$.

(2.3b) For each j, the midpoint $u_{j+1/2}$ is restricted to lie in the interval given by neighboring grid values u_j and u_{j+1}.

The minmod function is defined by

$$\text{minmod}(x,y) = \begin{cases} \min(|x|,|y|)\text{sign}(x) & \text{if } x \cdot y \le 0 \\ 0 & \text{if } x \cdot y > 0 \end{cases},$$

and we shall use the notation $\widehat{u_L}_j^n = u_{j-1/2}^n - u_j^n$ and $\widehat{u_R}_j^n = u_{j+1/2}^n - u_j^n$. At each point $x_{j+1/2}$ midway between grid blocks, we consider left and right point values given by the formulae

$$\text{(2.4)} \qquad \begin{aligned} v_{j+1/2}^l &= u_j^n + \text{minmod}(\widehat{u_R}_j^n, \rho\widehat{u_L}_j^n), \\ v_{j+1/2}^r &= u_{j+1}^n + \text{minmod}(\widehat{u_L}_{j+1}^n, \rho\widehat{u_R}_{j+1}^n), \end{aligned}$$

where $\rho \ge 0$ is a finite parameter.

Remark 1: If (2.4), with any fixed $\rho > 1$, is applied to a smooth function $u(x)$ that has no local extreme points in the interval $(x_{j-1/2}, x_{j+3/2})$, then for Δx sufficiently small

$$\text{(2.5)} \qquad v_{j+1/2}^l = v_{j+1/2}^r = u_{j+1/2}^n.$$

(The parameter ρ does not depend in any way on the grid size.)

Our modified forward Euler centered scheme now reads

$$\text{(2.6)} \qquad u_j^{n+1} = u_j^n - \frac{\Delta t}{\Delta x}\left(h_f(v_{j+1/2}^r, v_{j+1/2}^l) - h_f(v_{j-1/2}^r, v_{j-1/2}^l)\right),$$

where $h_f(u_1, u_2)$ is any continuous 2 point monotone flux function that is consistent to $f(u)$ in the sense that

$$h_f(u, u) = f(u);$$

see [4]. Referring back to (2.5), note that we should expect generically that

$$h_f(v^r_{j+1/2}, v^l_{j+1/2}) = f(u^n_{j+1/2}),$$

so we should expect that generically (2.6) will reduce to the centered scheme given in (2.2). The modified scheme can be written as

$$u^{n+1}_j = u^n_j - \frac{\Delta t}{\Delta x}\big(f(u^n_{j+1/2}) - f(u^n_{j-1/2}) - (Q_{j+1/2} - Q_{j-1/2})\big), \tag{2.7}$$

where

$$Q_{j+1/2} = f(u^n_{j+1/2}) - h_f(v^r_{j+1/2}, v^l_{j+1/2}),$$

so as to indicate the particular form of the modification to the centered scheme (2.2).

The modified forward Euler central difference scheme (2.6) satisfies in an obvious way the following theorem:

THEOREM 1. *Suppose all intermediate points $u^n_{j+1/2}$ satisfy (2.3). Let Δt_h denote the time step stability limit for the first order monotone scheme*

$$u^{n+1}_j = u^n_j - \frac{\Delta t}{\Delta x}\big(h_f(u^n_{j+1}, u^n_j) - h_f(u^n_j, u^n_{j-1})\big).$$

If the time step size Δt in (2.6) is taken so that

$$\Delta t \le \frac{1}{\rho + 1}\Delta t_h,$$

for the fixed $1 \le \rho < \infty$ in (2.4), then we have for each $n > 0$

$$\min_j u^0_j \le u^n_j \le \max_j u^0_j.$$

Moreover, if we use $Var(u_j)$ to denote the usual pointwise variation of a grid values u_j, we have for each $n > 0$

$$Var(u^n_j) \le Var(u^0_j).$$

Remark 2: From the statement of Theorem 1, one should ask the following paradoxical question: Remark 1 seems to imply that if the solution to the pde that (2.6) approximates is smooth, then (2.6) reduces generically to the strictly unstable scheme (2.2). How can

the claim of the theorem then be correct? This question will be addressed at the end of this section.

Proof of Theorem 1: In each cell $I_j \equiv [x_{j-1/2}, x_{j+1/2})$ determine a number θ_j such that

$$(1/2+\theta_j)(v^r_{j-1/2}-u^n_j)+(1/2-\theta_j)(v^l_{j+1/2}-u^n_j)=0.$$

From the definitions of $v^r_{j-1/2}$ and $v^l_{j+1/2}$ we have for each j

$$|\theta_j| \le 1/2\left|\frac{\rho-1}{\rho+1}\right|.$$

Cut I_j into two pieces with the dividing point given by $\tilde{x}_j = x_j + \theta_j\Delta x$; that is $I_j = [x_{j-1/2}, \tilde{x}_j) \cup [\tilde{x}_j, x_{j+1/2}) \equiv I^l_j \cup I^r_j$. Redistribute data u^n onto a nonuniform mesh given by $\bigcup_j (I^l_j \cup I^r_j)$, and let $\tilde{u}^n$ denote the redistributed data:

$$\tilde{u}^n(x) = \begin{cases} v^r_{j-1/2} & \text{if } x \in I^l_j \\ v^l_{j+1/2} & \text{if } x \in I^r_j \end{cases}.$$

Scheme (2.6) amounts to nothing more than a classic monotone finite difference scheme applied to data $\tilde{u}^n$ on a nonuniform mesh, and reaveraged back onto the original mesh. Since the minimum grid spacing of the nonuniform mesh is

$$\frac{1}{\rho+1}\Delta x,$$

the results in [4] make the results of the present theorem obvious.

The backward Euler version of (2.6) reads:

$$u^{n+1}_j = u^n_j - \frac{\Delta t}{\Delta x}\left(h_f(v^r_{j+1/2}, v^l_{j+1/2}) - h_f(v^r_{j-1/2}, v^l_{j-1/2})\right), \tag{2.8}$$

where for the implicit scheme we define

$$\widehat{u_{Lj}}^{n+1} = u^{n+1}_{j-1/2} - u^{n+1}_j$$
$$\widehat{u_{Rj}}^{n+1} = u^{n+1}_{j+1/2} - u^{n+1}_j$$

to get

$$v^l_{j+1/2} = u^{n+1}_j + \text{minmod}(\widehat{u_{Rj}}^{n+1}, \rho\widehat{u_{Lj}}^{n+1}),$$
$$v^r_{j+1/2} = u^{n+1}_{j+1} + \text{minmod}(\widehat{u_{Lj+1}}^{n+1}, \rho\widehat{u_{Rj+1}}^{n+1}).$$

We assume that the midpoint values $u^{n+1}_{j+1/2}$ are given by a continuous function of grid values at time level $n+1$, and that they satisfy (2.3). Therefore, both $v^l_{j+1/2}$ and $v^r_{j+1/2}$ are continuous functions of grid values.

THEOREM 2. *The results of the previous theorem remain valid for the backward Euler scheme (2.8) without any CFL restrictions regardless of the size of* $1 \le \rho < \infty$.

Proof: The idea here is quite simple. Consider a compact and convex subspace of the space of sequences defined by

$$\mathcal{D} = \{x : \mathrm{Var}(x_j) \le \mathrm{Var}(u_j^n)\} \cap \{x : \min_j(u_j^n) \le x_j \le \max_j(u_j^n)\}.$$

Next, define

$$v_{j+1/2}^l(x) = x_j + \mathrm{minmod}(\widehat{x_R}_j, \rho\widehat{x_L}_j),$$
$$v_{j+1/2}^r(x) = x_{j+1} + \mathrm{minmod}(\widehat{x_L}_{j+1}, \rho\widehat{x_R}_{j+1}),$$

and $\Delta F_j(x)$ by

$$\Delta F_j(x) = h_f(v_{j+1/2}^r(x), v_{j+1/2}^l(x)) - h_f(v_{j-1/2}^r(x), v_{j-1/2}^l(x)).$$

We use

$$u_j^{n+1} = u_j^n - \frac{\Delta t}{\Delta x}\Delta F_j(u^{n+1}).$$

to denote the backward Euler scheme (2.8). We will show: (i) The implicit equation above has a solution. (ii) The solution obeys the stability results of Theorem 1. In order to accomplish these goals, consider the continuous map $\mathcal{F}$ on $\mathcal{D}$ defined by

$$\mathcal{F}_j(x) = x_j - \epsilon\left(x_j + \frac{\Delta t}{\Delta x}\Delta F_j(x) - u_j^n\right).$$

$\mathcal{F}$ can be rewritten as

$$\mathcal{F}_j(x) = (1-\epsilon)\left(x_j - \frac{\epsilon}{1-\epsilon}\frac{\Delta t}{\Delta x}\Delta F_j(x)\right) + \epsilon u_j^n.$$

From Theorem 1 it is clear that for ϵ small enough

$$\mathrm{Var}(\mathcal{F}_j(x)) \le (1-\epsilon)\mathrm{Var}(x_j) + \epsilon\mathrm{Var}(u_j^n),$$
$$(1-\epsilon)\min_j(x_j) + \epsilon\min_j(u_j^n) \le \mathcal{F}_j(x) \le (1-\epsilon)\max_j(x_j) + \epsilon\max_j(u_j^n).$$

Therefore, we have that $\mathcal{F} : \mathcal{D} \to \mathcal{D}$. So by the Schauder fixed-point theorem [1], there exists a $u^{n+1} \in \mathcal{D}$ such that $u^{n+1} = \mathcal{F}(u^{n+1})$, and the fixed-point u^{n+1} is a solution to the backward Euler scheme (2.8). Moreover, since $u^{n+1} \in \mathcal{D}$ it also satisfies the desired stability properties.

A second order central differencing scheme is generated by the intermediate point value formula

$$u_{j+1/2} = \frac{1}{2}(u_{j+1} + u_j). \tag{2.9}$$

Clearly (2.9) satisfies conditions (2.3a) and (2.3b). We now derive a fourth order in space centered scheme. Let $c_{j+1/2}(x)$ denote the cubic polynomial that interpolates the cell averages u_{j-1}, u_j, u_{j+1} and u_{j+2} on cells $(x_{j-3/2}, x_{j-1/2})$, $(x_{j-1/2}, x_{j+1/2})$, $(x_{j+1/2}, x_{j+3/2})$ and $(x_{j+3/2}, x_{j+5/2})$ respectively. If $c_{j+1/2}(x)$ is applied to the values of a smooth function $u(x,\cdot)$, we have that $c_{j+1/2}(x_{j+1/2}) = u(x_{j+1/2},\cdot) + \epsilon(x_{j+1/2})$, where $\epsilon(x)$ depends smoothly on x and $\epsilon(x) = O(\Delta x^4)$. Therefore, since

$$\frac{1}{\Delta x}\int_{x_{j-1/2}}^{x_{j+1/2}} \frac{\partial}{\partial x} f(u(x,t))\, dx = \frac{1}{\Delta x}\left(f(u(x_{j+1/2},t)) - f(u(x_{j-1/2},t))\right),$$

we have that this is equal to

$$\frac{1}{\Delta x}\left(f(c_{j+1/2}(x_{j+1/2})) - f(c_{j-1/2}(x_{j-1/2}))\right) + O(\Delta x^4).$$

The formula for $c_{j+1/2}(x_{j+1/2})$ is

$$c_{j+1/2}(x_{j+1/2}) = \frac{1}{2}(q_l + q_r), \tag{2.10}$$

where,

$$q_l = \frac{1}{2}(u_{j+1} + u_j) - \frac{1}{6}(u_{j+1} - 2u_j + u_{j-1})$$
$$q_r = \frac{1}{2}(u_{j+1} + u_j) - \frac{1}{6}(u_{j+2} - 2u_{j+1} + u_j),$$

however, $c_{j+1/2}(x_{j+1/2})$ does not always satisfy (2.3). Verification of (2.3) is crucial! We can ensure that (2.3) is satisfied by modifying q_l and/or q_r when necessary. We have taken the following approach: Let

$$\begin{aligned}\tilde{q}_l &= \frac{1}{2}(u_{j+1} + u_j) \\ &\quad - \frac{1}{6}\min(|u_{j+1} - 2u_j + u_{j-1}|, 3|u_{j+1} - u_j|)\mathrm{sign}(u_{j+1} - 2u_j + u_{j-1}), \\ \tilde{q}_r &= \frac{1}{2}(u_{j+1} + u_j) \\ &\quad - \frac{1}{6}\min(|u_{j+2} - 2u_{j+1} + u_j|, 3|u_{j+1} - u_j|)\mathrm{sign}(u_{j+2} - 2u_{j+1} + u_j),\end{aligned} \tag{2.11}$$

and note that $\tilde{q}_l$ and $\tilde{q}_r$ verify (2.3). So we define

$$u_{j+1/2} \equiv \frac{1}{2}(\tilde{q}_l + \tilde{q}_r) \tag{2.12}$$

and note that (2.12) satisfies (2.3) as well. However, when (2.12) is applied to a smooth function away from local extrema, we have that for sufficiently small Δx

$$u_{j+1/2} \equiv \frac{1}{2}(q_l + q_r) = c_{j+1/2}(x_{j+1/2}),$$

therefore giving the desired accuracy away from extreme points of the solution.

We conclude this section by addressing Remark 2. Consider the linear pde with 1-periodic boundary conditions

$$\begin{aligned} &\frac{\partial}{\partial t}u + \frac{\partial}{\partial x}u = 0 \\ &u(0,t) = u(1,t) \\ &u(x,0) = \sin(2\pi x). \end{aligned} \tag{2.13}$$

To approximate the solution to this pde, we will use the following fourth order in space, forward Euler scheme:

$$u_j^{n+1} = u_j^n - \frac{\Delta t}{\Delta x}(v_{j+1/2}^l - v_{j-1/2}^l), \tag{2.14}$$

where

$$\begin{aligned} v_{j+1/2}^l &= u_j^n + \text{minmod}(\widehat{u_R}_j^n, \rho\widehat{u_L}_j^n) \\ \widehat{u_L}_j^n &= u_{j-1/2}^n - u_j^n \quad \widehat{u_R}_j^n = u_{j+1/2}^n - u_j^n \\ u_{j+1/2}^n &= \frac{1}{2}(\tilde{q}_l + \tilde{q}_r), \quad \text{see (2.11).} \end{aligned}$$

Notice that at grid points where the approximate solution generated by (2.14) is <u>not</u> near a local extremum, we have that

$$v_{j+1/2}^l = \frac{1}{2}(q_l + q_r), \quad \text{see (2.10),}$$

and one can easily verify that (2.14), using these point values, is strictly unstable – for every nontrivial Fourier mode. However, the results of Theorem 1 imply that the approximate solution generated by the full nonlinear scheme (2.14) is stable. What in fact happens is the following: The scheme away from extrema is unstable and all Fourier modes are geometrically amplified. When an oscillation begins to form, the nonlinear *limiting* mechanism kicks in where local extreme points appear. This limiting will tend to flatten out extreme points producing a *staircase* effect. This phenomena is demonstrated using (2.14) to approximate the solution to (2.13) using $\Delta x = 1/100$ and the results are plotted in figure 2.1 at $t = 1.0$

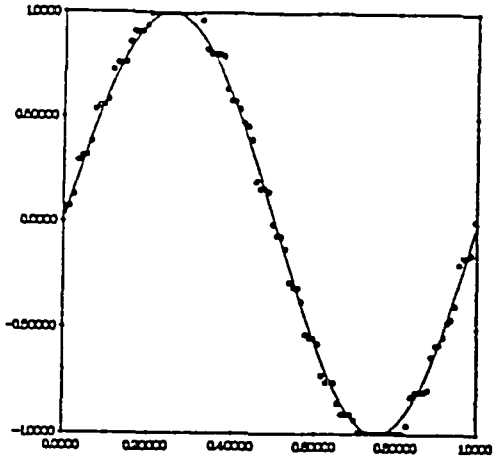

Figure 2.1. The solid line represents the exact solution to (2.13) at $t = 1.0$. The circles depict the approximate solution coming from (2.14).

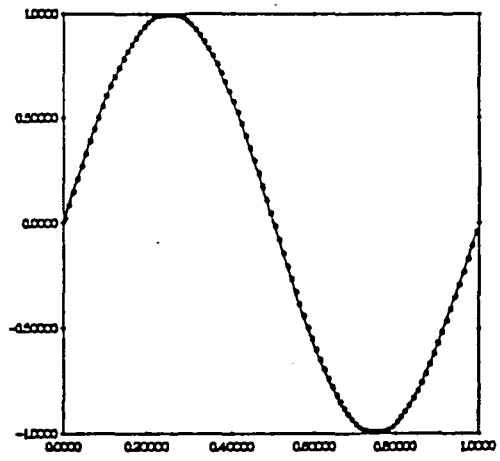

Figure 2.2. The solid line represents the exact solution to (2.13) at $t = 1.0$. The circles depict the approximate solution coming from (2.15).

While the results above do not contradict the results from Theorem 1, they should however be considered unsatisfactory. To eliminate this staircase phenomena, (this phenomena is inherent to our modified forward Euler central schemes), we introduce a Lax-Wendroff type of viscosity to the right hand side of (2.14). Specifically, we modify (2.14) to

$$u_j^{n+1} = u_j^n - \frac{\Delta t}{\Delta x}((v_{j+1/2}^l - S_{j+1/2}) - (v_{j-1/2}^l - S_{j-1/2})), \tag{2.15}$$

where

$$S_{j+1/2} = \frac{1}{2}\left(\frac{\Delta t}{\Delta x}\right)\frac{v_{j+1/2}^l - u_j^n}{u_j^n - v_{j-1/2}^r}\left(v_{j+1/2}^l - v_{j-1/2}^r\right).$$

This modification leads to a scheme that is generically fourth order in space and *second* order in time. More importantly however, in regions where the solution to the pde is smooth, (2.15) reduces to a stable numerical scheme. The results from (2.15) are plotted in figure 2.2. Implicit schemes of the form (2.8) do not exhibit the staircase phenomena demonstrated above for explicit schemes. The viscosity modification hinted to above in (2.15) will be analyzed and generalized in future work.

§3. Hyperbolic systems and numerical examples. The extension of the implicit scheme (2.8) to hyperbolic systems is straight-forward. Numerical results coming from the implicit scheme applied to hypersonic reentry problems will appear in a future paper with C. P. Li of NASA Johnson Space Center. The extension of the modified explicit scheme (2.6) to time dependent hyperbolic systems is not so straight-forward. As demonstrated in the examples depicted in figures 2.1 and 2.2, some type of numerical viscosity must be appended to the basic central scheme. At present, we take the approach outlined below.

Consider a one space dimensional, hyperbolic system of m equations

$$\frac{\partial}{\partial t}u + \frac{\partial}{\partial x}f(u) = 0, \tag{3.1}$$
$$u \in \mathbf{R}^m,\ f : \mathbf{R}^m \to \mathbf{R}^m,$$

and let $Df(u)$ denote the Jacobian matrix of $f(u)$. Since (3.1) is hyperbolic, the matrix $Df(u)$ has m real eigenvalues, denoted here by $\lambda_k(u)$, $k = 1,\ldots,m$ and m independent eigenvectors, denoted here by $r_k(u)$, $k = 1,\ldots,m$. We let $R(u)$ denote the matrix whose columns are the right eigenvectors of $Df(u)$,

$$R(u) = \left(r_1(u) \quad \cdots \quad r_m(u)\right),$$

and

$$L(u) = R^{-1}(u).$$

The domain and range of the minmod function is extended to $\mathbf{R}^m$ component-wise. That is, for each $1 \le i \le m$

$$(\text{minmod}(\vec{x},\vec{y}))_i = \text{minmod}(x_i, y_i).$$

The modification of (2.4) to systems is to perform the limiting in so-called *characteristic variables*. Written in matrix form, this procedure is given by

$$\vec{v}^l_{j+1/2} = \vec{u}^n_j + R(u^n_j)\ \text{minmod}(L(u^n_j)\widehat{u_R}^n_j, \rho L(u^n_j)\widehat{u_L}^n_j), \tag{3.2}$$
$$\vec{v}^r_{j+1/2} = \vec{u}^n_{j+1} + R(u^n_{j+1})\ \text{minmod}(L(u^n_{j+1})\widehat{u_L}^n_{j+1}, \rho L(u^n_{j+1})\widehat{u_R}^n_{j+1}),$$

The simplest numerical flux $h_f(u_1,u_2)$ we can envision (see (2.6)) is the Lax-Friedichs numerical flux function. It is given by

$$h^{LF}_f(u_1,u_2) = \frac{1}{2}\left((f(u_1) + f(u_2)) - \nu(u_1 - u_2)\right), \tag{3.3}$$

where the parameter ν is an artificial viscosity satisfying

$$\nu \ge \max_k(\max(|\lambda_k(u_1)|, |\lambda_k(u_2)|)).$$

Since generically we will have that $u_1 = u_2$, the Lax-Friedrichs viscosity term above will vanish so that generically we will have that

$$h^{LF}_f(u_1,u_2) = f(u_1) = f(u_2).$$

Finally, the viscosity modification used in (2.15) will be extended to nonlinear systems of equations in the following way. Define $\widehat{c_L}_j$ and $\widehat{c_R}_j$ by

$$\widehat{c_L}_j = \text{minmod}(L(u^n_j)\widehat{u_L}^n_j, \rho L(u^n_j)\widehat{u_R}^n_j), \tag{3.4}$$

$$\widehat{c_R}_j = \text{minmod}(L(u_j^n)\widehat{u_R}_j^n, \rho L(u_j^n)\widehat{u_L}_j^n),$$

and from these define

$$s_{Lj} = -(\widehat{c_R}_j - \widehat{c_L}_j)\left(\widehat{c_L}_j/\widehat{c_R}_j\right),$$
$$s_{Rj} = -(\widehat{c_R}_j - \widehat{c_L}_j)\left(\widehat{c_R}_j/\widehat{c_L}_j\right),$$

Note that both s_{Lj} and s_{Rj} are well defined and continuous functions of $\widehat{u_L}_j^n$ and $\widehat{u_R}_j^n$. Now in each cell j and for each vector component k, compute

$$(d_{Lj})_k = 1/2\frac{\Delta t}{\Delta x}\min(\lambda_k(u_j),0)^2(s_{Lj})_k, \tag{3.5}$$
$$(d_{Rj})_k = 1/2\frac{\Delta t}{\Delta x}\max(\lambda_k(u_j),0)^2(s_{Rj})_k.$$

The full numerical flux function we use in our forward Euler calculations below is given by

$$h_{f_{j+1/2}} = h_j^{LF}(\vec{v}_{j+1/2}^r, \vec{v}_{j+1/2}^l) - \left(R(u_{j+1}^n)d_{Lj+1} + R(u_j^n)d_{Rj}\right), \tag{3.6}$$

giving the scheme

$$u_j^{n+1} = u_j^n - \frac{\Delta t}{\Delta x}\left(h_{f_{j+1/2}} - h_{f_{j-1/2}}\right).$$

We consider the fourth order modified central scheme (3.6) taking the limit factor $\rho = 3.0$ and using a Courant number $CFL = 0.25$. This scheme is applied to the one dimensional Euler equations

$$\frac{\partial}{\partial t}\rho + \frac{\partial}{\partial x}\rho u = 0,$$
$$\frac{\partial}{\partial t}\rho u + \frac{\partial}{\partial x}(\rho u^2 + p) = 0,$$
$$\frac{\partial}{\partial t}e + \frac{\partial}{\partial x}(e+p)u = 0.$$

In the equations above, ρ is a fluid's density, u its velocity and e its total energy. The pressure p is given by the equation of state $p = (\gamma - 1)(e - \rho u^2)$ where the parameter $\gamma = 1.4$. The Riemann problem initial datum

$$(\rho(x), u(x), p(x)) = \begin{cases} (.445, .698, 3.528) & \text{if } x < 0.5 \\ (.5, 0, .571) & \text{if } x \geq 0.5 \end{cases},$$

defines what is frequently referred to as the Lax Riemann problem. This datum is integrated to time $t = 0.15$. See [7,2,6] for comparisons. 100 equally spaced points on the interval $(0,1)$ are used for all results presented here. In all figures below, the solid lines represent the exact fluid density and the $x's$ denote its numerical approximation.

Figure 3.1 depicts the results of the second order Lax-Wendroff finite difference scheme applied to the Lax Riemann test problem above with $CFL = 0.8$. Figure 3.2 depicts the results of the first order Lax-Friedrichs finite difference scheme applied to this same test problem. Figure 3.3 depicts our new scheme (3.6) applied to the Lax test problem.

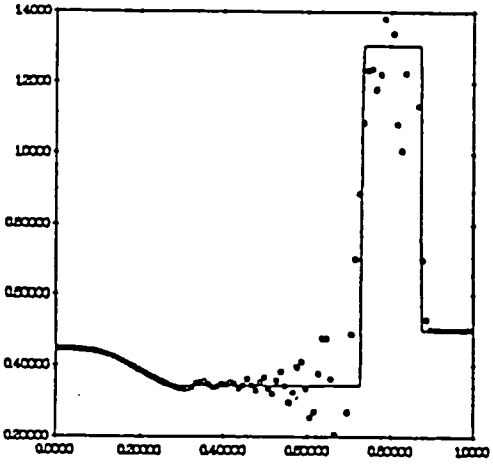

Figure 3.1. The solid line represents the exact solution to the Lax Riemann problem. The $x's$ are results from the Lax-Wendroff scheme.

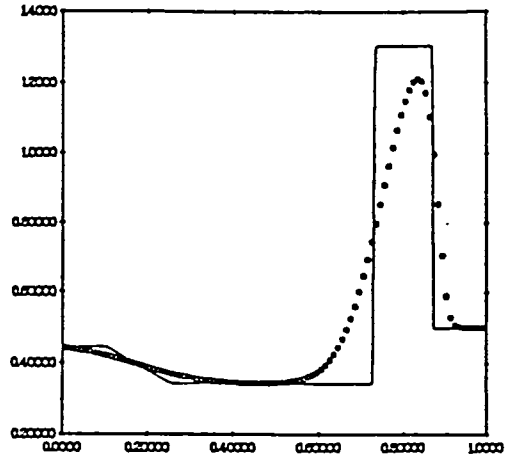

Figure 3.2. Results coming from the Lax-Friedrichs scheme.

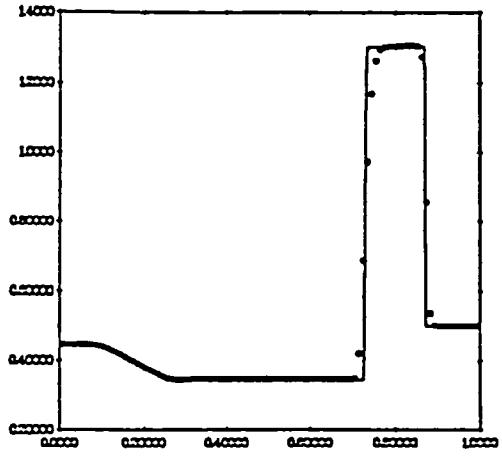

Figure 3.3. Numerical results coming from our fourth order scheme (3.6).

The next test problem is referred to as the *blast wave* problem. This problem tests the performance of a numerical scheme on very strong shocks and shock wave interactions.

Its initial data contains two shock waves with pressure ratios of 100,000 and 10,000. The initial data to this problem is

$$(\rho(x), u(x), p(x)) = \begin{cases} (1.0, 0.0, 1000.0) & \text{if } x < 0.1 \\ (1.0, 0.0, 0.01) & \text{if } 0.1 \leq x \leq 0.9 \\ (1.0, 0.0, 100.0) & \text{if } x > 0.9 \end{cases},$$

The boundary conditions at $x = 0$ and $x = 1$ are reflecting. The Lax-Wendroff scheme will not solve this problem. The initial shocks are so strong that negative densities and pressures occur almost immediately. The Lax-Friedrichs scheme will solve it – be it not very well. Figure 3.4 depicts the Lax-Friedrichs results using 400 points comparing it to the "exact" solution which came from (3.6) using 1200 points. (The exact solution to this problem can not be found in closed form.) Figure 3.5 demonstrates the performance of our scheme (3.6) on the blast wave test problem again using 400 points. We should point out that no modifications of the scheme was required to avoid negative densities and pressures.

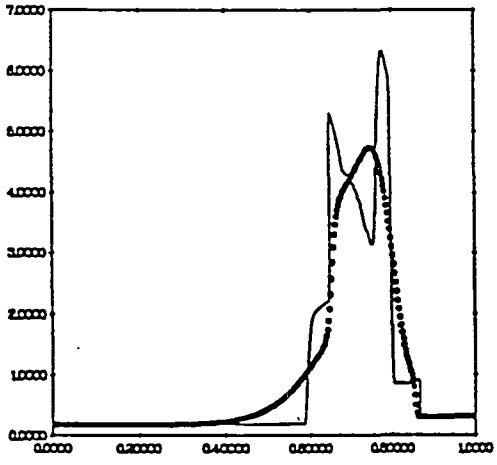

Figure 3.4. The Lax-Friedrichs scheme applied to the blast wave test problem.

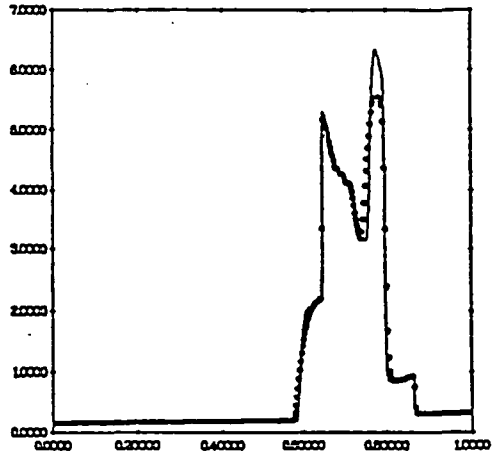

Figure 3.5. Results coming from scheme (3.6).

References

[1] N. Dunford and J.T. Schwartz, *Linear Operators, Part I: General Theory*, Pure and Appl. Math., vol VII, Interscience, New York, 1958.

[2] A. Harten and S. Osher, "Uniformly high-order accurate nonoscillatory schemes. I", *SIAM J. Numer. Anal.* 24 (1987), pp. 279-309.

[3] P. D. Lax, "Weak solutions of nonlinear hyperbolic equations and their numerical computation", *Comm. Pure Appl. Math.* 7, pp. 159-193.

[4] R. Sanders, "On convergence of monotone finite difference schemes with variable spatial differencing", *Math. Comp.* 40 (1983) pp. 91-106.

[5] R. Sanders, "A third order accurate variation nonexpansive difference scheme for single nonlinear conservation laws", *Math. Comp.* 51 (1988) pp. 535-558.

[6] R. Sanders and A. Weiser, "A high order staggered grid method for hyperbolic systems of conservation laws in one space dimension", *Computer Methods in Applied Mechanics and Engineering.* 75 (1989) pp. 91-107.

[7] G.A. Sod, "A survey of several finite difference methods for systems of nonlinear hyperbolic conservation laws", *J. Comp. Phys.* 27 (1978), pp. 1-31.

THE DOUBLY LABELED WATER METHOD FOR MEASURING HUMAN ENERGY EXPENDITURE: ADAPTATIONS FOR SPACEFLIGHT

Final Report

NASA/ASEE Summer Faculty Fellowship Program--1991

Johnson Space Center

Prepared By:	Leslie O. Schulz, Ph.D.
Academic Rank:	Associate Professor
University & Department	University of Wisconsin-Milwaukee Department of Health Sciences Milwaukee, Wisconsin 53201
NASA/JSC	
Directorate:	Space and Life Sciences
Division:	Medical Sciences
Branch:	Biomedical Operations and Research
JSC Colleague:	Helen W. Lane, Ph.D.
Date Submitted:	August 15, 1991
Contract Number:	NGT-44-001-800

ABSTRACT

It is essential to determine human energy requirements in space and the doubly labeled water method has been identified as the most appropriate means of indirect calorimetry to meet this need. The method employs naturally occurring, stable isotopes of hydrogen (^2H, deuterium) and oxygen (^{18}O) which, after dosing, mix with body water. The deuterium is lost from the body as water while the ^{18}O is eliminated as both water and CO_2. The difference between the two isotope elimination rates is therefore a measure of CO_2 production and hence energy expenditure.

Spaceflight will present a unique challenge to the application of the doubly labeled water method. Specifically, interpretation of doubly labeled water results assumes that the natural abundance or "background" levels of the isotopes remain constant during the measurement interval. This assumption does not hold true during spaceflight since the potable water on board the Space Shuttle, which is produced as a byproduct of electricity by the fuel cells, varies within the mission with respect to enrichment levels of these isotopes. Therefore, interpretation of doubly labeled water results during future in-flight studies will be complicated by the changing background isotope enrichments due to consumption of Shuttle water.

To address this issue an equilibration model will be developed in an on-going ground-based study. As energy requirements of women matched to counterparts in the Astronauts Corps are being determined by doubly labeled water, the baseline isotope concentration will be changed by consumption of "simulated Shuttle water" which is artificially enriched. One group of subjects will be equilibrated on simulated Shuttle water prior to energy determinations by doubly labeled water while the others will consume simulated Shuttle water after dosing. This process will allow us to derive a prediction equation to mathematically model the effect of changing background isotope concentrations.

The results of this study will inform us whether or not it will be necessary to initially equilibrate astronauts involved in future in-flight doubly labeled water studies with Shuttle water to prevent compromising interpretation of energy expenditure data. Since prior equilibration would be logistically difficult to accomplish, a mathematical model would significantly ease the technology involved in addressing the critical issue of human energy requirements in space.

INTRODUCTION

It is essential to determine human energy requirements in space to adequately assess food needs for long-term missions and to be able to predict energy requirements in closed ecological life support systems. The doubly-labeled water method has been identified by NASA as the most appropriate means of indirect calorimetry to meet this need. The method employs naturally occurring, stable isotopes of hydrogen (^2H, deuterium) and oxygen (^{18}O) which, after dosing, mix with the body water. Due to the action of the enzyme carbonic anhydrase, primarily in red blood cells, the isotopes equilibrate between water and carbon dioxide. The deuterium is then lost from the body as water while the ^{18}O is eliminated as both water and CO_2. The difference between the two isotope elimination rates, determined from urine or saliva samples prepared for gas isotope ratio mass spectrometry, is therefore a measure of CO_2 production and hence energy expenditure.

The doubly labeled water method is considered a major advance in nutrition research because it allows for the quantification of energy expenditure in free-living populations for a period of days to weeks. There have already been many interesting applications of the method to address basic questions in nutrition science. For example, it has been applied to quantifying energy expenditure of people throughout the life cycle (1), including pregnant and lactating women (2). The doubly labeled water method has also been used to assess the energy cost of various work and exercise patterns (3) and in people in different environmental conditions (4). Given its potential use in such a variety of circumstances, it is essential to also understand its limitations. A number of investigators have probed the assumptions underlying the method to identify the conditions under which its validity and/or precision may be impaired and to develop the most accurate approaches to data analysis. The assumptions that underpin the doubly labeled water method include the following (5,6):

1. Body water is a single compartment that the isotopes (^2H and ^{18}O in H_2O) label and from which they are lost.

2. ^2H is lost only as water.

3. ^{18}O is lost both as water and as carbon dioxide; transference of oxygen between water and carbon dioxide is the consequence of a rapid exchange promoted by carbonic anhydrase.

4. Total body water, and output rates of water and carbon dioxide are constant.

5. Water and carbon dioxide losses occur with the same enrichment as that coexisting in body water.

6. Background isotope intake rates are constant.

In truth, none of these assumptions is absolute (5,6). Therefore, it is necessary to understand the significance of each of the model's imperfections in order to make the necessary corrections. This report will deal specifically with assumption number 6 because it is uniquely affected by space travel. Background concentrations of ^{2}H and ^{18}O are important considerations because in order to obtain data to calculate CO_2 production, the baseline value is subtracted from the post-dose enrichments. If the baseline value changes throughout the isotope disappearance curve and is unaccounted for, an error will be introduced into the final calculation.

Since stable isotopes occur naturally, they are in everything we eat, drink and breathe. Individuals thus take on a pattern of isotope enrichment that reflects their intake. With respect to ^{2}H and ^{18}O, the usual source of variation is brought about by evaporation and condensation processes where isotopic enrichment in humans follows the same pattern as that seen for water supplies, and ^{2}H and ^{18}O enrichments covary. There are several situations which have been shown to lead to changes in background enrichments. An obvious example would be a subject moving from one location to another and thereby changing his or her background intake. In addition, infants who are breastfed are more enriched than those who are bottle-fed (7); presumably at weaning breastfed babies become less enriched. Gambian infants have been found to have significant background variations at different times of the year (6). Finally, Jones et al. (8) have shown the effect of changing nutrition on background enrichments in infants weaned from total parenteral nutrition.

Spaceflight presents a new challenge for the doubly labeled water method, in particular for developing a systematic approach to dealing with changing background isotope enrichments. Currently, during spaceflight, the water which is consumed on board the Shuttle is produced as a byproduct of electricity by the fuel cells. The water varies within the mission with respect to enrichment levels of ^{2}H and ^{18}O. Therefore, interpretation of doubly labeled water data from inflight studies will be complicated by the changing background isotope enrichments due to consumption of Shuttle water. The study described below has been designed to address this issue.

PROCEDURES

The intent of the on-going project is two-fold: 1) to use the doubly labeled water method to determine energy requirements in lean, active women in the same age range as those in the Astronaut Corps, and 2) to alter conditions in this ground-based study to take into consideration changes in background isotope enrichment which will be involved in-flight due to consumption of Shuttle water.

A total of twelve women between the ages of 35 and 50, judged to be healthy by an Air Force Class 3 physical examination, will participate in the study. Weighed food records are being obtained throughout the study and exercise tests for maximal oxygen uptake and strength indicators are conducted at regular intervals. Body composition is assessed by skinfolds, underwater weighing, and bone densitometry. Resting energy expenditure is determined with a metabolic cart and canopy at the beginning and end of the doubly labeled water measurement of total energy expenditure.

The women are randomly assigned to two groups; group A has a changing baseline and group B has a stable baseline with respect to ^{2}H and ^{18}O. The baseline values are being manipulated by means of "simulated Shuttle water" which is intentionally enriched with the two heavy isotopes. Each subject obtains simulated Shuttle water from the Johnson Space Center and uses it for all food preparation and consumption throughout the energy expenditure assessment period. Women in group A are dosed with doubly labeled water simultaneously with initiation of consumption of simulated Shuttle water and therefore have a known change in the background enrichment of ^{2}H and ^{18}O. Women in group B consume simulated Shuttle water for two weeks prior to dosing with doubly labeled water. Urine samples are collected in this group both before and after dosing to quantify the change in baseline.

INTERPRETATION OF RESULTS

The data collected from the doubly labeled water procedure will be analyzed to determine total energy expenditure (TEE) for active women in this age range. The physical activity level (PAL) will also be assessed by dividing the TEE by resting energy expenditure (REE) measured by metabolic cart. This index (PAL=TEE/REE) is being increasingly used because it allows immediate comparison between subjects of different ages, sex, and body size, since the influence of these variables is largely removed by using REE as the denominator.

To address the issue of changing background enrichments, an equilibration model will be developed. Three factors will be considered to derive a prediction equation to mathematically model the effect of changing background isotope concentrations: the difference between measured baseline isotopic abundance and the predicted baseline on Shuttle water, the time interval of re-equilibration to the Shuttle water, and the fraction of water derived from the dietary source.

SIGNIFICANCE

The results of this study will provide important information on energy requirements of women aged 35 to 50. Data on normal, active women in this age group have been previously lacking. Since women represent an increasing proportion of the Astronaut Corps, these data will fill a void and improve estimates of food and oxygen needs for future flights.

The results of this study will also inform us whether or not it will be necessary to initially equilibrate astronauts involved in future in-flight doubly labeled water studies with Shuttle water to prevent compromising interpretation of energy expenditure data. Since prior equilibration would be logistically difficult to accomplish, a mathematical model would significantly ease the technology involved in addressing the critical issue of human energy requirements in space.

REFERENCES

1. Roberts, S.B., Coward, W.A., Lucas, A. (1987) Validation of the doubly labelled water method in preterm infants. Am. J. Clin. Nutr. 45, 1545-1547.

2. Lawrence, M., Lawrence, F., Coward, W.A., Cole, T.J., Whitehead, R.G. (1987) Energy requirements of pregnancy in The Gambia. Lancet 2, 1072-1076.

3. Schulz, L.O., Alger, S., Harper, I., Wilmore, J.H., Ravussin, E. Energy expenditure of elite female runners measured by respiratory chamber and doubly labeled water. J. Appl. Physiol. (in press).

4. Singh, J., Prentice, A.M., Diaz, E., Coward, W.A., Ashford, J., Sawyer, M., Whitehead, R.G. (1989) Energy expenditure of Gambian women during peak agricultural activity measured by the doubly-labelled water method. Br. J. Nutr. 62, 315-329.

5. Schoeller, D.A. (1988) Measurement of energy expenditure in free-living humans by using doubly labeled water. J. Nutr. 118, 1278-1289.

6. Coward, W.A., Cole, T.J. The doubly labeled water method for the measurement of energy expenditure in humans: risks and benefits in Whitehead, R.G. and Prentice, A. (eds.) New Techniques in Nutritional Research Academic Press: New York, 1991.

7. Roberts, S.B., Coward, W.A., Ewing, G., Savage, J., Cole, T.J., Lucas, A. (1988) The effect of weaning on the accuracy of the doubly-labelled water method in infants. Am. J. Physiol. 254, R622-627.

8. Jones, P.J.H., Winthrop, A.L., Schoeller, D.A., Filler, R.M., Swyer, P.R., Smith, J., Heim, T. (1988) Evaluation of doubly labeled water for measuring energy expenditure during changing nutrition. Am. J. Clin. Nutr. 47, 799-804.

MODEL OF THE FRICTIONAL HEATING OF INCONEL 718 AND TITANIUM (Ti-6Al-4V) IN HELIUM

Final Report

NASA/ASEE Summer Faculty Fellowship Program 1991

Johnson Space Center

Prepared by:	Christopher T. Skowlund, Ph.D.
Academic Rank:	Assistant Professor
University & Department:	New Mexico State University Chemical Engineering Department Las Cruces, New Mexico 88003
NASA/JSC	
Directorate:	Johnson Space Center
Division:	White Sands Test Facility
Branch:	Laboratories Office
JSC Colleague:	Harold D. Beeson, Ph.D.
Date Submitted:	August 9, 1991
Contract Number:	NGT-44-001-800

ABSTRACT

The frictional heating of metals in sliding contact in an oxygen-rich environment can result in the catastrophic ignition and combustion of metallic parts. In order to investigate the susceptibility of specific metals to this phenomenon the NASA White Sands Test Facility (WSTF) has conducted numerous experimental investigations of this phenomenon over the past decade using a unique apparatus developed at WSTF. A number of theoretical investigations of the frictional heating and subsequent ignition have also been pursued at WSTF. But, due to the complexity of the different phenomena involved in the frictional heating of metals in an oxygen-rich environment (e.g., the kinetics of the oxidation reactions or the effect of mechanical, physical and chemical changes at the interface on the actual amount of heat produced by friction) it is not possible at present to accurately predict whether the ignition phenomena will occur. The heat introduced to the interface of the samples during the experiment via friction will be balanced by the heat loss from the interface due to conduction through the samples away from the interface. This conduction of heat away from the interface will be enhanced by heat losses from the samples to the surroundings via convection, radiation and conduction. In order to accurately predict the possibility of ignition it is therefore important to understand the effect these phenomena have on the resulting temperature at the interface. It is also important to understand the actual heat produced by the frictional rubbing of the metallic samples. At present no quantitative theory exists for predicting the actual conversion of mechanical to thermal energy via friction (i.e., there is no method for predicting friction coefficients).

A computer model of the frictional heating of metals in an inert environment has been developed which incorporates the effects of the heat loss from the samples due to conduction, radiation and convection to the surroundings. This model allows the measured temperatures to be used to determine the amount of heat produced at the interface during the experiment by the sliding contact of two different metallic samples. The results of the simulation for an experiment run at WSTF show that for the same heat production at the interface the heat losses have a significant effect on the temperatures in the samples. But, the heat losses do not significantly affect the different calculated heat flows (or friction coefficients) at the interface necessary to correlate the measured temperatures.

INTRODUCTION

Over the past decade a number of theoretical and experimental reports have been published regarding the frictional heating of metals in gaseous oxygen,[1-5] the majority of which was conducted at the NASA White Sands Test Facility (WSTF). Jenny and Wyssmann[1] developed a theoretical model of frictional heating which incorporated conductive heat transfer along the sample and heat loss to the surroundings via radiation. They also assumed that the friction coefficient was dependent on the interface temperature, though they were unable to relate this temperature dependence to any physical property and instead relied on an empirical relationship.

At WSTF Yuen and co-workers[2-4] developed a number of models for the frictional heating apparatus. The model by Zhu et al.[3] incorporated conduction along the samples, convective and radiative heat loss and heat production due to oxidation reactions at the interface. Although the model used a number of empirical parameters it was able to qualitatively represent the experimental results.

The purpose of this modeling effort is to test a model of the frictional heating of cylinders under relatively simplistic conditions (i.e., no reaction). By removing the contribution to the heat input due to the oxidation reactions (which, at present, are not well understood mathematically) it should be possible to determine with higher accuracy the contributions of the other phenomena (friction, conduction, convection, etc.) on the observed temperatures in the samples.

EXPERIMENTAL RESULTS

The experimental results used in this study are from test number 830-411 performed on October 11, 1990 at WSTF. The experimental apparatus for the frictional heating tests has been described in detail elsewhere[5] and need not be repeated here. From a modeling standpoint we need only consider those aspects of the design and operation of the experiment which may have an effect on the observed results.

The test samples consist of two annular rods, one stationary (made of Inconel 718) and one rotating (made of the titanium alloy Ti-6Al-4V). Both samples are approximately 0.850 in. long with an outer diameter of approximately 1 in. and an inner diameter of 0.8 in. The stationary sample is placed in a holder which has a diameter approximately 0.0015 in. wider than the outer diameter of the sample and is 0.4 in. long. For

the rotating sample the holder has a diameter approximately 0.001 in. less than the inner diameter of the sample, is approximately 0.5 in. long and is connected to the inner rotating shaft. After 0.5 in. the inner shaft diameter is reduced to 0.57 in. for a length of 0.8 in. where it then reaches the minimum diameter of 0.37 in. Both samples are enclosed in a cylindrical chamber with a gas volume of 3 in^3 (total volume approximately 4.5 in^3) and surrounded by a replaceable copper sleeve with a diameter of 1.5 in. The length of the chamber is 2.5 in.

The measurements of interest in this study were the transient temperature changes measured by two thermocouples placed in the stationary sample. The two thermocouples were located 0.05 in. (TC-702) and 0.20 in. (TC-703) from the junction with the rotating rod. The thermocouple closest to the junction shows a very interesting temperature change. There are four distinct time intervals during the course of the experiment denoted by changes in the temperature of TC-702 (fast, slow, fast, slow).

MODEL DEVELOPMENT

The model to be used in this study will be a simple transient one-dimensional model for heat conduction. Due to the high temperatures involved, though, the temperature dependence of the physical properties will be included. Therefore, for each annular rod (i=1,2) we will have the following energy balance[6]

$$\rho_i C_{p,i} \frac{\partial T}{\partial t} = \frac{\partial}{\partial x} k_i \frac{\partial T}{\partial x} - Q_v - Q_c - Q_r$$

where ρ_i = the density of rod i, $C_{p,i}$ = the heat capacity of rod i, T = temperature in the rod, t = time, x = axial position in rod, k_i = the thermal conductivity of rod i, Q_v = the heat loss per unit rod volume due to convection, Q_c = the heat loss per unit rod volume due to conduction and Q_r = the heat loss per unit rod volume due to radiation.

The initial condition will be:

$$T = T_o \quad \text{for } -\infty < x < +\infty$$

The boundary conditions will be:

At x = 0:

$$-k_1 \frac{\partial T}{\partial x} + k_2 \frac{\partial T}{\partial x} = Q_F \qquad \text{and} \qquad T_{0+} = T_{0-}$$

where Q_F is the frictional energy flux at the interface.

At $|x| \rightarrow \infty$:

$$T = T_w$$

Frictional Energy:

The frictional energy flux Q_F is given by the equation

$$Q_F(t) = P(t)v(t)\mu(t) \qquad \text{in Btu/in}^2 \text{ sec.}$$

Although the applied pressure (P) and velocity (v) terms are measured quantities, the coefficient of friction (μ) is not measured. Due to the substantial frictional forces introduced in this experiment it is likely that this parameter will change over the course of the experiment. At present there is very little suitable theory describing how the coefficient of friction will change over the course of the experiment. A number of methods were attempted in order to develop a suitable fit of the data. The following correlations gave the best results.

Correlation A: The first model simply states that the frictional heat flux Q_F will be held constant over a specified time interval Δt_i, i.e.

$$Q_F = Q_{F,i} \qquad \text{for } t_i < t < t_i+\Delta t_i$$

The values for $Q_{F,i}$ will be determined by the best fit of the experimental data. From these values the average values for the friction coefficient can be calculated using the following analysis:

Define the "average" flux over a time interval t_i to $t_i+\Delta t_i$ as

$$Q_{F,i} = \frac{\int_{t_i}^{t_i+\Delta t_i} Q_F dt}{\int_{t_i}^{t_i+\Delta t_i} dt} = \frac{\int_{t_i}^{t_i+\Delta t_i} P(t)\, v(t)\, \mu(t)\, dt}{\int_{t_i}^{t_i+\Delta t_i} dt}$$

For this experiment P(t) varies linearly with time and v is constant. Letting P(t) = kt gives the average friction coefficient over the time interval as

$$\mu_i = \frac{2Q_{F,i}\Delta t_i}{kv[(t_i+\Delta t_i)^2 - t_i^2]}$$

Correlation B: The second model will hold the friction coefficient μ constant over the time interval Δt_i, i.e.

$$\mu = \mu_i \qquad \text{for } t_i < t < t_i+\Delta t_i$$

The frictional heat flux Q_F will then be calculated using this value for μ. The values for μ_i will be determined by the least-squares fit.

Effect of Gas on Frictional Heating:

For the gas phase (helium) we can develop the following energy balance (assuming the gas phase to be well-mixed):

$$m_g C_{p,g} \frac{dT_g}{dt} = 2\pi R_o \int h_v (T - T_g)\, dx - A_g h_v (T_g - T_w)$$

where m_g = the mass of gas in the system, $C_{p,g}$ = the heat capacity of the gas, h_v = convective heat transfer coefficient, T = the rod temperature (varies with position), T_g = the temperature of the gas, T_w = the chamber wall temperature, R_o = the outer rod radius and A_g = the area for heat transfer from the gas to the surrounding chamber.

External Heat Transfer From Rods:

Convection:

The heat loss from the rods due to convection can be described by the equation

$$Q_v = S_v h_{vi} (T - T_g)$$

where S_v = the surface area per unit rod volume available for convective heat transfer (= $2R_o/(R_o^2-R_i^2)$), R_i = the inner radius of the annulus and h_{vi} = the convective heat transfer coefficient for rod i.

For the stationary Inconel rod it will be assumed that, due to the high temperatures involved in the experiment, free convection will be the major mode of heat transfer by convection for the part of the rod exposed to the chamber. The heat transfer coefficient can be given by the correlation from Chapman[7].

For the rotating titanium rod forced convection was assumed to be the main mode of convective heat transfer. A correlation for heat transfer for an annulus with the inner cylinder

rotating is given by Maron and Cohen.[8]

Conduction:

For the heat transfer from the cylinders to the holders over the small distances (0.0015 and 0.001 in., respectively, for the Inconel and titanium samples) the heat loss due to conduction can be approximated by assuming a "pseudo" heat transfer coefficient h_c

$$Q_c = S_{c,i}h_c(T - T_w) = \frac{S_{c,i}k_g}{\Delta x}(T - T_w)$$

where $S_{c,i}$ = the surface area per unit volume of rod i available for conductive heat transfer, k_g = the thermal conductivity of the gas (helium) evaluated at the average temperature of T and T_w and Δx = the distance separating the cylinder and holder.

Radiation:

The heat loss due to radiative heat transfer can be calculated via

$$Q_r = S_{r,i}\sigma F_{i-j}(T^4 - T_w^4)$$

where all temperatures are absolute (°R), σ = Stefan's constant (= 3.3063×10^{-15} Btu/s in^2 °R^4), $S_{r,i}$ = the surface area per unit volume of rod i available for radiative heat transfer and F_{i-j} = the shape factor for radiative heat transfer from body i to body j.

Due to the geometry of the apparatus, the shape factors are dependent on the axial position x. It is assumed that radiation will occur in both directions from the rods (i.e., from the outer surface of the rods to the chamber and from the inner surface of the rods to the shaft). The equations for radiative heat transfer between two gray bodies is given by Chapman.[7]

NUMERICAL SOLUTION

The numerical solution of the differential equations describing the temperature profiles in the annular rods is accomplished using a finite-difference approximation for the spatial derivatives and integrating in time using the ODEPACK subroutine LSODE (allowing integration via Adam's or the implicit Gear's methods). The nonlinear least-squares program

for determining the frictional heating parameters was the MINPACK subroutine LMDIF1 which utilizes a finite-difference Jacobian.

For the finite-difference approximation the following equation was used for the conduction terms:

At $x = x_i$:

$$\frac{\partial}{\partial x} k_j \frac{\partial T}{\partial x} = \frac{k_{j,i+}(T_{j,i+1} - T_{j,i}) - k_{j,i-}(T_{j,i} - T_{j,i-1})}{h^2}$$

where h is the grid spacing. The subscript j refers to the rod (Inconel, j = 1, or titanium, j = 2). The subscript i refers to the axial position (the value of i increases with increasing distance from the junction of the rods for both values of j). The axial position x = 0 refers to the junction of the two rods and x > 0 refers to the Inconel rod while x < 0 refers to the titanium rod. The thermal conductivities will be evaluated at the temperatures at the mid-points between x_{i+1} and x_i (for $k_{1,i+}$) and x_i and x_{i-1} (for $k_{1,i-}$). These temperatures will be approximated using a second-order difference formula.

The finite-difference approximation for the boundary condition at x = 0 was handled in the following manner:

Using $O(h^2)$ approximations for the derivatives gives

$$-\frac{k_{1,0}(T_{1,1} - T_1^*)}{2h} + \frac{k_{2,0}(T_2^* - T_{2,1})}{2h} = Q_F$$

where T^*_1 is the temperature in the Inconel rod at an imaginary point located a distance h into the titanium rod. T^*_2 is a similar point for the titanium rod.

Since we assume that the temperature at x = 0 is the same for both the Inconel and titanium rods for all times, this implies that at x = 0 $\partial T/\partial t$ for both rods are equal. For these terms to be equal the conduction terms must also be equal. We can therefore set the finite-difference approximations at x = 0 for both rods equal to each other, i.e.

$$\frac{k_{1,0+}(T_{1,1} - T_0) - k_{1,0-}(T_0 - T_1^*)}{\rho_1 C_{p,1,0}} = \frac{k_{2,0-}(T_2^* - T_0) - k_{2,0+}(T_0 - T_{2,1})}{\rho_2 C_{p,2,0}}$$

where the subscript 0 refers to values at x = 0.

Solving the boundary condition for T^*_1 in terms of T^*_2 gives

$$T_1^* = T_{1,1} + \frac{2hQ_F + k_{2,0}(T_{2,1} - T_2^*)}{k_{1,0}}$$

Substituting this into the previous equation gives T^*_2 solely in terms of the other temperatures (which are all known at the previous time step). This value for T^*_2 can then be used in the transient equation for the titanium rod at x = 0. Unfortunately, since T^*_2 and T^*_1 are necessary in order to calculate the thermal conductivities, an iterative procedure is necessary to first approximate these temperatures, calculate the thermal conductivities and then check the values obtained using the approximate values (in practice only a few iterations were necessary for convergence). The initial guesses for T^*_2 and T^*_1 were obtained using a second-order finite difference extrapolation.

The integration for the energy balance on the gas was accomplished using the trapezoidal rule.

RESULTS AND DISCUSSION

Figure 1 shows the results of the simulation with the frictional heat at the interface approximated using correlation A with 16 equally spaced values for $Q_{F,i}$. The agreement with the experimental results is within a relative error of 6%. Note that the calculated temperature at the interface approaches the phase transition temperature for Ti-6Al-4V (which is between 1750 and 1850°F). But, for the short period that the interface temperature enters this range the value is due primarily to difficulties in fitting the experimental data with the transient model. Except for this short interval the calculated interface temperature never enters this range. The effect of the phase transition on the energy balance was therefore neglected.

The average friction coefficient using 16 time intervals (parameters) in correlation A or B is shown in Figure 2. The initially high value for the friction coefficient suggests a Coulomb-type relationship (i.e., as $P \rightarrow 0$ the frictional force approaches a finite non-zero value). The results compare favorably with the friction coefficients determined from torque measurements as reported by Zhu et al.[3] After the initial time period the qualitative nature of the curve also agrees with the conceptual model of Suh[9] regarding the contributions to the friction coefficient from adhesion, plowing and polishing.

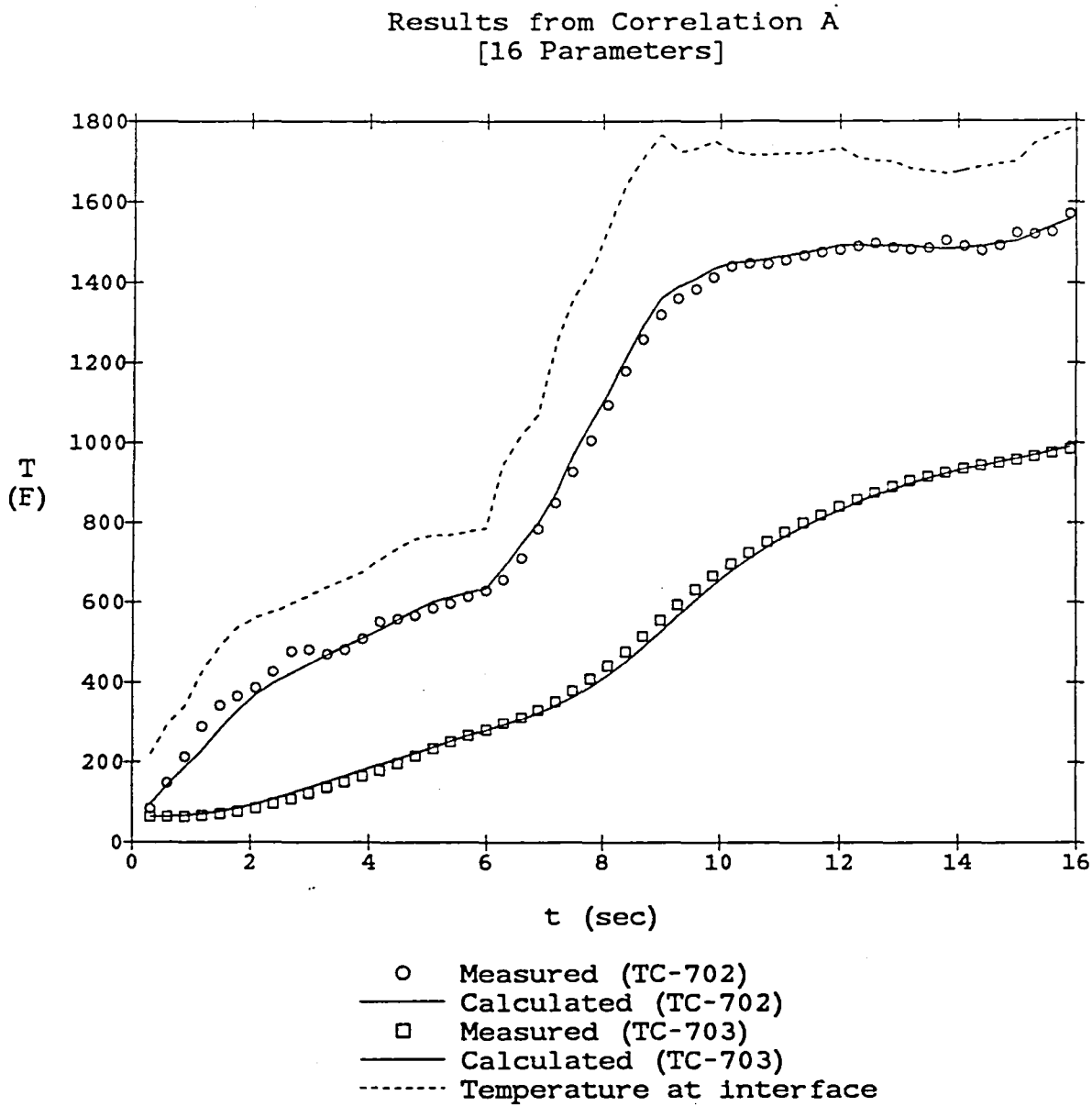

Figure 1.- Comparison of measured and calculated temperatures in Inconel 718 rod using correlation A with 16 time intervals.

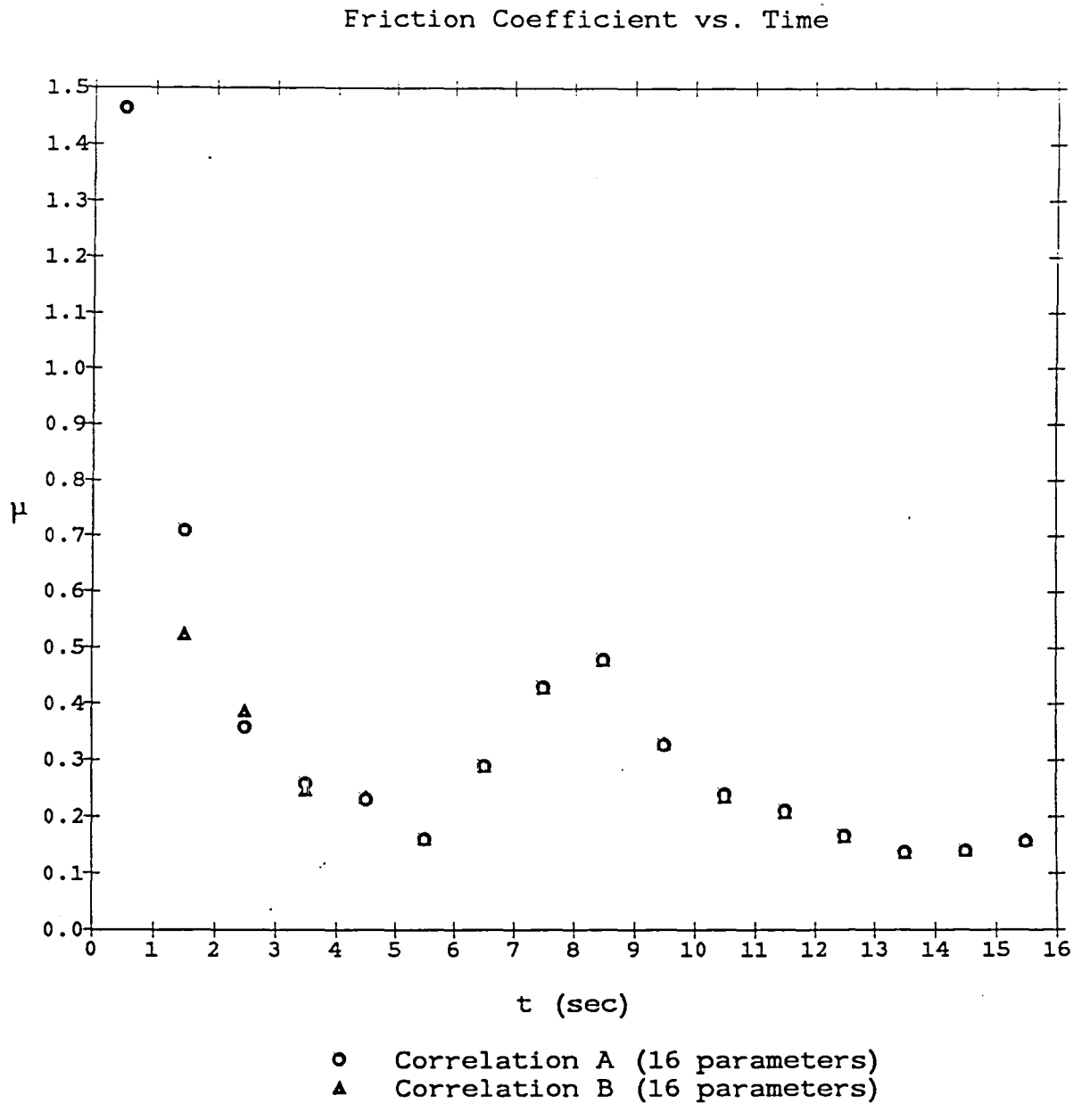

Figure 2.- Comparison of the average friction coefficients calculated using correlation A or B.

Figure 3 shows the contributions of conductive, radiative and convective heat loss on the calculated temperature profiles in the Inconel sample at the end of the simulation (for each curve the same values for the heat flux at the interface were used). For the stationary Inconel sample free convection and radiation make the largest contribution to the temperatures at the thermocouple positions (x = 0.05 in. and x = 0.2 in.).

For the rotating titanium sample forced convection contributes the most with conduction and radiation about equal. The large effect of conduction is due to the holder which extends from x = -0.85 to x = -0.35 in. This holder (which was assumed to remain at a constant temperature of 64°F) provides a significant sink for conductive heat transfer.

Figure 4 shows a comparison of the friction coefficients calculated using correlation A for two cases: 1) with the conductive, radiative and convective heat losses included and 2) with no heat losses included. These results, in conjunction with Figure 3, show the extreme sensitivity of the sample temperatures to the heat flux at the interface (i.e., the friction coefficients). In Figure 3 the values of the heat production corresponding to those used for case 1 (above) were used for all of the simulations, even those for which no heat losses were included (i.e., case 2). For the results in Figure 4 the values of the heat production required to match the measured temperatures were used for each simulation. From these results we can see that the required friction coefficients did not vary significantly between the two extreme cases. But, from Figure 3 we see that when the same values for the friction coefficient are used the temperatures at the thermocouple points (x = 0.05 in. and x = 0.20 in) vary by over one hundred degrees. This can be a significant difference when trying to predict the possibility of ignition for a given set of test conditions.

For the energy balance of the gas the final calculated temperature was 170°F which compares favorably with the measured value of 160°F.

The results of this research effort have shown that it is possible to accurately model the measured temperature in the metallic samples resulting from frictional heating in an inert environment. Future work will concentrate on attempting to extend the applicability of the model to reactive environments (i.e., gaseous oxygen) and the ability to separate the different contributions to the heat flux at the interface due to friction and reaction.

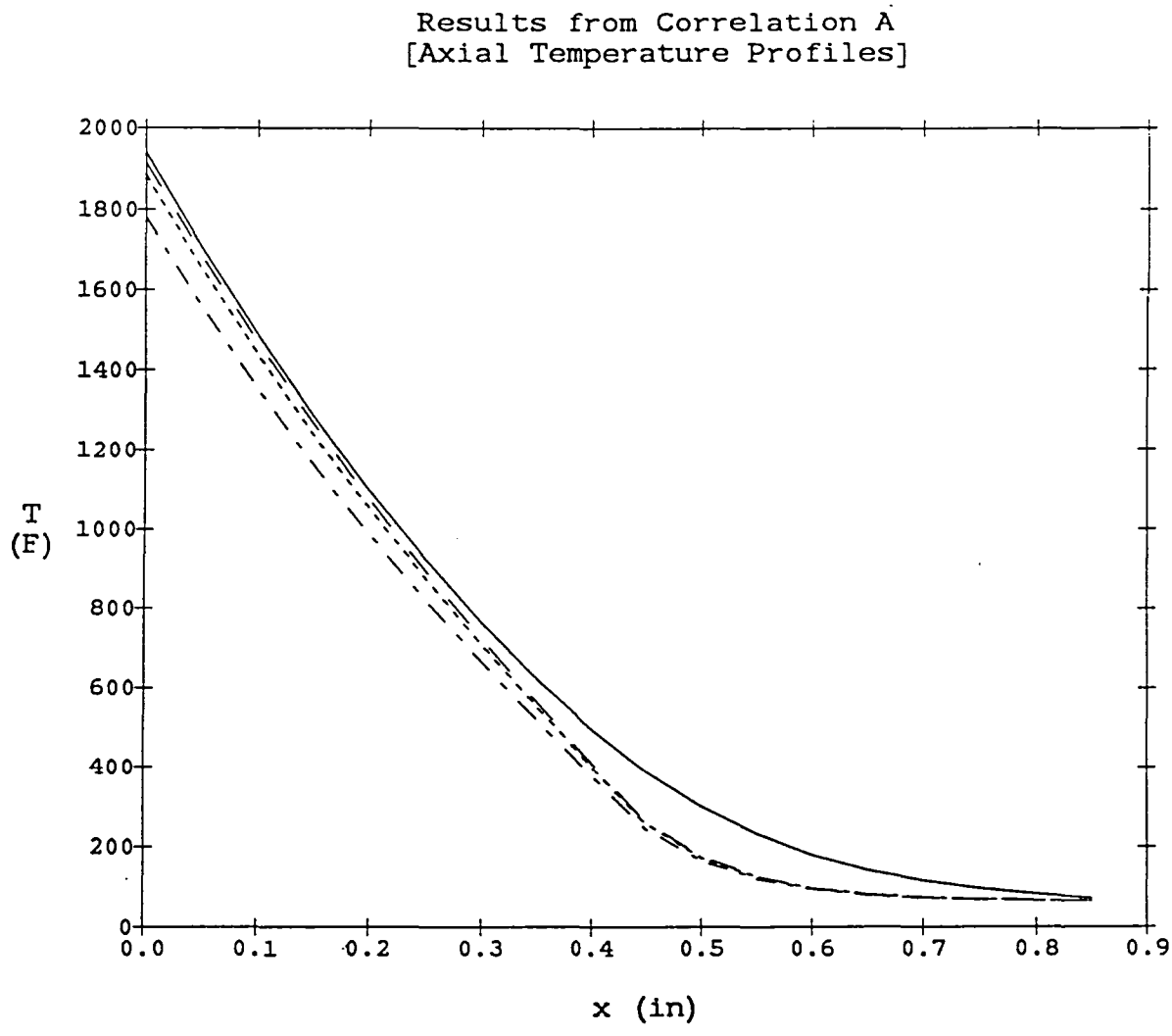

Figure 3.- Comparison of the effects of different modes of heat loss on the axial temperature profile in the Inconel 718 rod.

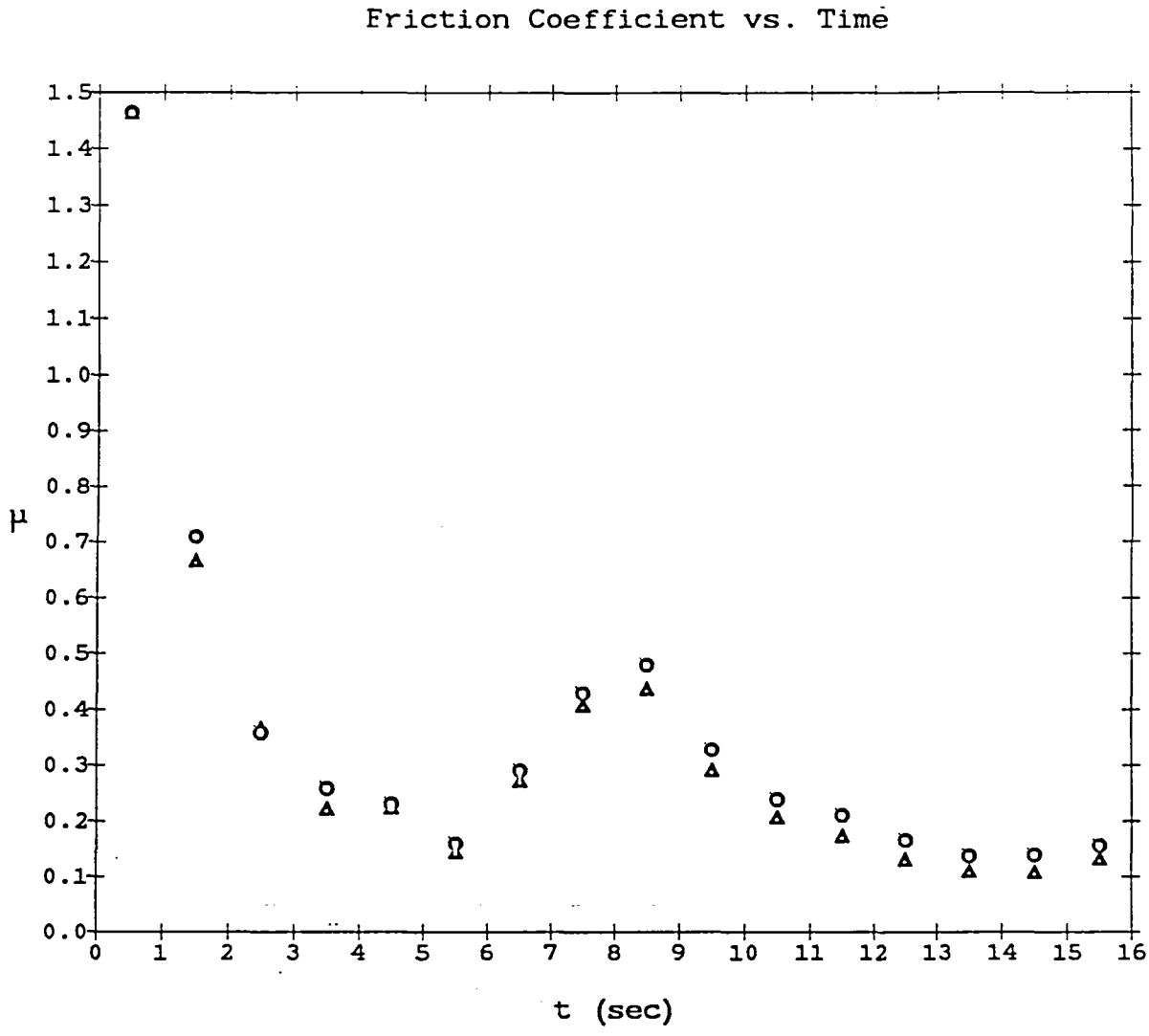

Figure 4.- Comparison of the average friction coefficients calculated using correlation A for two cases: 1) with all modes of heat loss from the sample included and 2) with no heat loss included.

REFERENCES

1. Jenny, R.; and Wyssmann, H.R.: Friction-Induced Ignition in Oxygen. Flammability and Sensitivity of Materials in Oxygen-Enriched Atmospheres (ASTM STP 812), B.L. Werley, ed., American Society for Testing and Materials (Philadelphia), 1983, pp. 150-166.

2. Yuen, W.W.: A Model of Metal Ignition Including the Effect of Oxide Generation. Flammability and Sensitivity of Materials in Oxygen-Enriched Atmospheres: 2nd Volume (ASTM STP 910), M.A. Benning, ed., American Society for Testing and Materials (Philadelphia), 1986, pp. 59-77.

3. Zhu, S.-H.; Stolzfus, J.M.; Benz, F.J.; and Yuen, W.W.: Modeling and Data Analysis of the NASA-WSTF Frictional Heating Apparatus: Effects of Test Parameters on Friction Coefficient. Flammability and Sensitivity of Materials in Oxygen-Enriched Atmospheres: 3rd Volume (ASTM STP 986), D.W. Schroll, ed., American Society for Testing and Materials (Philadelphia), 1988, pp. 172-187.

4. Yuen, W.W.: Modeling and Data Evaluation of the WSTF Frictional Heating Test Facility. Flammability and Sensitivity of Materials in Oxygen-Enriched Atmospheres: 4th Volume (ASTM STP 1040), J.M. Stolzfus, F.J. Benz and J.S. Stradling, eds., American Society for Testing and Materials (Philadelphia), 1989, pp. 76-90.

5. Stolzfus, J.M.; Benz, F.J.; and Homa, J.M.: The Pv Product Required for the Frictional Ignition of Alloys. Flammability and Sensitivity of Materials in Oxygen-Enriched Atmospheres: 4th Volume (ASTM STP 1040), J.M. Stolzfus, F.J. Benz and J.S. Stradling, eds., American Society for Testing and Materials (Philadelphia), 1989, pp. 212-223.

6. Carslaw, H.S.; and Jaeger, J.C.: Conduction of Heat in Solids. Oxford University Press, 1959.

7. Chapman, A.J.: Heat Transfer, 3rd Edition. Macmillan, 1974.

8. Maron, D.M.; and Cohen, S.: Hydrodynamics and Heat/Mass Transfer Near Rotating Surfaces, in *Advances in Heat Transfer*, vol. 21, 1991, pp. 141-183.

9. Suh, N.P.: Tribophysics. Prentice-Hall, 1986.

Movement of Trace Elements during Residence in the Antarctic Ice: A Laboratory Simulation

Final Report

NASA/ASEE Summer Faculty Fellowship Program - 1991

Johnson Space Center

Prepared By:	Melissa M. Strait, Ph. D.
Academic Rank:	Assistant Professor
University & Department	Alma College Department of Chemistry Alma, MI 48801
NASA/JSC	
Directorate:	Space and Life Sciences
Division:	Solar System Exploration
Branch:	Planetary Materials
JSC Colleague:	Marilyn M. Lindstrom, Ph.D.
Date Submitted:	November 12, 1991
Contract Number:	NGT-44-001-800

ABSTRACT

Thousands of meteorites have been found in Antarctica in recent years which represents a wealth of new material for meteorite research. While it has been recognized that meteorites returned from Antarctica have spent thousands of years buried in the ice and that this could have caused some weathering of the samples, only recently has serious attention been paid to the amount of weathering that may have occurred. From the early days of the Antarctic meteorite program, the curatorial process has given a simple weathering classification to recovered meteorites based primarily on visual observations. It was assumed that if a meteorite did not show obvious weathering, it must be relatively undisturbed chemically. However, recent work has determined that differences in the trace element distribution between Antarctic eucrites and non-Antarctic eucrites may be due to weathering during residence in the ice, and samples that demonstrate trace elements disturbances do not necessarily correspond to eucrites that appear badly weathered to the naked eye.

This study constitutes a preliminary test of the idea that long-term residence in the ice is the cause of the trace element disturbances observed in the eucrites. Samples of a non-Antarctic eucrite were leached in water at room temperature conditions. Liquid samples were analyzed for their rare earth element abundances using ion chromatography. The results for the short-term study showed little or no evidence of leaching having occurred. However, there were tantalizing hints that something may be happening.

The residual solid samples are currently being analyzed for the unleached trace metals using instrumental neutron activation analysis and should show evidence of disturbance if the chromatography clues were real. In addition, another set of samples continues to be intermittently sampled for later analysis.

The results should give us information about the movement of trace elements under our simulated conditions and allow us to make some tentative extrapolations to what we observe in actual Antarctic eucrite samples.

INTRODUCTION

In the past twenty years, a treasure trove of meteoritic material has become available with the discovery of thousands of meteorites in Antarctica. While it has been recognized that meteorites returned from Antarctica have spent thousands of years buried in the ice, and that this could have caused some alteration of the samples, only recently has serious attention been paid to weathering affects that may be present. Most of this work has concentrated upon the changes in mineralogy that result from weathering (Gooding, 1981; Velbel, 1988). The little work that has been directed toward changes in the overall chemistry of the meteorites were done on chondritic materials (Jovanovic and Reed, 1985).

Prior to 1969 about 2000 meteorites had been identified in the 250 years since meteorites were recognized to come from outside the Earth. Since 1969, approximately 12000 meteorite samples (many of which are paired samples of the same meteorite) have been recovered from the ice in Antarctica by teams of scientists sent from the US and Japan. Meteorites from Antarctica have extended the amount of material available on which to do meteorite research, as well as filled in gaps in existing suites of meteorites. In addition, new types of extraterrestrial material have been discovered, including meteorites that originate from a known source, such as the Moon.

Meteorites that are recovered from the ice have spent an average of about 230,000 years, but up to as long as 1,000,000, years immersed in the Antarctic icesheet (Schultz, 1990). Despite the low temperatures, it has come to be recognized that chemical reactions are occurring that alter the meteorites from their pristine state (Gooding, 1986). These meteorites must be carefully examined to look for the effects of weathering prior to using them in studies of their origin.

Studies of how materials weather in Antarctica were originally initiated to provide models for how materials may weather on Mars. These studies looked at basaltic weathering because it is proposed that the surface of Mars may be basaltic. Berkeley and Drake (1981) report in their study on an Antarctic Martian weathering analog that weathering in the Antarctic environment is extremely slow and inhibited by the lack of liquid water. In contrast, Conca and Wright (1987) found in laboratory simulations that etch pits and associated minerals observed in basaltic cobbles from Antarctica could form quickly during the short period of time when small amounts of liquid water were available during the austral summer.

The eucrite association (eucrites, howardites, diogenites and mesosiderites) represents an occurrence of planetary volcanism from the smaller bodies of the Solar System. This

meteorite association is studied to understand chemical and genetic relationships among the meteorite groups and to look at igneous processes that occurred 4.5 billion years ago in the Solar System.

The present study will look specifically at eucrites to examine the chemical effects of weathering and to further ongoing studies of asteroidal differentiation and early Solar System history. Of the approximately 4300 meteorite samples which have been returned from Antarctica by US scientists, about 80 have been classified as basaltic achondrites (Score and Lindstrom, 1990). This includes 56 samples of eucrites which represent approximately 28 meteorites.

Eucrites are generally breccias with remnant igneous textures that resemble terrestrial basalts and are modelled in an analogous manner. They consist of calcium-poor pyroxenes and calcium-rich plagioclases, in roughly equal amounts. In addition, the eucrites contain accessory amounts of olivine, tridymite, quartz, cristobalite, chromite, magnetite, ilmenite and phosphates, such as apatite and whitlockite, as well as minor amounts of metal and troilite (Duke and Silver, 1967).

As eucrites are basalts, the results of weathering studies of terrestrial basalts in Antarctica should apply to how eucrites weather in the Antarctic environment. Prior work with the Antarctic eucrites has led to the definition of two groupings based on the abundances of the REE: those with normal REE patterns (similar to REE patterns observed for eucrite falls), and those with abnormal patterns, mostly apparent enrichments in Ce and Eu (Mittlefehldt and Lindstrom, 1991). This is an important observation. The REE are used extensively to model igneous materials and abnormal abundances due to causes other than igneous processes must be carefully examined.

Mittlefehldt and Lindstrom (1991) proposed that the abnormalities observed in some Antarctic eucrites are caused by terrestrial weathering that occurs in the Antarctic ice. The primary REE minerals in the eucrites are the calcium phosphates. The phosphates are readily susceptible to dissolution in slightly acidic solutions. It was proposed that the phosphates dissolved during the residence of the meteorite in Antarctica. When the phosphates dissolve and the weathering solutions are removed from the meteorite, they carry with them a large part of the REE budget of the meteorite. Because Eu has been preferentially crystallized in the plagioclase, which is much less susceptible to alteration, Eu is retained in the meteorite. It is proposed that the Ce anomaly arises because it is oxidized to the +4 state by the acidic conditions that leach the apatite. Ce^{+4} forms an insoluble Ce oxide which precipitates and remains behind in the meteorite. Therefore, the abnormalities are

not enrichments of Ce and Eu, but depletions of the other REE.

This doesn't appear to happen in all cases. There are Antarctic eucrites with normal REE patterns that fall within the range of patterns exhibited by non-Antarctic eucrites. However, the presence of the abnormal Antarctic eucrites presents problems for workers who model the origins and evolution of the eucrites using REE data. Using abnormal eucrites may lead to erroneous conclusions in models.

There are two schools of thought as to causes of differences in the chemistry between Antarctic and non-Antarctic meteorites. (1) Differences are pre-terrestrial and are indicative of a change in the population of meteoritic material over time. (2) Differences are due to weathering during residence in the ice. A workshop was recently held to look at differences between Antarctic and non-Antarctic meteorites in an attempt to resolve this issue (Koeberl and Cassidy, 1991).

This study arises out of concerns for observed abundances of trace elements in eucrites. Early observations of inconsistencies in REE abundances in eucrites were made in Yamato eucrites in connection with dating studies involving the Hf/Lu system (Shimizu, et al., 1982; Tatsumoto, et al., 1981). More recently, Mittlefehldt and Lindstrom (1991) made an extensive study of Antarctic eucrites and found the two distinct populations. Strait (1990) looked for correlations between chemistry and visual evidence of weathering and found none. These latest studies have led to the current study because of the facility with which liquid and solid samples can be analyzed using the complementary techniques of ion chromatography (IC) and instrumental neutron activation analysis (INAA). The possibility that leaching during residence in the ice could be the cause of these disturbances is being examined in a laboratory simulation.

EXPERIMENTAL

In an attempt to understand apparent deviations in the trace element abundances of Antarctic eucrites we will be leaching non-Antarctic eucrites under conditions that we hope will promote the dissolution of phosphate minerals that are the primary REE carriers in the eucrites. At this point we have no intention of simulating actual Antarctic conditions. The chemistry of Antarctic ice will be used to establish the chemical environment of the study.

Studies of hydrothermal weathering of basalts at mid-ocean ridges conditions (high pressure and temperature in seawater(Seyfried and Mottl, 1982) were used to establish preliminary experimental conditions for this study.

Studies of weathering processes need to look at material that is known have been collected shortly after its fall to

earth (falls). The environmental conditions these meteorites have experienced is well documented. The record of available falls was examined and samples were chosen that represented extremes in a range of REE chemistries and were available in abundance. Four meteorites were initially selected. This preliminary study was done only using Stannern because of its availability.

Sample Preparation

A 6.5 g sample of Stannern was inspected and obvious altered portions were removed. In particular, the material along cracks that could provide entry for water into the stone was removed. The sample was split, and processed into a variety of sample forms: powdered, whole rock chips and a basaltic clast. Meteorites in the Antarctic environment would be present as whole rocks, however, to speed up any potential leaching of the phosphates, we have chosen to analyze powdered samples as well as small, whole chips.

The samples were prepared in the clean room facility of the INAA lab at Johnson Space Center. A comparison blank was prepared using crushed suprasil glass. In addition, plain water was subjected to the same conditions to control for possible contamination from outside sources, such as sample handling. The samples prepared are summarized in Table 1. Sample material not used in the leaching study was saved for later analysis by INAA and SEM.

Low density polyethylene (LDPE) bottles were used for the leach runs and for storage of the samples taken for IC analysis. LDPE plastic was chosen because it is low in potential trace element contamination. All bottles were cleaned by immersion for 2 days in hot 6 M HNO_3, rinsed in triply distilled water and allowed to air dry.

Antarctic ice is apparently relatively clean, with levels of major elements (Na, K, Ca, Fe, Mg, etc.), on the order of 10^{-9} to 10^{-12} g/g ((Boutron, 1980; Miklishanskiy, et al., 1980), so distilled water was used as the Antarctic melt water simulant. The water in contact with the eucrites in the Antarctic environment would have been weakly acidic due to equilibration with CO_2, NO_x, and SO_x present in the Antarctic atmosphere (Jovanovic and Reed, 1985). It is thought the slightly acidic conditions would oxidize sulfides in the eucrite to sulfuric acid, providing localized strongly acidic conditions. Therefore, water used for the experiment was allowed to equilibrate with the atmosphere for several days. The pH was determined to be ~5 (slightly acidic) at the time the study was commenced.

Approximately one gram samples of Stannern were placed in 60-mL LDPE screw cap bottles. About 50 mL of the equilibrated triply distilled water was added to each bottle.

TABLE 1. - STANNERN SAMPLE SUMMARY

Number	Weight (g)	Sample	Study Time
1	1.19636	Glass	30 Day
2	1.23035	Glass	Long-term
3	1.26042	Glass	Long-term/Unsampled
4	-	Water	30 Day
5	-	Water	Long-term
6	-	Water	Long-term/Unsampled
7	0.85012	Powder	30 Day
8	1.13482	Powder	Long-term
9	0.89999	Powder	Long-term/Unsampled
10	0.33566	Basalt Clast	Long-term
11	0.92267	Chip	30 Day
12	0.88286	Chip	Long-term

TABLE 2. - SAMPLE SCHEDULE TIMES IN HOURS AFTER START

Number	A	B	C	D	E	F
1	1	24	96	260	526	1007
2	96	1007				
3						
4	1	24	96	260	526	1007
5	96	1007				
6						
7	1	24	96	260	526	1007
8	96	1007				
9						
10	96	1007				
11	1	24	96	260	526	1007
12	96	1007				

The bottle was tightly closed and allowed to sit at room temperature for a period of time. Two run-time intervals were established: 30 days, to allow for some immediate summertime results; and an as yet undefined longer time period - on the order of 3 months to a year or more. The length of time for the long-term study has been extended indefinitely on the basis of the preliminary results from the 30-day study.

Two-milliliter samples were removed at regular intervals from designated bottles and placed in 5-mL sample vials. A total of six samples were removed for each run. The sample was preserved with the addition of ~ two drops of ultra-pure HNO_3 per 2 mL sample. Finally, the vial was sealed with wax to allow for transportation to Michigan with minimal sample loss. A schedule for the samples already collected is shown in Table 2.

At the end of the study, the remaining liquid was decanted from the solid and transferred to a sample bottle and preserved as before. The solid was carefully dried, and a portion removed for neutron activation analysis. The remainder was saved for later work.

The liquid samples were returned to Alma College for analysis. The REE were determined using ion chromatography. Transition metals (Fe, Cu, Co, Mn, Pb, Ni, Zn, etc.) will be analyzed later, and the solid samples are in the process of being analyzed by INAA at JSC. Neutron activation analysis is being run on leached and unleached glass as a background monitor, leached and unleached powders and the leached chips. A portion of the remaining solid will be made into grain mounts at a future date and examined by SEM for mineral weathering products.

Analysis

The REE in the leach samples were analyzed by ion chromatography. A Dionex 4500i gradient pump system with a post column reactor and UV/Visible detector was used for the analysis The chromatographic output was analyzed by a Spectra Physics 4400 integrator.

The method used to separate the various RE elements is based upon their relative attraction for a resin based ion exchange column and an organic chelating agent. This analysis used a gradient analysis from 80% 100 mM oxalic acid and 20% water to 26% 100 mM oxalic acid/23% 100 mM diglycolic acid/51% water over 8 minutes and then isocratic at the latter composition for another 12 minutes. Post column reaction with 4-(2-pyridylazo)resorcinol was used with photometric detection at 520 nm. The eluants were prepared from Fluka puriss quality reagents and 18 MΩ water. All

samples and reagents were filtered through a 0.45 μm filter before analysis.

A typical run showing the separation of 13 REE in a standard solution is shown in Figure 1. The retention times are reproducible between runs on any one day and are predictably reproduced from day to day. The concentrations for the standard on the calibrated system were within ±5% of the true value, with the exception of La, which was 40% low. Er, Yb and Lu are observable as peaks in the chromatogram, but are not processed by the integrator.

Figure 2 shows a typical calibration of the standard used to calibrate the system. This shows that the system is capable of reproducing concentrations from run to run, and demonstrates that the detection limit for the system is well below the 10 ppm level of the standard. The calibration is done with a standard prepared by dilution from 1000 ppm atomic absorption lanthanide standards (Aldrich Chemical).to 10 ppm levels.

Sample chromatograms for two of the samples are shown in Figure 3. All of the samples exhibited basically the same pattern, showing no real evidence of leaching having occurred. The samples show no presence of the REE in any sample other than a possible La peak (a retention time of 4-5 minutes) and possibly something in the range of Pr or Nd (a retention time of 6-8 minutes). Most samples that show the possible La peak. The peak is occasionally ~85%, and usually ~95% of the retention time for La. Only 12A, 7C and 7D show the peak in the 6-8 minute range, and the retention time varies from 6.45 to 8.73, with 7D having an additional peak at 5.26 minutes.

One note about the above possibilities is the problems with reproducibility in the system when only one or two of the lanthanides are present. Several of the elements must be present for the column interactions to work properly. Therefore, no definite conclusions can be made about what was observed in these runs. At best, it can only be said that the lanthanides did not leach to any detectable amount in thirty days.

The solid samples remaining from the 30-day run (1, 4, 7, and 11) have been decanted from the liquid, dried and prepared for INAA. The first count set has been completed and seems to confirm the results from the IC: no depletion in the REE was observed. However, one sample showed a discolored area which may be the result of alteration due to the presence of the water. The sample will be examined in the SEM to determine this possibility.

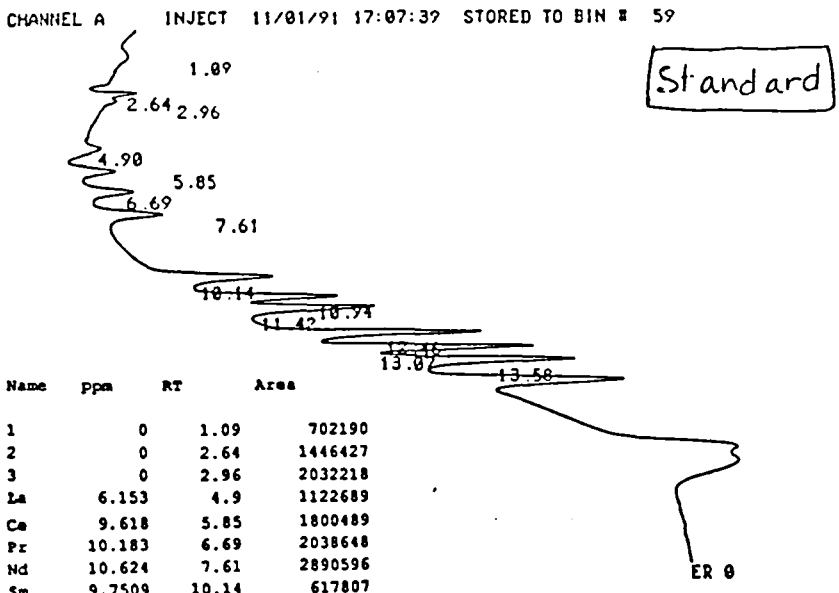

Name	ppm	RT	Area
1	0	1.09	702190
2	0	2.64	1446427
3	0	2.96	2032218
La	6.153	4.9	1122689
Ce	9.618	5.85	1800489
Pr	10.183	6.69	2038648
Nd	10.624	7.61	2890596
Sm	9.7509	10.14	617807
Eu	10.524	10.94	4598184
Gd	10.254	11.42	5620331
Tb	10.635	12.46	5553819
Dy	10.079	13.07	5884729
Ho	10.455	13.58	6969844
Er		(14.3)	
Yb		(16.9)	
Lu		(17.57	

Figure 1.- A typical run of the standard showing the appearance of the 10 ppm standard. Retention times in parentheses are manually calculated. The peaks before ~5 minutes are injection peaks, an artifact of the sample injection. The curve in the baseline is due to the gradient analysis. (RT = retention time in minutes)

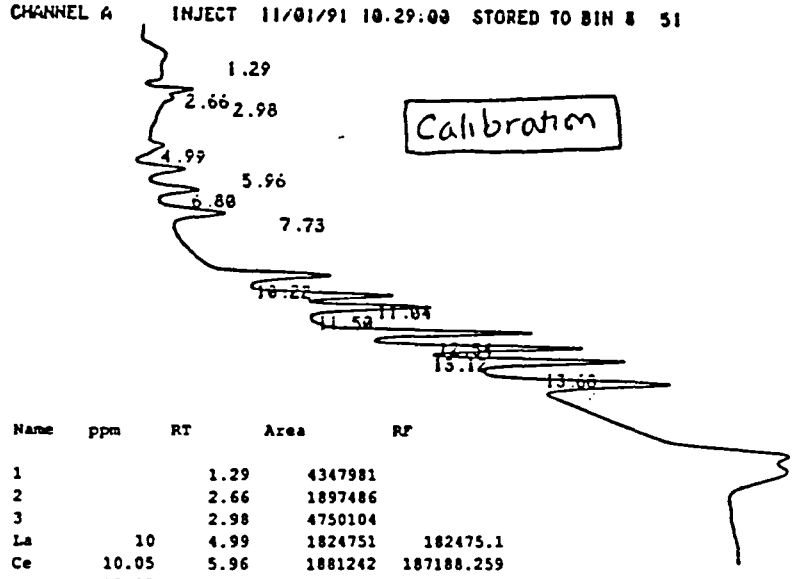

Name	ppm	RT	Area	RF
1		1.29	4347981	
2		2.66	1897486	
3		2.98	4750104	
La	10	4.99	1824751	182475.1
Ce	10.05	5.96	1881242	187188.259
Pr	10.03	6.8	2007972	200196.61
Nd	10.1	7.73	2748236	272102.574
Sm	9.95	10.22	630424	63359.196
Eu	10.15	11.04	4434829	436928.966
Gd	10.1	11.5	5535761	548095.149
Tb	10.1	12.54	5274236	522201.584
Dy	9.9	13.12	5780496	583888.485
Ho	10.05	13.68	6699779	666644.677
Er	10.05	(14.0)		
Yb	10.2	(16.7)		
Lu	10	(17.4)		

Figure 2.- A typical calibration run. The response factor (RF) is calculated by the integrator and used to calculate the concentration.

CHANNEL A INJECT 11/01/91 12:27:02 STORED TO BIN # 53

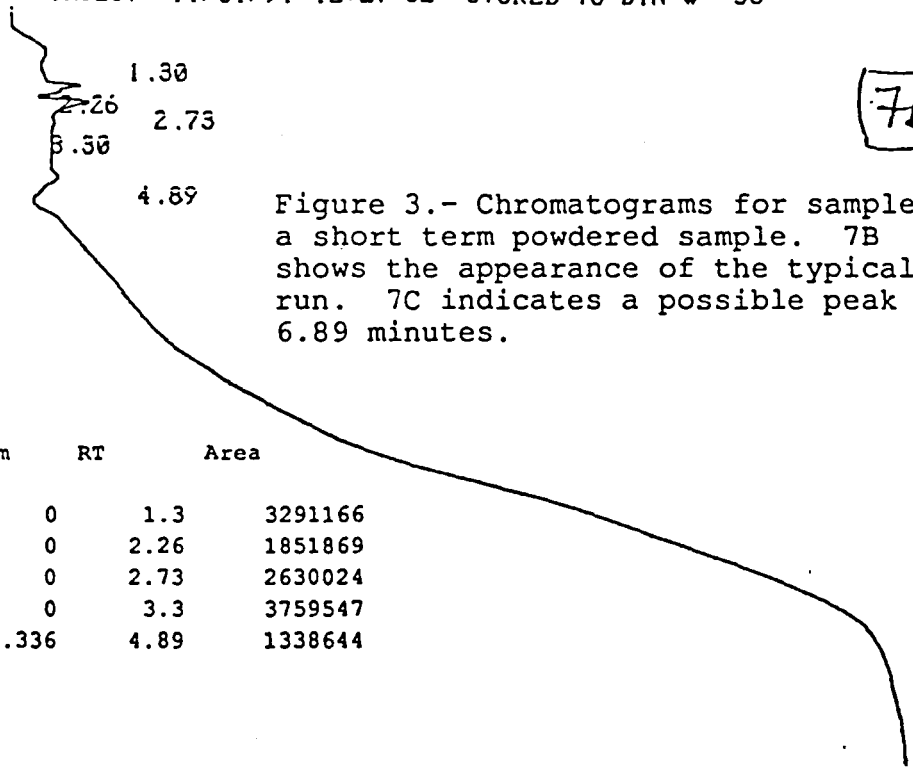

7B

Figure 3.- Chromatograms for sample 7, a short term powdered sample. 7B shows the appearance of the typical run. 7C indicates a possible peak at 6.89 minutes.

Name	ppm	RT	Area
1	0	1.3	3291166
2	0	2.26	1851869
3	0	2.73	2630024
4	0	3.3	3759547
La	7.336	4.89	1338644

CHANNEL A INJECT 11/01/91 13:21:12 STORED TO BIN # 54

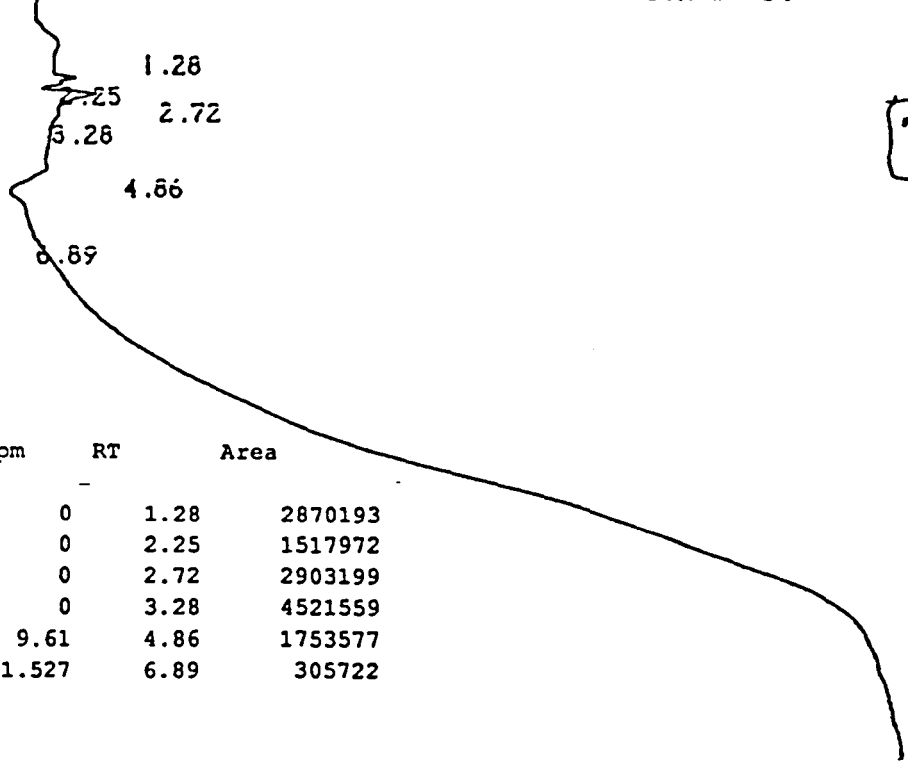

7C

Name	ppm	RT	Area
1	0	1.28	2870193
2	0	2.25	1517972
3	0	2.72	2903199
4	0	3.28	4521559
La	9.61	4.86	1753577
Pr	1.527	6.89	305722

CONCLUSION

From this study we hoped to see a movement of the REE out of the solid into the liquid. Ce and Eu should have stayed behind, as observed in the disturbed eucrites previously studied (Strait, 1991; Mittlefehldt and Lindstrom, 1991). This was not observed in the leach results or the initial the INAA analysis.

The long term sample runs are still being leached, and the runs will be concluded six to nine months from now. The long term leach may produce concentrations of REE high enough in the leach to be observable by IC, or enough depletion in REE in the solid to be observable by INAA.

This study will continue with the analysis of the samples still being leached. In the future, further work could involve changing the chemical environment of the system by varying the pH and oxidation levels of the water, the temperature of the reaction, the water to rock ratio, and the water chemistry.

Because we are working in a very liquid environment and not Gooding's "hydrocryogenic" Antarctic environment (Gooding, 1986) , what we see does not reproduce what happens in Antarctica, but this study will still give us useful new information about the movement of REE and other trace elements during the weathering process.

REFERENCES

Berkeley, J. L. and Drake, M. J.: Weathering of Mars: Antarctic Analog Studies. Icarus, vol. 45, 1981, pp. 231-249.

Boutron, C.: Respective Influence of Global Pollution and Volcanic Eruptions on the Past Variations of the Trace Metals Content of Antarctic Snows Since 1880's. J. Geophys. Res., vol. 85, 1980, pp.7426-7432.

Conca, J. and Wright, J.: The aqueous chemistry of weathering solutions in dolerite of the Allan Hills, Victoria Land, Antarctica. Antarc. J.U. S., vol. 22(5), 1987, pp. 42-44.

Duke, M.B. and Silver, L.T.: Petrology of eucrites, howardites and mesosiderites. Geochim. Cosmochim. Acta, vol. 31, 1967, pp. 1637-1665.

Gooding, J. L.: Weathering of Stony Meteorites in Antarctica. LPI Tech. Rpt. 86-01, 1986, pp. 48-54.

Gooding, J. L.: Mineralogical aspects of terrestrial weathering effects in chondrites from Allan Hills, Antarctica. Proc. Lunar Planet. Conf., vol. 12b, 1981 pp. 1105-1122.

Jovanovic, S. and Reed, G. W.: Submicroscopic Weathering of Antarctic Meteorites? Lunar Planet. Sci., vol. XVII, 1985, pp. 416-417.

Koeberl, C. and Cassidy, W. A.: Differences between Antarctic and non-Antarctic meteorites: An assessment. Geochim. Cosmochim. Acta, vol. 55, 1991, pp. 3-18.

Miklishanskiy, A. Z., Yakovlev, Yu. V., Savel'yev, B. V. and Zuyev, A. P.: Levels and compositions of the mineral components in ice cores from central Antarctica. Geochem. Int., vol. 17, 1980, pp. 152-158.

Mittlefehldt, D. W. and Lindstrom, M. M.: Generation of abnormal trace element abundances in Antarctic eucrites by weathering processes. Geochim. Cosmochim. Acta, vol. 55, 1991, pp. 77-87.

Schultz, L.: Terrestrial ages and weathering of Antarctic meteorites. LPI Tech. Rpt. 90-03, 1990, pp. 56-59.

Score, R. and Lindstrom, M. M.: Guide to the U.S. Collection of Antarctic Meteorites 1976-1988. Ant. Met. Newslet.,vol. 13, 1990.

Seyfried, W. E., Jr. and Mottl, M. J.: Hydrothermal alteration of basalt by seawater under seawater-dominated conditions. Geochim. Cosmochim. Acta, vol. 46, 1982, pp. 985-1002.

Shimizu, H., Masuda, A. and Tanaka, T.: Cerium anomaly in REE pattern of Antarctic eucrite. Mem. Natl. Inst. Polar Res. (Japan), Spec. Issue, vol. 30, 1983, pp. 341-348.

Strait, M. M.: Solutions to Problems of Weathering in Antarctic Eucrites. NASA Contractor Report, vol. 185637, 1990, pp. 24-1-15.

Strait, M. M., Mittlefehldt, D. W. and Lindstrom, M. M.: Identifying and Using Weathered Antarctic Eucrites. Lunar and Planet. Sci., vol. XXII, 1991, pp. 1347-1348.

Tatsumoto, M., Unruh, D. M. and Patchett, P. J.: U-Pb and Lu-Hf systematics of Antarctic meteorites. Proc. 6th Symp. Antarc. Met., 1981, pp. 237-249.

Velbel, M. A.: The distribution and significance of evaporitic weathering products on Antarctic meteorites. Meteoritics, vol. 23, 1988, pp. 151-159.

ACKNOWLEDGEMENT

I would like to acknowledge and thank David W. Mittlefehldt of Lockheed ESC for his help and support in this project. He provided access to his vast knowledge of the eucrites and other basaltic achondrites and was generally available as a resource and support.

NONINVASIVE pH-TELEMETRIC MEASUREMENT OF GASTROINTESTINAL FUNCTION

Final Report

NASA/ASEE Summer Faculty Fellowship Program--1991

Johnson Space Center

Prepared By:	Karen J. Tietze, Pharm.D.
Academic Rank:	Associate Professor
University & Department:	Philadelphia College of Pharmacy and Science Department of Pharmacy Practice Philadelphia, PA 19104
NASA/JSC	
Directorate:	Space and Life Sciences
Division:	Medical Sciences
Branch:	Biomedical Operations and Research
JSC Colleague:	Lakshmi Putcha, Ph.D.
Date Submitted:	August 2, 1991
Contract Number:	NGT-44-001-800

ABSTRACT

The purpose of this study was to gain experience with and validate the Heidelberg pH-telemetric methodology in order to determine if the pH-telemetric methodology would be a useful noninvasive measure of gastrointestinal transit time for future ground-based and in-flight drug evaluation studies. The Heidelberg pH metering system is a noninvasive, nonradioactive telemetric system that, following oral ingestion, continuously measures intraluminal pH of the stomach, duodenum, small bowel, ileocecal junction, and large bowel. Gastrointestinal motility profiles were obtained in normal volunteers using the lactulose breath-hydrogen and Heidelberg pH metering techniques. All profiles were obtained in the morning after an overnight fast. Heidelberg pH profiles were obtained in the fasting and fed states; lactulose breath-hydrogen profiles were obtained after a standard breakfast. Mouth-to-cecum transit time was measured as the interval from administration of lactulose (30 ml; 20 g) to a sustained increase in breath hydrogen of 10 ppm or more. Gastric emptying time was measured as the interval from the administration of the Heidelberg capsule to a sustained increase in pH of 3 units or more. Technical problems limited the number of gastric motility profiles obtained. However, mouth-to-cecum transit time, peak hydrogen, and time to peak hydrogen as measured by the lactulose breath-hydrogen test did not appear to be changed by the co-administration of the Heidelberg capsule. Food prolonged gastric emptying of the Heidelberg capsule. It appears that each method assesses a different component of the gastrointestinal system. These two methodologies test distinctly different components of gastrointestinal motility and together may provide a more complete assessment of gastrointestinal motility.

INTRODUCTION

One of NASA's scientific goals is to describe and understand human adaptation to the space environment and to use this knowledge to improve the health, safety, and performance of the astronauts (1). The absorption of orally administered drugs depends on characteristics of the drug (solubility, ionization, etc.), the nature of the formulation (solution, suspension, tablet, etc.) and the physiology of the gastrointestinal tract (pH, surface area, blood flow, etc.). Gastrointestinal hypokinesia associated with bed rest results in decreased appetite, indigestion, and constipation. Preliminary observations suggest that the microgravity also may cause gastrointestinal hypokinesia. Because gastrointestinal absorption of medications and nutrients depends on gastrointestinal pH, motility, and splanchic blood flow, it is necessary to characterize how these parameters are altered by microgravity in order to develop appropriate countermeasures. The purpose of this study was to gain experience with the Heidelberg pH-telemetric system in order to determine if the pH-telemetric methodology would be a useful noninvasive measure of gastrointestinal transit time for future ground-based and in-flight drug development and assessment studies.

BACKGROUND

Gastrointestinal Physiology

Each organ of the gastrointestinal tract (esophagus, stomach, small intestine, large intestine) is anatomically and physiologically distinct. The proximal stomach stores food; the antrum grinds and sieves food. Liquids are emptied from the stomach by a rapid first-order phase followed by a slower first-order phase. This is in contrast to gastric emptying of solids, which tends to be more sigmoid in nature. For solids, there is an initial long lag phase which is followed by a prolonged linear phase, and finally, when the stomach is nearly empty, by a very slow zero-order phase. Gastric emptying of large, indigestible particles is thought to occur during the phase III contractions of the interdigestive myoelectric motility waves ("housekeeping waves") that occur every 90-120 minutes. It is not known whether microgravity-induced changes in gastrointestinal motility affect each organ to the same extent or if different organs are affected to different degrees.

The Heidelberg pH Meter Test

The Heidelberg pH metering system is a noninvasive, nonradioactive telemetric system that, following oral ingestion, continuously measures intraluminal gastro-intestinal pH. The system consists of the pH metering

capsule, a belt antenna, a receiving console, and a heating module. The capsule is approximately the size of a No. 1 gelatin capsule (7 x 20 mm) and has a density of 1.5 g/cm3. The capsules are not sterilizable and are intended for one application.

The Heidelberg pH metering system was originally marketed as a noninvasive diagnostic tool for the evaluation of various hypo- and hypersecretory acid states and motility disorders. More recently, the Heidelberg pH metering system has been used to evaluate the effect of a variety of parameters such as food (2), gender, posture, and age on gastric residence time (3). The system has also been used to evaluate the effect of gastric residence time on the absorption of enteric-coated aspirin (4-5) and procainamide (6) as well as the effect of drugs such as ranitidine (7), omeprazole (8), loperamide, and metoclopramide (9) on various components of gastrointestinal transit time.

The Heidelberg pH-telemetric system measures the intraluminal pH of the stomach, duodenum, small bowel, ileocecal junction, and large bowel. In addition to measuring the pH of different segments of the gastro-intestinal tract, the gastric emptying time, can be determined from the characteristic pH-time profile. Gastric emptying time is the interval from the ingestion of the capsule to a sharp, sustained increase in pH of 3 units or more. The accurate measuring range is H 1.0 to 8.0 with a measuring error of +/- 0.5pH units (10).

Typical parameters for young male normal volunteers after standard feeding include a gastric residence time of 3.5 +/- 0.6 hours, duodenal pH of 5.8 +/- 0.8, small bowel transit time of 2.8 to > 5 hours, and mouth to cecum transit time within 9 hours (11). Gastric residence time appears to be reproducible (no difference between parameters when taken at one week intervals) and postural changes (supine flat on the back versus standing) do not appear to alter gastric residence time (11). However, gastric residence time is prolonged with increasing age and in females even when hormonal changes due to the menstrual cycle are normalized.

STUDY DESIGN

Gastrointestinal motility profiles were obtained in normal volunteers using the lactulose breath-hydrogen and Heidelberg pH metering techniques. All profiles were obtained in the morning after an overnight fast and/or a standard breakfast. The standard breakfast consisted of a hard boiled egg, two slices of bread/toast lightly buttered, 4 oz. orange juice, and a cup of decaffinated coffee or tea. The breakfast was consumed within a 15 minute interval; the orange juice was consumed at the end of the meal with the test material. Lactulose breath-hydrogen was measured

before and every 10 minutes for 4 hours after the lactulose was consumed. End-alveolar breath was collected and analyzed for hydrogen content. Mouth-to-cecum transit time was measured as the interval from administration of the lactulose (30 ml; 20 g) to a sustained increase in breath hydrogen of 10 ppm or more. Gastric emptying time was measured as the interval from the administration of the Heidelberg capsule to the time when there was a sustained increase in pH of 3 units or more.

RESULTS

Gastrointestinal Profiles

Technical problems limited the number of gastrointestinal motility profiles obtained. However, some trends are evident. The mouth-to-cecum transit time, peak hydrogen, and time to peak hydrogen as measured by the lactulose breath-hydrogen test did not appear to change when lactulose was administered alone or co-administered with the Heidelberg capsule (the values ranged from 60-90 min. vs. 80 min.; 40-97 ppm vs. 56 ppm; and 30-90 vs. 50 min., respectively). Food prolonged gastric emptying of the Heidelberg capsule (320 min. fed vs. 30-38 min. fasting).

Procedures

Appropriate functioning of the Heidelberg pH-telemetric system depends on close attention to operational details. The following additions to the procedures supplied in the manual are recommended:

1. Turn the heating module on at least one hour prior to administration of the capsule. Set the left hand knob to 3.5. The module is very slow to reach equilibrium and very sensitive to the setting. Do not try to rush the warm-up period by setting the knob higher than 3.5.

2. Fill the stainless steel rinse dish to within one-half inch of the rim with deionized water. Do not use tap water. Replace the rinse water if more than two or three calibration checks are necessary.

3. Fill a 16 x 100 mm disposable glass culture tube one-half full with 0.9% sodium chloride. It is absolutely necessary to have in-date and accurately prepared 0.9% sodium chloride solutions. Do not try to make the 0.9% sodium chloride from laboratory or table sodium chloride. Non-preserved, single use injectable 0.9% sodium chloride solutions work well with the system, but do not save the bottle or bag for another test.

4. Using long-nose forceps, gently place the capsule, white end up, into the tube with the 0.9% sodium chloride. Observe two or three bubbles leave the capsule and then gently scrape the white mesh of the capsule with a fingernail to break the surface tension. It is absolutely essential that the white mesh is saturated with solution and not covered with air. Leave the capsule undisturbed for at least 15-20 minutes. (Disregard the company's recommendation of a 2 minute soaking interval).

Problem Shooting. All capsules can be calibrated. If the capsule calibrates to pH 1 initially, but will not calibrate to pH 7, the 0.9% sodium chloride is at fault. Change to a different lot or brand of 0.9% sodium chloride and start over with another capsule. Soak the the original capsule in deionized water for 20-30 minutes and dry at room temperature for at least 48 hours before attempting to recalibrate with new 0.9% sodium chloride. If the capsule will not calibrate to pH 1, there is something wrong with the system. The problem may be with the calibration antenna, which is the most sensitive component of the system. Unplug the calibration antenna from the console and take the acrylic block out of the heater module and place it on the center of the antenna belt. This allows the capsule to be calibrated with the antenna belt directly and bypasses the calibration antenna. Calibrate the capsule as above. If this fails, contact the company for further advice.

RECOMMENDATIONS

The Heidelberg pH-telemetric system is a relatively simple, noninvasive method for the assessment of the gastric emptying rate. Although the calibration of the system is a little tricky and very dependent on the accuracy of the 0.9% sodium chloride, the noninvasiveness of the test and the lack of dependency on the degree of subject cooperation make it a good evaluation method for in-flight testing. It is not clear whether the gastric emptying rate of the large indigestible capsule reflects true gastric emptying of food particles or just the final housekeeping phase of gastric emptying.

The exact relationship between changes in gastrointestinal motility as measured by the lactulose breath-hydrogen method and the Heidelberg pH-telemetric method remains to be determined. From the limited data obtained in this study, it appears that each method assesses a different component of the gastrointestinal system. Measurement of gastrointestinal function with both of these methodologies may provide a more complete view of gastrointestinal function. The influence of one test material on the other has yet to be determined, but it appears that each test functions independently of the other.

Several equipment changes are recommended before the system is considered for in-flight studies. A small, hand-sized console unit should be developed that could be clipped to a belt. This would allow the astronaut to be completely mobile throughout the testing period. Another alternative would be to develop a hand-sized recorder that would receive and record the battery signals. A final concern is with the size of the calibration capsule. Emptying of a smaller sized capsule may be a more accurate measure of gastric emptying of food particles and a more realistic evaluation of gastric function.

References.

1. Committee on Space Science and Medicine. A Strategy for Space Biology and Medical Sciences. National Academy Press, Washington, D.C. 1987.

2. Mojaverian P, Ferguson RK, Vlasses PH et al. Estimation of gastric residence time on the Heidelberg capsule in humans: Effect of varying food composition. Gastroenterolgy 1985; 89:392-7.

3. Mojaverian P, Vlasses PH, Kellner P et al. Effects of gender, posture, and age on gastric residence time of an indigestible solid: pharmaceutical considerations. Pharmaceutical Res 1988; 5:639-44.

4. Mojaverian P, Rocci ML, Conner DP et al. Effect of food on the absorption of enteric-coated aspirin: Correlation with gastric residence time. Clin Pharmacol Ther 1987; 41:11-17.

5. Lui CY, Oberle R, Fleisher D et al. Application of a radiotelemetric system to evaluate the performance of enteric coated and plain aspirin tablets. J Pharm Sci 1986; 75:469-74.

6. Rocci ML Jr, Mojaverian P, Davis RJ et al. Food-induced gastric retention and absorption of sustained-release procainamide. Clin Pharmacol Ther 1987; 42:45-9.

7. Mojaverian P, Parker S, Warner C et al. Single and multiple oral doses of ranitidine accelerate the gastric transit of an indigestible capsule in man. Clin Pharmacol Ther 1989; 45:183. Abstract

8. Vlasses PH, Rocci MJ Jr, Distlerath LM et al. Pharmacokinetics and pharmacodynamics of intravenous omeprazole, a selective gastric H+/K+ ATPase inhibitor in healthy men. Clin Pharmacol Ther 1989; 45:183.

9. Kirby MG, Kutes GE, Powell JR et al. The dose-effect of loperamide and metoclopramide on various components of gastrointestinal transit time. Clin Pharmacol Ther 1987; 41:168. Abstract

10. Youngberg CA, Wlodyga J, Schmaltz S et al. Radiotelemetric determination of gastrointestinal pH in four healthy beagles. Am J Vet Res 1985; 46:1516-21.

11. Mojaverian P, Chan K, Desai A et al. Gastrointestinal transit of a solid indigestible capsule as measured by radiotelemetry and dual gamma scintigraphy. Pharmaceutical Res 1989; 6:719-24.

AN INTELLIGENT COMPUTER-AIDED TRAINING SYSTEM (ICAT) FOR DIAGNOSING ADULT ILLITERATES: INTEGRATING NASA TECHNOLOGY INTO WORKPLACE LITERACY

Final Report

NASA/JSC Summer Faculty Fellowship Program--1991

Johnson Space Center

Prepared by:	David B. Yaden, Jr., Ph.D.
Academic Rank:	Associate Professor
University & Department:	University of Houston - University Park Department of Curriculum and Instruction Houston, Texas 77204-5872
NASA/JSC	
Directorate:	Information Systems
Division:	Information Technology
Branch:	Software Technology
JSC Colleague:	James A. Villarreal
Date Submitted:	August 14, 1991
Contract Number:	NGT 44-001-800

ABSTRACT

An important part of NASA's mission involves the secondary application of its technologies in the public and private sectors. One current application being developed is the The Adult Literacy Evaluator, a simulation-based diagnostic tool designed to assess the operant literacy abilities of adults having difficulties in learning to read and write. Using ICAT system technology in addition to speech recognition, closed-captioned television (CCTV), live video and other state-of-the art graphics and storage capabilities, this project attempts to overcome the negative effects of adult literacy assessment by allowing the client to interact with a intelligent computer system which simulates real-life literacy activities and materials and which measures literacy performance in the actual context of its use. The specific objectives of the project are as follows: (a) To develop a simulation-based diagnostic tool to assess adults' prior knowledge about reading and writing processes in actual contexts of application, (b) to provide a profile of readers' strengths and weaknesses, and (c) to suggest instructional strategies and materials which can be used as a beginning point for remediation. In the first and development phase of the project, descriptions of literacy events and environments are being written and functional literacy documents analyzed for their components. Examples of literacy events and situations being considered included interactions with environmental print (e.g., billboards, street signs, commercial marquees, storefront logos, etc.), functional literacy materials (e.g., newspapers, magazines, telephone books, bills, receipts, etc.) and employment-related communication (i.e., job descriptions, application forms, technical manuals, memorandums, newsletters, etc.). Each of these situations and materials are being analyzed for its literacy requirements in terms of written display (i.e., knowledge of printed forms and conventions), meaning demands (i.e., comprehension and word knowledge) and social situation. From these descriptions, scripts are being generated which define the interaction between the student, an on-screen guide and the simulated literacy environment. The proposed outcome of the Evaluator is a diagnostic profile which will present broad classifications of literacy behaviors across the major areas of metacognitive abilities, word recognition, vocabulary knowledge, comprehension and writing. From these classifications, suggestions for materials and strategies for instruction with which to begin corrective action will be made. The focus of the Literacy Evaluator will be essentially to provide an expert diagnosis, and an interpretation of that assessment which then can be used by a human tutor to further design and individualize a remedial program as needed through the use of an authoring system.

INTRODUCTION

Secondary Applications of NASA Technology

As mandated by Congress, one of NASA's principal charters is to facilitate the transfer of its vast technological knowledge into the public and private sectors for the general benefit of the American populace. Further, NASA has taken a particular interest and lead in promoting educational programs and innovations which not only enrich American life, but also serve to maintain and sharpen this country's scientific and technological edge (Haggarty, 1990, Technology Utilization Office, 1991). The Adult Literacy Evaluator represents an important spinoff project which will bring to bear NASA's considerable expertise in artificial intelligence (AI) and intelligent computer-aided training (ICAT) upon the growing problem of adult illiteracy and diminishing workplace literacy skills. This project with its application of expert system technology to the diagnosis and evaluation of reading problems represents a significant advance over current computer-assisted instruction (CAI) in literacy which provides no intelligent feedback to either student or tutor. After a brief overview of some of the issues in adult literacy instruction, the following report will describe the current status of the project and its proposed development schedule.

Adult Literacy: A National Issue

While experts disagree on the exact magnitude of the problem of adult illiteracy both in the U.S. and elsewhere, there is no doubt that educators, industry executives and government officials are concerned about what seems to be a rising tide of workers who are ill-equipped to meet the requirements of an increasingly technological and information-based society. Not only does illiteracy impact a person's ability to participate fully in a democratic society, the cost of remedial education to U.S. corporations each year reaches into the billions of dollars annually (Barlow, 1991; Jennings, 1988). This expense coupled with the fact that the nation now spends more federal monies on education than on defense (U.S. Department of Education, 1991) presents an alarming picture which suggests that our current system of public elementary and secondary schooling may have reached a point of "diminishing returns" in preparing workers for jobs in an age where information is a primary commodity and its rapid and efficient management is of paramount importance.

In order to improve the quality of education and to ensure that America has a competent workforce in the 21st century, the President and the nation's governors identified in 1989 six national goals to be accomplished by the year 2000. In essence, these goals call for the participation of business and industry in education, the setting of national standards of achievement, and the elimination of illiteracy in the adult population. While the feasibility of this latter goal has been questioned (Mikulecky & Drew, 1991), the federal government's efforts to study adult learning and workplace literacy have intensified over the last few years with the establishment of the National Center on Adult Literacy at the University of Pennsylvania in October 1990 and by the recent passing of the National Literacy Act in July 1991 which will provide federal funds for the establishment of state literacy resource centers. Further, a new agency, the National Institute for Literacy, is in the development stage and will provide additional resources for research and evaluation of adult literacy programs (Lovell, 1991).

Workplace Literacy Assessment

Despite these widespread efforts to combat adult illiteracy and increase the quality of performance in the workplace, several problems present themselves to researchers and practitioners in this field. The first of these concerns the disparity between skills learned in school and those actually required on the job. Research has found that job site literacy materials not only are of a greater variety than those found in school, but are often more difficult. In addition, Mikulecky (1982) has found that in comparison to high school students workers actually spend more time reading on the job and perform higher level reading tasks such as self-questioning, summarizing or monitoring. Thus, one of the serious hindrances to an increased supply of competent workers is that traditional literacy instruction in school is very narrow and there is little guarantee that even the skills that are learned transfer easily to real-life reading and writing tasks.

Another area of concern is the lack of assessment instruments which adequately measure literacy ability as it manifests itself in real-world reading tasks. Although standardized tests exist which are commonly used in evaluating the progress of adult education programs, there is widespread consensus (cf. Askov, 1991) that these traditional pencil and paper tests lack content validity for indexing job site literacy skills and cannot reliably predict a person's actual reading and writing performance in the workplace. In an attempt to remedy this situation, the Department of Labor commissioned the development of the *Applied Tests of Literacy Skills* based upon the 1986 National Assessment of Educational Progress survey of young adults, ages 21-25. These tests use facsimile productions of newspaper articles, office memorandums job applications, tables, charts, etc. to simulate actual workplace materials and tasks. However, it remains to be seen if this non-situated, pencil and paper test can overcome the limitations of most psychometric measures of its type.

PROJECT DESCRIPTION AND STATUS

Project Overview and Objectives

The scope of the NASA Adult Literacy Evaluator aims at both incorporating real-life reading and writing tasks as well as providing through computer simulation actual situations encountered in the environment and workplace. The specific objectives of the project are to (a) develop a simulation-based, expert system diagnostic tool to assess adults' prior knowledge about literacy processes and materials in the context of their use, (b) to provide a profile of readers' strengths and weaknesses, and (c) to suggest instructional strategies and materials which can be used as a beginning point for remediation. The initial target population whom the project intends to serve is the two to six percent of the adult population whose facility with written language is extremely limited (Elkind, 1990). However, one assumption underlying the program is that even adults who've failed in school or on traditional pencil and paper tests of literacy skills still have considerable knowledge about written displays in the environment which are not tapped by present methods of testing. A fundamental premise of the project is that unless this prior knowledge about print in the environment is known, then corrective instruction will inevitably either over-or underestimate the adult's actual level of ability. In order to create these simulated literacy events, the project is in the process of experimenting with the following technologies: Closed-captioned television (CCTV), computerized speech recognition and production, live video, virtual reality and laser disk storage of video images. At present, all of the foregoing are being designed to run on a Macintosh IIci or better with touch screen and voice regulated response to be integrated as is possible.

Literacy Knowledge Base

Range of components. The first step in developing the Adult Literacy Evaluator has been to identify the actual components of literacy that will be simulated and assessed. Drawing from the experience of literacy experts, reference materials and the professional literature in reading education, over 300 areas of literacy behavior have been categorized under six broad rubrics: (a) Aspects of metacognition, (b) word recognition, (c) vocabulary, (d) comprehension, (d) fluency, (e) writing, and (f) studying. Under each one of these major literacy topics, further subcategorizations have been developed in a logical hierarchy, subject to verification as the development process continues. Given the space limitations of this paper, it is not possible to display all of the 300 categories and their respective definitions. However, represented in Figure 1 below is a subset of components arranged under the topic of Written Language Awareness, one of the four subheadings under Metalinguistic Awareness which in turn is one of four topics under Aspects of Metacognition. Written language awareness is further subdivided into knowledge about written conventions, written symbols (graphemes), word boundaries, print orientation and direction, sentence boundaries and the relationship between different kinds of pictorial displays and the text in which they are embedded. Each of these topics in turn have further breakdowns into the specific graphic symbols which appear in written materials and the conventional processes or page formats which are used to render these written features into the intended meaning of the respective document.

Concepts assessed. Coupled with each component displayed in the tree diagram and representing the knowledge base of the system are definitions which outline the parameters of what each node means in terms of specific assessment. These definitions form the basis of the expert system diagnosis and interpretation which will be relevant as the subject proceeds through the simulated settings and literacy events as constructed by the program. An example of definitions is displayed in Table 1 for the major topic of Metacognition, the subheading Metalinguistic Awareness and for some of the components under Conventions previously represented (see Fig. 1). Presently, initial definitions for over 100 areas under Metacognition have been written and are currently undergoing revision and refinement. Additional descriptions of the knowledge base for the other six major literacy areas are yet to be completed.

Literacy Environments

Graphic displays. Although most of the estimated 30-60 million adults reading below the eighth grade level in this country consistently fail on school-based tests of reading and writing, they do not lack knowledge about the written environment and oftentimes manage adeptly to either cope with the level of knowledge that they have or to learn how to use others' knowledge for their benefit. The intent of the Adult Literacy Evaluator is to produce computer-based simulations of everyday and workplace literacy situations where print has a ubiquitous presence and give these adults an opportunity to display the knowledge that they have in the context in which they apply it. Some of the literacy documents intended for use include, but are not limited to, interactions with environmental print (e.g., billboards, street signs, commercial marquees, storefront logos), functional literacy materials (e.g., newspapers, magazines, telephone books, TV Guide, bills receipts, etc.) and employment-related communication (for instance, job descriptions, application forms, technical manuals, flyers, newsletters, memorandums, etc.). The range of the print in these environments will vary from simple one or two word signs to paragraphs. Examples of text to be used in the simulations are depicted in Figure 2.

Literacy scenarios. Unlike most testing situations where the knowledge assessed is completely out of context, the Literacy Evaluator will take subjects through a series of natural literacy activities encountered on common excursions in the environment. This type of assessment of environmental print knowledge and coping skills is not unlike a case study approach to remediation and diagnosis where the clinician or tutor accompanies an illiterate adult in a variety of situations and observes how the person negotiates encounters with others where written language is normally involved. Three "vignettes" currently being developed are a walk through a mall , a grocery store and a tour of NASA itself is being considered. Other actual job site situations are planned as well. In each one of these scenarios, several types of encounters with print are possible. At each one of these encounters, a "script" is being written in which the subject in some instances will converse with an on-screen guide who may, as a clinician would, ask a series of questions such as "What does this sign tell us?" "What symbols do you recognize?" "Where do you think it says, 'No Parking?'" In another type of encounter, such as with an ATM machine, the person will need to respond to the written screen prompts either by reading them aloud or simply pressing the right button in order to complete the task of getting money for some further encounter. Finally, in some instances, the subject may be directed to respond by using an electronic stylus to fill out an application form, write a check or complete an order form for a purchase. The goal of the scenarios developed is to simulate as many situations as possible where written language plays an integral role such that an accurate, in- context assessment might be made of the adult's full range of knowledge about and functioning with printed forms.

Graphical user interface and assessment. In order to have the widest possible range of response capabilities, the project is intending to incorporate along with the standard Macintosh interface, speech and handwriting recognition, touch-screen capabilities and voice recording. Each response of the adult will be classified, counted or evaluated by the appropriate assessment algorithm or AI program software. For instance, all of the print used in the scenarios will be classified as to its appearance on lists of basic words and the adult's response to each of these words will be monitored. Additionally, the use of neural networks may be used in the speech and handwriting recognition and fuzzy logic programming might be appropriate for determining whether a series of behaviors constitutes knowledge of a certain literacy domain. The eventual program output to a human tutor will involve not only the normal assessment areas such as would be gained by the administration of a diagnostic reading test, but also an interpretation of the person's knowledge of and concepts about written language displays as well as their behavior with specific print forms.

It is this latter knowledge, in particular, that is absent from traditional assessments. Tests routinely report results in the form of standard scores, grade or age levels or descriptive frequencies of words, letters, sentences, etc. that are right or wrong. What test results cannot provide is an interpretation of the relationship between scores or the reasons why a person responded this way or that. Thus, tutors working with adults with reading problems usually operate only on negative information, that is, what they don't know as revealed on non-situated, paper and pencil tests. Therefore, the purpose of the present project is to provide both *situated information* about a person's reading ability as well as *interpretations* regarding the person's performance and what concepts about written language would cause the person to respond in such a way.

Computing Platform

The research and development platform of the project is illustrated in Figure 3. While an early demonstration of the program made use of the VCR to incorporate live video, use of a digital video interface (DVI) board for use with a CD - ROM is faster for manipulating video. This technology in turn may give way to a new Apple System product call QuickTime, a software extension which would eliminate the need for extra hardware to compress video images. In addition, the current speech recognition system needs considerable processing power in the form of a workstation, something that would be too impractical and expensive in a commercial application. While the Macintosh can use a software system with an add-in board called Voice Navigator which allows the user to access menu items with voice commands, the system at present must be customized for every speaker. Further, the present technology of speech recognition computing systems is still at a relatively rudimentary stage, with no system being able to converse easily as would a human interlocutor (Smith, 1990). The project plan, therefore, is to incorporate the speech recognition component at the level of technology available and use it within whatever constraints are necessary. Finally, the intended delivery platform would consist of a Macintosh IIci or better with keyboard and mouse, a headphone and microphone setup, a large hard disk or writable CD - ROM and a software system which would handle the video features and speech recognition for multiple speakers. During the development phase, all of the above technologies are being evaluated for their utility in enhancing the demonstration of literacy concepts as well for their current stage of development and anticipated cost.

Development Schedule

The overall research plan and schedule specifies three phases for project completion given adequate funding: (a) Phase I - Development should be completed by Spring 1992, (b) Phase II - Field Test and Refinement would extend through the remainder of the year, and (c) Phase III - Commercialization would begin after January 1993. Currently, detailed planning with the development phase calls for a complete functional requirements document specifying the literacy concepts to be evaluated and the graphical user interface to be completed by early Fall of 1991. Following this, a detailed design document implementing the functional requirements is to be finished before the end of the 1991. Actual programming should then begin during the early months of 1992. Adherence to this schedule as mentioned is greatly dependent upon receiving the funding necessary to support the additional programmers and media specialists needed as well as to purchase equipment and software for development.

SUMMARY

The design of this project attempts to minimize the negative effects of past failures in school by allowing adults to interact with a sophisticated ICAT system, thus giving students some "psychological" distance between themselves and a human evaluator as well as providing an opportunity to demonstrate what literacy knowledge they possess in the actual context of its use. Further, the use of simulated environmental and workplace literacy settings also gives the Literacy Evaluator greater ecological validity than paper and pencil tests which measure literacy skills in isolation only. Finally, the true use of AI technology constitutes an advance over current computer-assisted instruction which is reduced to only the cataloging of information and which has no knowledge base from which to interpret learner characteristics.

REFERENCES

Askov, E.: Workplace Literacy and Technology. Paper presented at the Adult Literacy and Technology Conference (Costa Mesa, CA), July 1991.

Barlow, J.: Dumbing Down Jobs is Dumb. *Houston Chronicle*, Section C, Aug. 19, 1991.

Barton, P. E.; and Kirsch, I. S. : Workplace Competencies: The Need to Improve Literacy and Employment Readiness. Information Services, Office of Educational Research and Improvement, U. S. Department of Education, 1991.

Elkind, J.: The Incidence of Disabilities in the United States. *Human Factors*, Vol. 34, no. 4, August 1990, pp. 397-405.

Haggerty, J. J.: NASA Spinoff 1990. NASA NP 138, 1990.

Jennings, W.: A Comprehensive Five Year Plan for Adult LIteracy in St. Paul, Minnesota. The St. Paul Foundation and The F. R. Bigelow Foundation, August 1988.

Lovell, M.: Using of Technology and Adult Basic Education and Literacy Programs. Paper presented at the Adult Liteacy and Technology Conference (Costa Mesa, CA), July 1991.

Mikulecky, L.: Job Literacy: The Relationship Betweeen School Preparation and Workplace Actuality. *Reading Research Quarterly*, vol. 17, 1982, pp. 400-419.

Mikulecky, L.; and Drew, R.: Basic Literacy Skills in the Workplace. Handbook of Reading Research, Vol. II., R. Barr, M. L. Kamil, P. Mosenthal, and P. David Pearson, eds., Longman Publishing Group, 1991, pp. 669-689.

Newman, A. P.; and Beverstock, C.: Adult Literacy: Contexts and Challenges. International Reading Association, 1991.

Smith, B. E.: Speech! Speech! The Really Important Multimedia Technology is Getting Little Attention From the Hypemeisters. *Personal Workstation*, September 1990, pp. 30-32.

Technology Utilization Office, Johnson Space Center, 1990 Activities. Annual Report, February 1991.

U. S. Department of Education: AMERICA 2000: An Education Strategy. (Washington, D. C.), 1991.

TABLE 1: DEFINITIONS OF LITERACY COMPONENTS

Literacy Topics

- Aspects of Metacognition

  Knowledge of one's own mental processes for acquiring, manipulating, and applying information derived from written sources. The ability to reflect upon and monitor one's own contents of "mind."

  - Metalinguistic Awareness

    The ability to treat either oral or written language as an "object of thought," understanding that each language system is comprised of smaller units which have logical relationships among themselves as well as reference to objects both psychological and physical in the real world.

    - Written-Language Awareness

      The ability to treat written language as an object of thought, recognizing that this system represents both oral language and meaning at the same time. Knowledge that written language is comprised of many smaller units each of which has a variety of invariant as well as relative features.

      - Conventions

        Knowledge that the display of written language for the purpose of communication follows certain arbitrary rules which vary from language to language. These rules relate to all levels of the subunits of printed form.

        - Capital

          Knowledge of the various functions of upper case letters such as
          (a) signalling the beginning of sentences,
          (b) designating proper names and adjectives,
          (c) indicating titles or specialized names,
          (d) referring to the Deity, and
          (e) using the pronoun I.

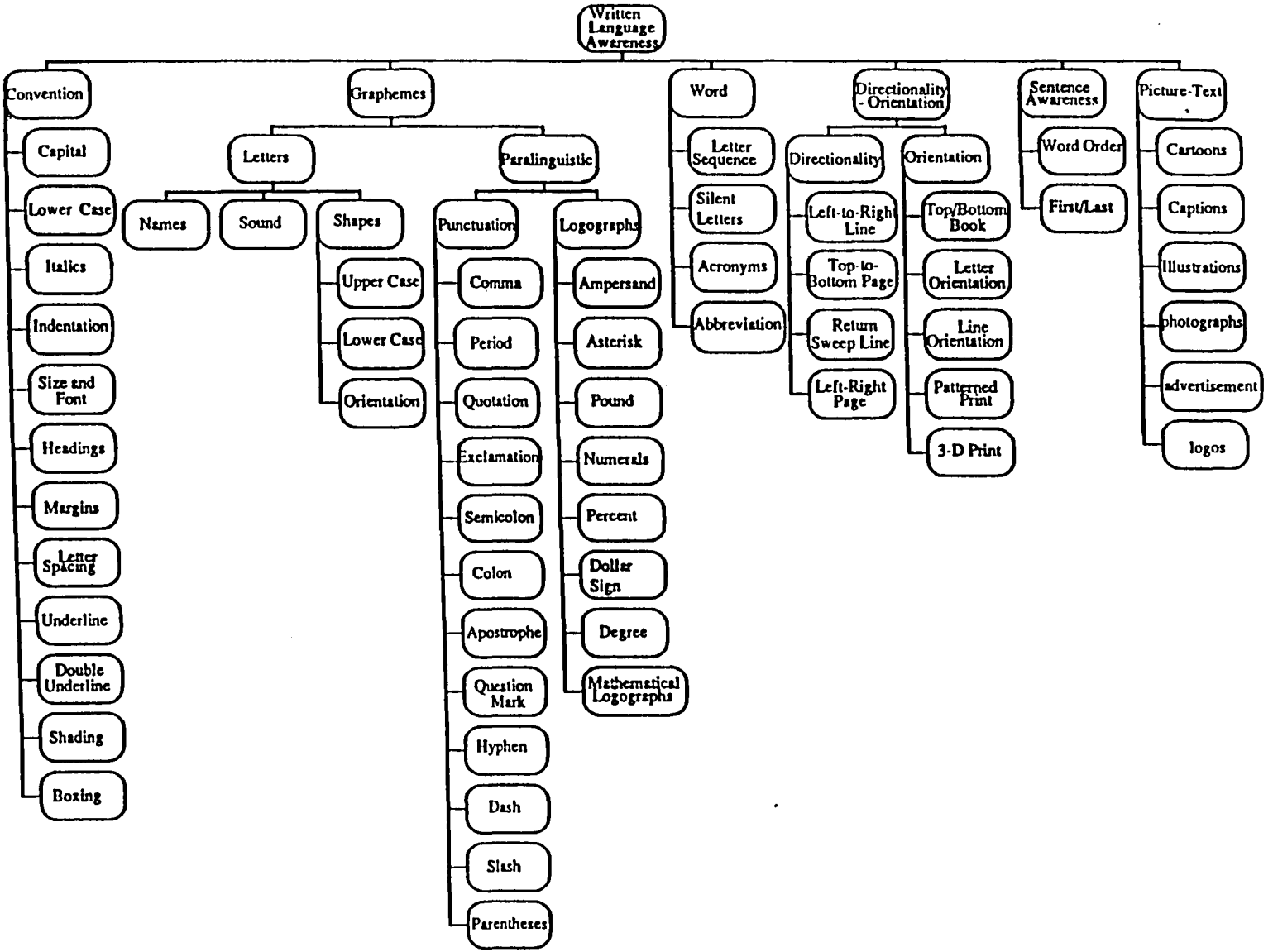

Figure 1: Components of Written Language Awareness

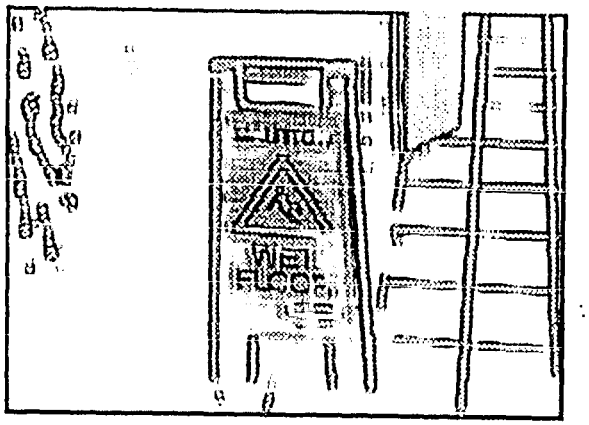

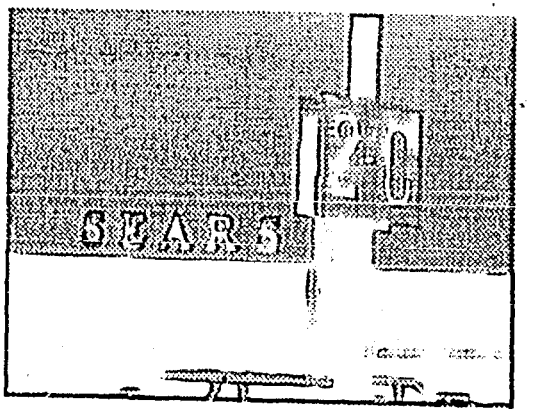

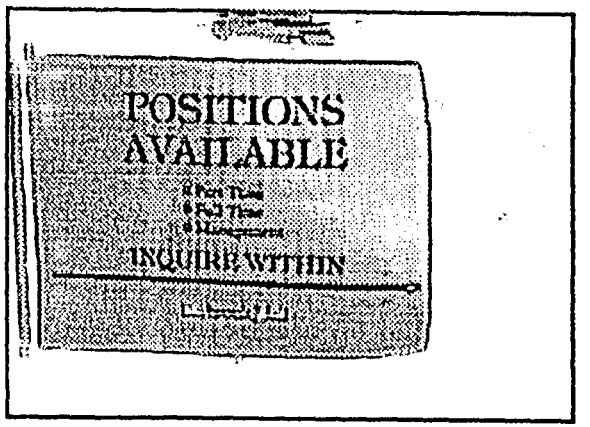

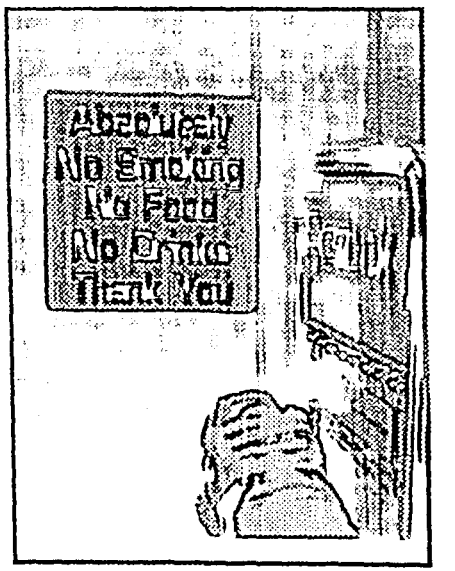

Figure 2. Examples of Environmental Print

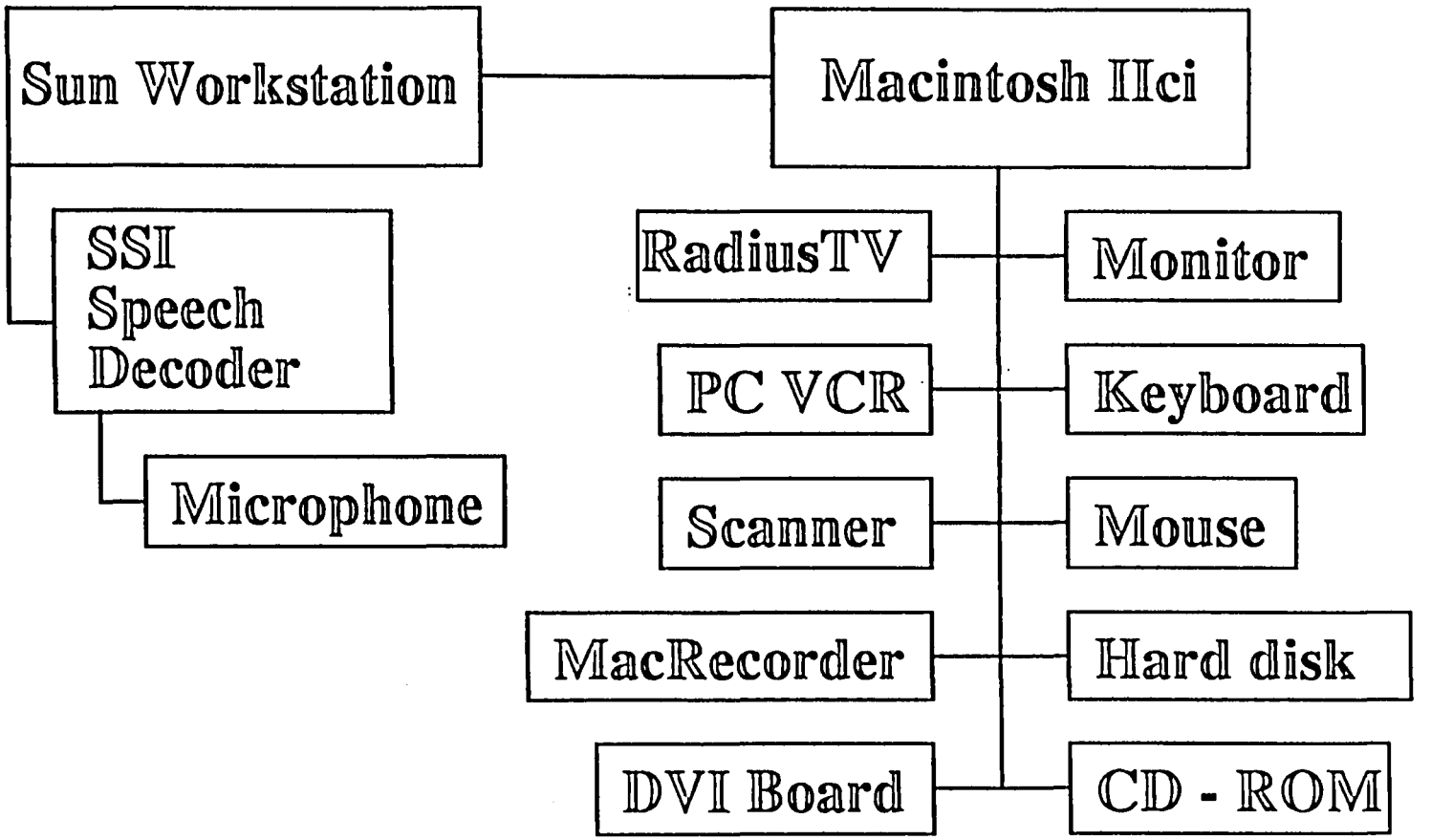

Figure 3. Research and Development Platform

REPORT DOCUMENTATION PAGE

Form Approved
OMB No. 0704-0188

1. AGENCY USE ONLY *(Leave blank)*	2. REPORT DATE	3. REPORT TYPE AND DATES COVERED
	December 1991	Contractor Report

4. TITLE AND SUBTITLE
National Aeronautics and Space Administration (NASA)/American Society for Engineering Education (ASEE) Summer Faculty Fellowship Program - 1991 Volume 2

5. FUNDING NUMBERS
NGT 44-001-800

6. AUTHOR(S)
William A. Hyman and Stanley H. Goldstein, Editors

7. PERFORMING ORGANIZATION NAME(S) AND ADDRESS(ES)
Texas A&M University
College Station, Texas

8. PERFORMING ORGANIZATION REPORT NUMBER

9. SPONSORING / MONITORING AGENCY NAME(S) AND ADDRESS(ES)
University Programs Office
Lyndon B. Johnson Space Center
Houston, Texas

10. SPONSORING / MONITORING AGENCY REPORT NUMBER
NASA CR 185670

11. SUPPLEMENTARY NOTES

12a. DISTRIBUTION / AVAILABILITY STATEMENT
Unclassified/Unlimited

Star Category 99

12b. DISTRIBUTION CODE

13. ABSTRACT *(Maximum 200 words)*

The 1991 Johnson Space Center (JSC) National Aeronautics and Space Administration (NASA)/American Society for Engineering Education (ASEE) Summer Faculty Fellowship Program was conducted by Texas A&M University and JSC. The program at JSC, as well as the programs at other NASA Centers, was funded by the Office of University Affairs, NASA Headquarters Washington, D.C. The objectives of the program, which began nationally in 1964 and at JSC in 1965, are (1) to further the professional knowledge of qualified engineering and science faculty members; (2) to stimulate an exchange of ideas between participants and NASA; (3) to enrich and refresh the research and teaching activities of participants' institutions; and (4) to contribute to the research objective of the NASA Centers.

Each faculty fellow spent at least 10 weeks at JSC engaged in a research project in collaboration with a NASA JSC colleague. This document is a compilation of the final reports on the research projects performed by the faculty fellows during the summmer of 1991. Volume 1 contains reports 1 through 14, and Volume 2 contains reports 15 through 27.

14. SUBJECT TERMS	15. NUMBER OF PAGES
	16. PRICE CODE

17. SECURITY CLASSIFICATION OF REPORT	18. SECURITY CLASSIFICATION OF THIS PAGE	19. SECURITY CLASSIFICATION OF ABSTRACT	20. LIMITATION OF ABSTRACT
Unclassified	Unclassified	Unclassified	Unlimited

End of Document